
A stabilized mixed discontinuous Galerkin formulation for double porosity/permeability model

AN E-PRINT OF THE PAPER IS AVAILABLE ON ARXIV: 1805.01389.

AUTHORED BY

M. S. JOSHAGHANI

Graduate Student, University of Houston

S. H. S. JOODAT

Graduate Student, University of Houston

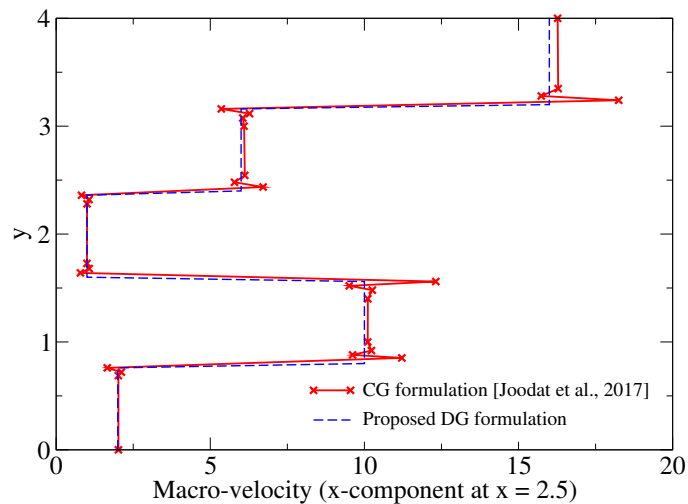
K. B. NAKSHATRALA

Department of Civil & Environmental Engineering

University of Houston, Houston, Texas 77204-4003

phone: +1-713-743-4418, **e-mail:** knakshatrala@uh.edu

website: <http://www.cive.uh.edu/faculty/nakshatrala>



Comparison of the profiles of the macro-velocity under the stabilized mixed continuous Galerkin (CG) formulation and the proposed stabilized mixed discontinuous Galerkin (DG) formulation. Under the CG formulation, overshoots and undershoots are observed at the interfaces of the layers. On the other hand, the proposed DG formulation is able to capture the physical jumps across the interfaces.

A stabilized mixed discontinuous Galerkin formulation for double porosity/permeability model

M. S. Joshaghani, S. H. S. Joodat and K. B. Nakshatrala

Department of Civil and Environmental Engineering, University of Houston.

Correspondence to: knakshatrala@uh.edu

ABSTRACT. Modeling flow through porous media with multiple pore-networks has now become an active area of research due to recent technological endeavors like geological carbon sequestration and recovery of hydrocarbons from tight rock formations. Herein, we consider the double porosity/permeability (DPP) model, which describes the flow of a single-phase incompressible fluid through a porous medium exhibiting two dominant pore-networks with a possibility of mass transfer across them. We present a stable mixed discontinuous Galerkin (DG) formulation for the DPP model. The formulation enjoys several attractive features. These include: (i) Equal-order interpolation for all the field variables (which is computationally the most convenient) is stable under the proposed formulation. (ii) The stabilization terms are residual-based, and the stabilization parameters do not contain any mesh-dependent parameters. (iii) The formulation is theoretically shown to be consistent, stable, and hence convergent. (iv) The formulation supports non-conforming discretization and distorted meshes. (v) The DG formulation has improved element-wise (local) mass balance compared to the corresponding continuous formulation. (vi) The proposed formulation can capture physical instabilities in coupled flow and transport problems under the DPP model.

A list of abbreviations and symbols

<i>Abbreviations</i>	
CG	Continuous Galerkin
DG	Discontinuous Galerkin
DPP	Double porosity/permeability
<i>Symbols in the DPP model, §2</i>	
$\Omega, \bar{\Omega}, \partial\Omega$	Computational porous domain, its set closure, and its boundary
$\mathbf{u}_1, \mathbf{u}_2, p_1, p_2$	Velocity and pressure solution fields in the two pore-networks
k_1, k_2	Permeabilities in the two pore-networks
γ, μ	True density and coefficient of viscosity of the fluid
$\mathbf{b}_1, \mathbf{b}_2$	Specific body forces in the pore-networks
$\hat{\mathbf{n}}(\mathbf{x})$	Unit outward normal vector at $\mathbf{x} \in \partial\Omega$
$u_{n1}, u_{n2}, p_{01}, p_{02}$	Prescribed velocities and pressures, Eqs. (2.1f)–(2.1i)
$\Gamma_1^u, \Gamma_2^u, \Gamma_1^p, \Gamma_2^p$	Velocity and pressure boundaries, Eq. (2.2)
χ	Mass exchange across the pore-networks, Eq. (2.1e)
β	Parameter in the inter-pore mass transfer, Eq. (2.1e)

Key words and phrases. discontinuous Galerkin methods; mixed methods; stabilized formulations; error analysis; double porosity/permeability model; flow through porous media.

η	Flow characterization parameter in the DPP model, Eq. (5.5)
<i>Mesh-related quantities, §2</i>	
$Nele$	Number of subdomains (elements)
$\omega^i, \partial\omega^i$	The i -th subdomain and its boundary ($i = 1, \dots, Nele$)
$\tilde{\Omega}$	Union of all open subdomains, Eq. (2.6)
$\mathcal{E}, \mathcal{E}^{\text{int}}$	Sets of all and interior edges, respectively
Υ	A typical edge (i.e., $\Upsilon \in \mathcal{E}$ or $\Upsilon \in \mathcal{E}^{\text{int}}$)
Γ^{int}	Union of internal boundaries
h	Mesh-size, Eq. (2.15)
h_ω	Element diameter of ω , §2.4 & Fig. 2
h_ω^{inc}	Diameter of the inscribed circle in ω , §2.4 & Fig. 2
h_Υ	Characteristic length of an edge, Eq. (2.16)
$\mathcal{T}, \mathcal{T}_h$	A mesh, and a mesh with mesh-size h
<i>Symbols in the proposed DG formulation, §3</i>	
$(\cdot; \cdot)_{\mathcal{K}}, (\cdot; \cdot)$	L_2 inner-products over \mathcal{K} and $\tilde{\Omega}$, respectively
$\ \cdot\ _{\mathcal{K}}, \ \cdot\ $	L_2 norms over \mathcal{K} and $\tilde{\Omega}$, respectively
$\mathbf{w}_1, \mathbf{w}_2, q_1, q_2$	Weighting functions for velocities and pressures
$\mathbf{u}^*_1, \mathbf{u}^*_2, p^*_1, p^*_2$	Numerical fluxes, Eqs. (3.4)–(3.7)
$\{\cdot\}, [\cdot]$	Average and jump operators, Eqs. (2.11) & (2.13)
η_u, η_p	Stabilization parameters for jumps in velocities and pressures across interior edges, respectively; Eqs. (3.13)–(3.16)
<i>Constants in various estimates</i>	
$\mathcal{C}_{\text{drag},1}, \mathcal{C}_{\text{drag},2}$	Bounds on drag coefficients, Eq. (2.4)
$\mathcal{C}_{\mathbf{e}_{u_1}}, \mathcal{C}_{\mathbf{e}_{u_2}}$	Eqs. (4.19) & (4.20)
\mathcal{C}_{int}	Constant in standard estimate for interpolation error, Eq. (4.21)
\mathcal{C}_{inv}	Constant in discrete inverse inequality, Eq. (2.30)
\mathcal{C}_{lqu}	Locally quasi-uniform coefficient, §2.4 & Eq. (2.18)
\mathcal{C}_{sp}	Shape parameter, §2.4 & Eq. (2.17)
$\mathcal{C}_{\text{trace}}$	Constant in continuous trace inequality, Eqs. (2.28) & (2.29)
<i>Other symbols</i>	
$\mathcal{P}^m(\omega)$	Set of all polynomials over ω up to and including m -th order, §2.5
c, D	Concentration and diffusivity, §8
$m(\omega)$	Net rate of volumetric flux from element ω , §7.2
$m_{\text{max}}^{\text{out}}$	Maximum element-wise mass outflow flux, Eq. (7.3a)
$m_{\text{max}}^{\text{in}}$	Maximum element-wise mass inflow flux, Eq. (7.3b)

1. INTRODUCTION AND MOTIVATION

This paper presents a discontinuous Galerkin version of the continuous stabilized mixed formulation proposed recently by [Joodat et al., 2018] for the double porosity/permeability (DPP) mathematical model. The DPP model describes the flow of a single-phase incompressible fluid in a rigid porous medium with two distinct pore-networks with possible mass transfer across them. A derivation of the DPP model using the theory of interacting continua and continuum thermomechanics along with the mathematical properties that the solutions of this model satisfy are presented in [Nakshatrala et al., 2018].

The motivation for this work is twofold. *First*, due to the increasing interest in geo-materials with multiple pore-scales (e.g., vuggy carbonates and shales) and the development of new synthetic complex porous materials using advanced manufacturing techniques, understanding the flow of fluids in such porous materials is currently an active area of research. Darcy equations, which are commonly used for modeling flow of fluids in a porous medium with one single pore-network, are not adequate to accurately describe the flow dynamics in porous media with multiple pore-networks. Hence, it is required to develop new mathematical models and computational tools which can accurately capture the flow characteristics in complex porous media consisting of multiple pore-networks with possible mass transfer across them. For this purpose, [Nakshatrala et al., 2018] have recently proposed a mathematical model, which is capable of considering fluid flow through two pore-networks. This mathematical model will be referred to as the DPP model, which forms a basis for the current paper.

The *second* motivation behind the current paper is that the continuous Galerkin (CG) based formulations suffer from the so-called Gibbs phenomenon¹ when applied to problems with highly heterogeneous medium properties such as layered media; which manifests in the form of spurious oscillations (overshoots and undershoots) at the interface of a sharp change in medium properties (e.g., permeability). [Hughes et al., 2006] have clearly demonstrated that conventional continuous finite element methods for *Darcy equations* fall short in accurately capturing jumps in the solution fields at the location of material discontinuities. Since disparate medium properties are frequently encountered in subsurface modeling, the stabilized mixed four-field CG formulation recently proposed for DPP model [Joodat et al., 2018] will not be able to accurately capture the velocity profiles in highly heterogeneous porous media and will not suffice for realistic subsurface modeling. This will be clearly demonstrated using numerical simulations in a later section of this paper. We, therefore, develop a stabilized mixed DG formulation for the DPP model, which is robust, stable and capable of capturing possible jumps in the solution fields due to the existing disparate medium properties.

It is important to mention that one can also capture disparate medium properties and satisfy the LBB *inf-sup* stability condition [Brezzi and Fortin, 1991] by employing an element from the H(div) family; which include Raviart-Thomas spaces [Raviart and Thomas, 1977], Nédélec spaces [Nédélec, 1980] Brezzi-Douglas-Marini (BDM) spaces [Brezzi et al., 1985], Brezzi-Douglas-Fortin-Marini (BDFM) spaces [Brezzi et al., 1987] and Crouzeix-Raviart spaces [Crouzeix and Raviart, 1973]. Although there is an on-going debate on using H(div) elements vs. DG methods, the later do enjoy some unique desirable features. DG methods combine the attractive features of both finite element and finite volume methods. Application of completely discontinuous basis functions in the form of piecewise polynomials in DG methods provides them with the flexibility to support common non-conforming spaces (e.g., non-matching grids and hanging nodes, *h-p* adaptivity, variable degrees of local interpolations) and handle jumps in the profiles of variables [Cockburn, 2003; Li and Rivière, 2015, 2016; Rivière and Wheeler, 2002]. DG methods also enjoy high parallel efficiency. Unlike

¹ Traditionally, the Gibbs phenomenon is the manifestation of overshoots and undershoots in the representation of a simple discontinuity using the Fourier series. This phenomenon was first observed by [Wilbraham, 1848]. A mathematical explanation was later provided in the papers [Gibbs, 1898] and [Gibbs, 1899]; the former paper had a mistake which was corrected in the later. However, contrary to the traditional belief, one can observe undershoots and overshoots even when non-trigonometric functions are employed to approximate a simple discontinuous function in a least-squares sense. In particular, the “Gibbs phenomenon” can occur even under a piece-wise linear approximation [Foster and Richards, 1991].

the conventional continuous formulations, they are known to exhibit better local (or element-wise) mass balance [Hughes et al., 2006; Rivière, 2008].

The origins of DG methods can be traced back to [Lions, 1968] and [Nitsche, 1971]. One of the first successful applications of DG formulation to solve a practical problem was by [Reed and Hill, 1973], which addressed neutron transport. Over the years, DG methods have been successfully employed to solve hyperbolic PDEs [Brezzi et al., 2004; Pal et al., 2016], elliptic PDEs [Arnold et al., 2002; Barrios and Bustinza, 2007; Cockburn et al., 2009b; Douglas and Dupont, 1976; Rivière et al., 1999; Rusten et al., 1996], parabolic PDEs [Douglas and Dupont, 1976; Kulkarni et al., 2007], coupling algorithms [Nakshatrala et al., 2009] and space-time finite elements [Abedi et al., 2006; Palaniappan et al., 2004]. Several variants of DG formulations have been developed over the years with varying merits for each variant. Some popular variants are Runge-Kutta DG [Cockburn and Shu, 2001], local DG [Castillo et al., 2000], embedded DG [Güzey et al., 2007], compact DG [Peraire and Persson, 2008], hybridizable DG [Cockburn et al., 2009a] and adjoint-type variational multiscale DG [Badia and Codina, 2010; Hughes et al., 2006]. Although these variants may look very different, a unified framework has been laid out by [Arnold et al., 2002], to derive DG methods systematically, and these methods differ in their choices of numerical fluxes. However, to the best of authors' knowledge, there is no clear cut winner among these variants.

In this paper we employ the adjoint-type variational multiscale approach to develop a stabilized mixed four-field DG formulation for the DPP model. In order to circumvent the LBB *inf-sup* stability condition we add residual-based, adjoint-type stabilization terms defined over the elements. In order to avoid Gibbs phenomenon and at the same time maintain stability, we choose appropriate and consistent numerical fluxes, which are in the form of jumps and averages of the medium properties and solution fields. The resulting stabilized mixed DG formulation enjoys several attractive features, which include: (i) The formulation is capable of eliminating the spurious numerical instabilities in the profiles of solutions and capturing the existing jumps in the material properties. (ii) Equal-order interpolation for all the field variables, which is computationally preferred, is stable. (iii) The formulation is mathematically shown to be consistent, stable, and hence convergent. (iv) *A priori* error estimation is systematically obtained. (v) The DG formulation exhibits improved element-wise mass balance compared to its continuous counterpart. (vi) The formulation can be utilized to capture physical instabilities in heterogeneous porous media and to eliminate numerical instabilities at the same time.

The rest of this paper is organized as follows: Background material and preliminaries (including the governing equations of the mathematical model) are provided in Section 2. The proposed stabilized mixed DG formulation is presented in Section 3. A systematic convergence analysis and the error estimation of the proposed DG formulation are carried out in Section 4. Results of constant flow patch tests along with a sensitivity study on the stabilization parameters are presented in Section 5. Numerical convergence analysis and structure preserving properties are provided in Sections 6 and 7, respectively. In Section 8, the proposed DG formulation is implemented to study viscous-fingering-type physical instabilities in heterogeneous porous media with double pore-networks. Finally, conclusions are drawn in Section 9.

Throughout this paper, repeated indices do not imply summation.

2. BACKGROUND MATERIAL AND PRELIMINARIES

2.1. Governing equations². The DPP model deals with the flow of a single-phase incompressible fluid through a rigid porous medium with two pore-networks exhibiting different hydromechanical properties. We refer to these two pore-networks as macro-pore and micro-pore networks, which are denoted by subscripts 1 and 2, respectively. We denote the porous domain by $\Omega \subset \mathbb{R}^{nd}$, where “ nd ” represents the number of spatial dimensions. For a precise mathematical treatment, we assume that Ω is an open bounded domain. The boundary $\partial\Omega = \bar{\Omega} - \Omega$ is assumed to be smooth, where the superposed bar denotes the set closure. A spatial point is denoted by $\mathbf{x} \in \bar{\Omega}$. The gradient operator with respect to \mathbf{x} is denoted by $\text{grad}[\cdot]$ and the corresponding divergence operator is denoted by $\text{div}[\cdot]$. The unit outward normal to the boundary is denoted by $\hat{\mathbf{n}}(\mathbf{x})$. The pressure and the discharge (or Darcy) velocity fields in the macro-pore network are, respectively, denoted by $p_1(\mathbf{x})$ and $\mathbf{u}_1(\mathbf{x})$, and the corresponding fields in the micro-pore network are denoted by $p_2(\mathbf{x})$ and $\mathbf{u}_2(\mathbf{x})$. We denote the viscosity and true density of the fluid by μ and γ , respectively.

The abstract boundary value problem under the DPP model takes the following form: Find $\mathbf{u}_1(\mathbf{x})$, $\mathbf{u}_2(\mathbf{x})$, $p_1(\mathbf{x})$ and $p_2(\mathbf{x})$ such that

$$\mu k_1^{-1} \mathbf{u}_1(\mathbf{x}) + \text{grad}[p_1(\mathbf{x})] = \gamma \mathbf{b}(\mathbf{x}) \quad \text{in } \Omega \quad (2.1a)$$

$$\mu k_2^{-1} \mathbf{u}_2(\mathbf{x}) + \text{grad}[p_2(\mathbf{x})] = \gamma \mathbf{b}(\mathbf{x}) \quad \text{in } \Omega \quad (2.1b)$$

$$\text{div}[\mathbf{u}_1(\mathbf{x})] = +\chi(\mathbf{x}) \quad \text{in } \Omega \quad (2.1c)$$

$$\text{div}[\mathbf{u}_2(\mathbf{x})] = -\chi(\mathbf{x}) \quad \text{in } \Omega \quad (2.1d)$$

$$\chi(\mathbf{x}) = -\frac{\beta}{\mu} (p_1(\mathbf{x}) - p_2(\mathbf{x})) \quad \text{in } \Omega \quad (2.1e)$$

$$\mathbf{u}_1(\mathbf{x}) \cdot \hat{\mathbf{n}}(\mathbf{x}) = u_{n1}(\mathbf{x}) \quad \text{on } \Gamma_1^u \quad (2.1f)$$

$$\mathbf{u}_2(\mathbf{x}) \cdot \hat{\mathbf{n}}(\mathbf{x}) = u_{n2}(\mathbf{x}) \quad \text{on } \Gamma_2^u \quad (2.1g)$$

$$p_1(\mathbf{x}) = p_{01}(\mathbf{x}) \quad \text{on } \Gamma_1^p \quad (2.1h)$$

$$p_2(\mathbf{x}) = p_{02}(\mathbf{x}) \quad \text{on } \Gamma_2^p \quad (2.1i)$$

where $k_1(\mathbf{x})$ and $k_2(\mathbf{x})$, respectively, denote the (isotropic) permeabilities of the macro-pore and micro-pore networks, $\mathbf{b}(\mathbf{x})$ denotes the specific body force, and β is a dimensionless characteristic of the porous medium. $\chi(\mathbf{x})$ accounts for the mass exchange across the pore-networks and is the rate of volume transfer of the fluid between the two pore-networks per unit volume of the porous medium. The dimension of $\chi(\mathbf{x})$ is one over the time [$\text{M}^0\text{L}^0\text{T}^{-1}$]. Γ_i^u denotes that part of the boundary on which the normal component of velocity is prescribed in the macro-pore ($i = 1$) and micro-pore ($i = 2$) networks, and $u_{n1}(\mathbf{x})$ and $u_{n2}(\mathbf{x})$ denote the prescribed normal components of the velocities on Γ_1^u and Γ_2^u , respectively. Γ_i^p is that part of the boundary on which the pressure is prescribed in the macro-pore ($i = 1$) and micro-pore ($i = 2$) networks, and $p_{01}(\mathbf{x})$ and $p_{02}(\mathbf{x})$ denote the prescribed pressures on Γ_1^p and Γ_2^p , respectively.

For mathematical well-posedness, we assume that

$$\Gamma_1^u \cup \Gamma_1^p = \partial\Omega, \quad \Gamma_1^u \cap \Gamma_1^p = \emptyset, \quad \Gamma_2^u \cup \Gamma_2^p = \partial\Omega, \quad \text{and} \quad \Gamma_2^u \cap \Gamma_2^p = \emptyset \quad (2.2)$$

²This subsection on the governing equations, which will be similar to our earlier papers [Joodat et al., 2018; Nakshatrala et al., 2018], is provided to make this paper self-contained and for easy referencing.

However, if $\Gamma_1^p = \emptyset$ and $\Gamma_2^p = \emptyset$ hold simultaneously then one will be able to find the pressure in each pore-network only up to an arbitrary constant. We assume that the drag coefficients in the two pore-networks, μ/k_1 and μ/k_2 , are bounded below and above. That is,

$$0 < \inf_{\mathbf{x} \in \Omega} \frac{\mu}{k_i(\mathbf{x})} \leq \sup_{\mathbf{x} \in \Omega} \frac{\mu}{k_i(\mathbf{x})} < +\infty \quad i = 1, 2 \quad (2.3)$$

This also means that there exist two non-dimensional constants $1 \leq \mathcal{C}_{\text{drag},1}, \mathcal{C}_{\text{drag},2} < +\infty$ where

$$\mathcal{C}_{\text{drag},1} := \left(\sup_{\mathbf{x} \in \Omega} \frac{\mu}{k_1(\mathbf{x})} \right) \left(\inf_{\mathbf{x} \in \Omega} \frac{\mu}{k_1(\mathbf{x})} \right)^{-1} \quad \text{and} \quad \mathcal{C}_{\text{drag},2} := \left(\sup_{\mathbf{x} \in \Omega} \frac{\mu}{k_2(\mathbf{x})} \right) \left(\inf_{\mathbf{x} \in \Omega} \frac{\mu}{k_2(\mathbf{x})} \right)^{-1} \quad (2.4)$$

2.2. Geometrical definitions. The domain is partitioned into “*Nele*” subdomains, which will be elements in the context of the finite element method. These elements form a mesh on the domain. Mathematically, a mesh \mathcal{T} on Ω is a finite collection of disjoint polyhedra $\mathcal{T} = \{\omega^1, \dots, \omega^{Nele}\}$ such that

$$\overline{\Omega} = \bigcup_{i=1}^{Nele} \overline{\omega}^i \quad (2.5)$$

(Recall that an overline denotes the set closure.) We refer to ω^i as the i -th subdomain (element). The union of all open subdomains is denoted by

$$\tilde{\Omega} = \bigcup_{i=1}^{Nele} \omega^i \quad (2.6)$$

with the understanding that an integration over $\tilde{\Omega}$ is interpreted as follows:

$$\int_{\tilde{\Omega}} (\cdot) d\Omega = \sum_{i=1}^{Nele} \int_{\omega^i} (\cdot) d\Omega \quad (2.7)$$

The boundary of element ω^i is denoted by $\partial\omega^i := \overline{\omega}^i - \omega^i$. The set of all edges³ in the mesh is denoted by \mathcal{E} and the set of all interior edges is denoted by \mathcal{E}^{int} . The entire boundary of the skeleton of the mesh (i.e, the union of all the interior and exterior edges) is denoted by

$$\Gamma = \bigcup_{\Upsilon \in \mathcal{E}} \Upsilon \equiv \bigcup_{i=1}^{Nele} \partial\omega^i \quad (2.8)$$

The entire interior boundary (i.e., the union of all the interior edges) is denoted by

$$\Gamma^{\text{int}} = \bigcup_{\Upsilon \in \mathcal{E}^{\text{int}}} \Upsilon \equiv \Gamma \setminus \partial\Omega \quad (2.9)$$

Similar to the broken integral over $\tilde{\Omega}$ (i.e., equation (2.7)), the integral over Γ^{int} should be interpreted as follows:

$$\int_{\Gamma^{\text{int}}} (\cdot) d\Gamma = \sum_{\Upsilon \in \mathcal{E}^{\text{int}}} \int_{\Upsilon} (\cdot) d\Gamma \quad (2.10)$$

³For simplicity, we use “edge” to refer to a node in 1D, an edge in 2D and a face in 3D in the entire paper. The context will be clear from the particular discussion.

2.3. Average and jump operators. Consider an interior edge $\Upsilon \in \mathcal{E}^{\text{int}}$. We denote the elements that juxtapose Υ by ω_{Υ}^+ and ω_{Υ}^- . The unit normal vectors on this interior edge pointing outwards to ω_{Υ}^+ and ω_{Υ}^- are, respectively, denoted by $\widehat{\mathbf{n}}_{\Upsilon}^+$ and $\widehat{\mathbf{n}}_{\Upsilon}^-$ (see **Fig. 1**). The average $\{\!\{ \cdot \}\!\}$ and jump $\llbracket \cdot \rrbracket$ operators on Υ for a scalar field $\varphi(\mathbf{x})$ are, respectively, defined as follows:

$$\{\!\{ \varphi \}\!\} := \frac{1}{2} (\varphi_{\Upsilon}^+(\mathbf{x}) + \varphi_{\Upsilon}^-(\mathbf{x})) \quad \text{and} \quad \llbracket \varphi \rrbracket := \varphi_{\Upsilon}^+(\mathbf{x}) \widehat{\mathbf{n}}_{\Upsilon}^+(\mathbf{x}) + \varphi_{\Upsilon}^-(\mathbf{x}) \widehat{\mathbf{n}}_{\Upsilon}^-(\mathbf{x}) \quad \forall \mathbf{x} \in \Upsilon \quad (2.11)$$

where $\varphi_{\Upsilon}^+(\mathbf{x})$ and $\varphi_{\Upsilon}^-(\mathbf{x})$ are the restrictions of $\varphi(\mathbf{x})$ onto the elements ω_{Υ}^+ and ω_{Υ}^- , respectively. Mathematically,

$$\varphi_{\Upsilon}^+(\mathbf{x}) := \varphi(\mathbf{x})|_{\partial\omega_{\Upsilon}^+} \quad \text{and} \quad \varphi_{\Upsilon}^-(\mathbf{x}) := \varphi(\mathbf{x})|_{\partial\omega_{\Upsilon}^-} \quad \forall \mathbf{x} \in \Upsilon \quad (2.12)$$

For a vector field $\boldsymbol{\tau}(\mathbf{x})$, these operators on Υ are defined as follows:

$$\{\!\{ \boldsymbol{\tau} \}\!\} := \frac{1}{2} (\boldsymbol{\tau}_{\Upsilon}^+(\mathbf{x}) + \boldsymbol{\tau}_{\Upsilon}^-(\mathbf{x})) \quad \text{and} \quad \llbracket \boldsymbol{\tau} \rrbracket := \boldsymbol{\tau}_{\Upsilon}^+(\mathbf{x}) \cdot \widehat{\mathbf{n}}_{\Upsilon}^+(\mathbf{x}) + \boldsymbol{\tau}_{\Upsilon}^-(\mathbf{x}) \cdot \widehat{\mathbf{n}}_{\Upsilon}^-(\mathbf{x}) \quad \forall \mathbf{x} \in \Upsilon \quad (2.13)$$

where $\boldsymbol{\tau}_{\Upsilon}^+(\mathbf{x})$ and $\boldsymbol{\tau}_{\Upsilon}^-(\mathbf{x})$ are defined similar to equation (2.12). It is important to note that the jump operator acts on a scalar field to produce a vector field and vice-versa. It is also important to note that the above definitions are independent of the ordering of the elements. The following identity will be used in the rest of this paper:

$$\llbracket \varphi \boldsymbol{\tau} \rrbracket = \llbracket \boldsymbol{\tau} \rrbracket \{\!\{ \varphi \}\!\} + \{\!\{ \boldsymbol{\tau} \}\!\} \cdot \llbracket \varphi \rrbracket \quad (2.14)$$

2.4. Mesh-related quantities. We denote the *element diameter* (i.e., the length of the largest edge) of $\omega \in \mathcal{T}$ by h_{ω} . The maximum element diameter in a given mesh is referred to as *the mesh-size* and is denoted by:

$$h := \max_{\omega \in \mathcal{T}} h_{\omega} \quad (2.15)$$

We denote the *diameter of the inscribed circle* in $\omega \in \mathcal{T}$ by h_{ω}^{inc} (see **Fig. 2**). For an internal edge $\Upsilon \in \mathcal{E}^{\text{int}}$, shared by elements ω_{Υ}^+ and ω_{Υ}^- , we define the characteristic length h_{Υ} as follows:

$$h_{\Upsilon} = \frac{1}{2} (h_{\omega_{\Upsilon}^+} + h_{\omega_{\Upsilon}^-}) \quad (2.16)$$

For an external edge $\Upsilon \in \mathcal{E} \setminus \mathcal{E}^{\text{int}}$, h_{Υ} is set to be equal to the element diameter of the element containing the edge Υ .

We place two restrictions on a mesh, and we refer to a mesh satisfying these two restrictions as an *admissible mesh*.

- (i) The mesh is *shape regular* [Braess, 2007], which means that there exists a constant number \mathcal{C}_{sp} such that

$$\mathcal{C}_{\text{sp}} h_{\omega} \leq h_{\omega}^{\text{inc}} \quad \forall \omega \in \mathcal{T} \quad (2.17)$$

The constant \mathcal{C}_{sp} is commonly referred to as the *shape parameter*.

- (ii) The mesh is *locally quasi-uniform*, which also goes by the name *contact regularity* [Dolejší and Feistauer, 2015]. This condition requires that the element diameters of any two neighboring elements obey an equivalence relation. That is, there exists a constant number $\mathcal{C}_{\text{lqu}} > 0$ such that

$$\frac{1}{\mathcal{C}_{\text{lqu}}} h_{\omega_{\Upsilon}^+} \leq h_{\omega_{\Upsilon}^-} \leq \mathcal{C}_{\text{lqu}} h_{\omega_{\Upsilon}^+} \quad \forall \Upsilon \in \mathcal{E}^{\text{int}} \quad (2.18)$$

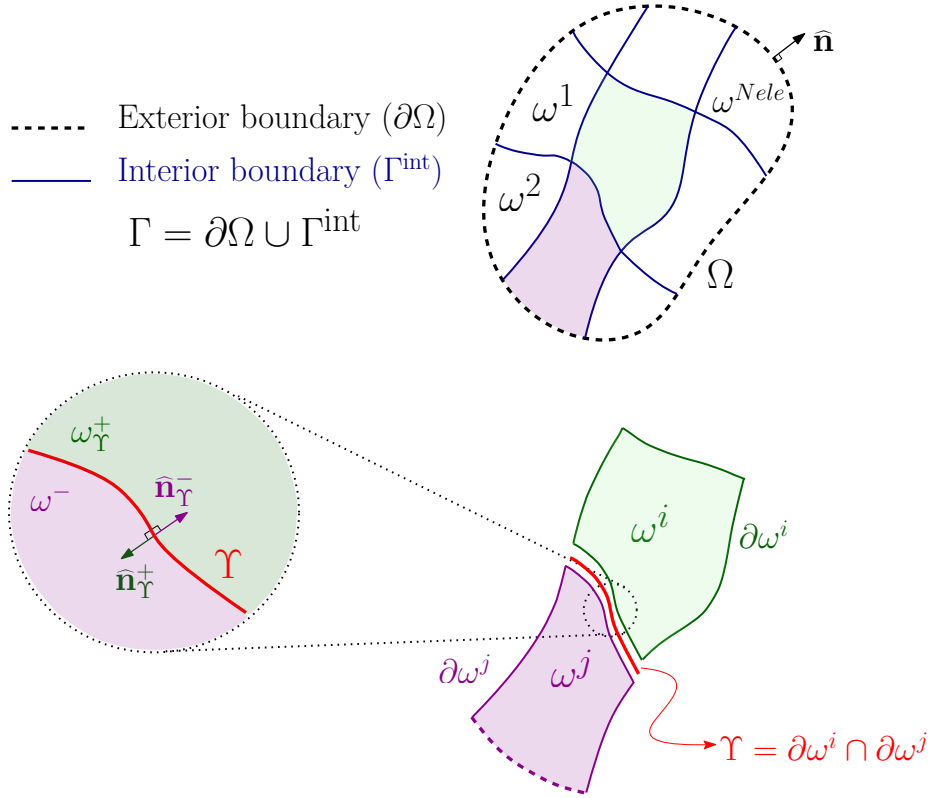


FIGURE 1. This figure shows the decomposition of the domain into subdomains (finite elements). External ($\partial\Omega$) and internal (Γ^{int}) boundaries of the domain, the shared interface (Υ) between two adjacent elements, as well as normal vectors to the boundaries are shown.

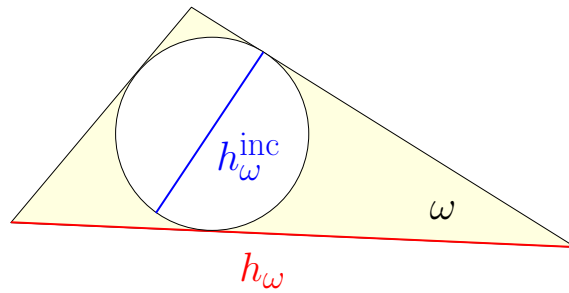


FIGURE 2. This figure illustrates the element diameter parameter h_ω and the diameter of the inscribed circle h_ω^{inc} for a typical element $\omega \in \mathcal{T}$.

The ordering of the neighboring elements (i.e., which element is “+” and which one is “-”) in the above inequality is arbitrary. This means that the above inequality holds even if ω_Υ^+ and ω_Υ^- are interchanged. The locally quasi-uniform condition implies the following useful bound:

$$\frac{1}{2} \left(1 + \frac{1}{\mathcal{C}_{\text{1qu}}} \right) h_{\omega_{\Upsilon}^+} \leq h_{\Upsilon} \leq \frac{1}{2} (1 + \mathcal{C}_{\text{1qu}}) h_{\omega_{\Upsilon}^+} \quad \forall \Upsilon \in \mathcal{E}^{\text{int}} \quad (2.19\text{a})$$

$$\frac{1}{2} \left(1 + \frac{1}{\mathcal{C}_{\text{1qu}}} \right) h_{\omega_{\Upsilon}^-} \leq h_{\Upsilon} \leq \frac{1}{2} (1 + \mathcal{C}_{\text{1qu}}) h_{\omega_{\Upsilon}^-} \quad \forall \Upsilon \in \mathcal{E}^{\text{int}} \quad (2.19\text{b})$$

A mesh \mathcal{T} with mesh-size h will be denoted by \mathcal{T}_h . A sequence of meshes will be denoted by $\mathcal{T}_{\mathcal{H}}$, where $\mathcal{H} = (0, \bar{h})$. $\mathcal{T}_{\mathcal{H}}$ is said to be an admissible sequence of meshes if \mathcal{T}_h is admissible for every $h \in \mathcal{H}$.

REMARK 2.1. *There are other notions of characteristic mesh sizes which are employed for DG methods. For example, an element length scale has been employed in [Hughes et al., 2006], which takes the following form under our notation:*

$$\hat{h} = \frac{\text{meas}(\omega_{\Upsilon}^+) + \text{meas}(\omega_{\Upsilon}^-)}{2 \text{meas}(\Upsilon)} \quad (2.20)$$

where $\text{meas}(\cdot)$ denotes the measure of a set. A good discussion on various mesh-based characteristic lengths can be found in [Dolejší and Feistauer, 2015].

2.5. Functional analysis aspects. We introduce the following broken Sobolev spaces (which are piece-wise discontinuous spaces):

$$\mathcal{U} := \left\{ \mathbf{u}(\mathbf{x}) \mid \mathbf{u}(\mathbf{x})|_{\omega^i} \in (L_2(\omega^i))^{\text{nd}}; \text{div}[\mathbf{u}] \in L_2(\omega^i); i = 1, \dots, \text{Nele} \right\} \quad (2.21\text{a})$$

$$\tilde{\mathcal{P}} := \left\{ p(\mathbf{x}) \mid p(\mathbf{x})|_{\omega^i} \in L_2(\omega^i); i = 1, \dots, \text{Nele} \right\} \quad (2.21\text{b})$$

$$\tilde{\mathcal{Q}} := \left\{ p(\mathbf{x}) \mid p(\mathbf{x})|_{\omega^i} \in H^1(\omega^i); i = 1, \dots, \text{Nele} \right\} \quad (2.21\text{c})$$

$$\mathcal{P} := \left\{ (p_1(\mathbf{x}), p_2(\mathbf{x})) \in \tilde{\mathcal{P}} \times \tilde{\mathcal{P}} \mid \left(\int_{\tilde{\Omega}} p_1(\mathbf{x}) d\Omega \right) \left(\int_{\tilde{\Omega}} p_2(\mathbf{x}) d\Omega \right) = 0 \right\} \quad (2.21\text{d})$$

$$\mathcal{Q} := \left\{ (p_1(\mathbf{x}), p_2(\mathbf{x})) \in \tilde{\mathcal{Q}} \times \tilde{\mathcal{Q}} \mid \left(\int_{\tilde{\Omega}} p_1(\mathbf{x}) d\Omega \right) \left(\int_{\tilde{\Omega}} p_2(\mathbf{x}) d\Omega \right) = 0 \right\} \quad (2.21\text{e})$$

where $L_2(\omega^i)$ denotes the set of all square-integrable functions defined on ω^i , and $H^1(\omega^i)$ is a standard Sobolev space [Evans, 1998].

REMARK 2.2. *The following condition in \mathcal{P} and \mathcal{Q} spaces (which is expressed in terms of the mean pressures in the two pore-networks):*

$$\left(\int_{\tilde{\Omega}} p_1(\mathbf{x}) d\Omega \right) \left(\int_{\tilde{\Omega}} p_2(\mathbf{x}) d\Omega \right) = 0$$

is one of the ways to fix the datum for the pressure. However, this condition is seldom employed in a numerical implementation. Alternatively, one can prescribe the pressure on a portion of the boundary in one of the pore-networks. For further details refer to [Joodat et al., 2018].

We denote the standard L_2 inner-product over a set \mathcal{K} by $(\cdot; \cdot)_{\mathcal{K}}$. That is,

$$(a; b)_{\mathcal{K}} := \int_{\mathcal{K}} a \cdot b \, d\mathcal{K} \quad (2.22)$$

and the associated standard L_2 norm is denoted by $\| \cdot \|_{\mathcal{K}}$ as follows:

$$\|a\|_{\mathcal{K}} = \sqrt{(a; a)_{\mathcal{K}}} \quad (2.23)$$

The subscript in the L_2 inner-product and the associated norm will be dropped if $\mathcal{K} = \tilde{\Omega}$.

In a subsequent section on the interpolation error, we employ a general order Sobolev semi-norm. To this end, let $\alpha = (\alpha_1, \dots, \alpha_{nd}) \in \mathbb{N}^{nd}$ be a nd -tuple (i.e., multi-index), the order of which is denoted by $|\alpha| := \sum_{i=1}^{nd} \alpha_i$. We denote the multi-index (classical or distributional) partial derivative by $D^\alpha(\cdot)$. For a scalar function $\varphi(\mathbf{x}) \in C_c^\infty(\mathcal{K})$ (which is a set of infinitely differentiable functions with compact support in \mathcal{K}) [Evans, 1998], the multi-index (classical) partial derivative with respect to a given coordinate system $\mathbf{x} = (x_1, \dots, x_{nd})$ is defined as follows:

$$D^\alpha \varphi(\mathbf{x}) := \frac{\partial^{|\alpha|} \varphi(\mathbf{x})}{\partial x_1^{\alpha_1} \partial x_2^{\alpha_2} \dots \partial x_{nd}^{\alpha_{nd}}} \quad (2.24)$$

Then, the multi-index distributional partial derivative of a scalar field $a : \mathcal{K} \rightarrow \mathbb{R}$ is defined as follows:

$$(D^\alpha a(\mathbf{x}); \varphi(\mathbf{x}))_{\mathcal{K}} := (-1)^{|\alpha|} (a(\mathbf{x}); D^\alpha \varphi(\mathbf{x}))_{\mathcal{K}} \quad \forall \varphi(\mathbf{x}) \in C_c^\infty(\mathcal{K}) \quad (2.25)$$

For a scalar field $a : \mathcal{K} \rightarrow \mathbb{R}$, the s -th order Sobolev semi-norm over \mathcal{K} is defined as follows:

$$|a|_{H^s(\mathcal{K})} := \left(\sum_{|\alpha|=s} \|D^\alpha a(\mathbf{x})\|_{\mathcal{K}}^2 \right)^{1/2} \quad (2.26)$$

and for a vector field $\mathbf{a} : \mathcal{K} \rightarrow \mathbb{R}^{nd}$ with scalar components a_i ($i = 1, \dots, nd$), the corresponding semi-norm is defined as follows:

$$|\mathbf{a}|_{H^s(\mathcal{K})} := \left(\sum_{i=1}^{nd} |a_i|_{H^s(\mathcal{K})}^2 \right)^{1/2} \quad (2.27)$$

2.5.1. *Inverse and trace inequalities*⁴. The inequalities given below play a crucial role in obtaining bounds on the error due to terms defined on the element interface. Mathematical proofs to these estimates can be found in [Arnold, 1982; Dolejší and Feistauer, 2015; Pietro and Ern, 2011; Verfürth, 2013].

LEMMA 2.1. (*Continuous trace inequality.*) For an admissible mesh \mathcal{T}_h , the following estimates hold $\forall \omega \in \mathcal{T}_h$:

$$\|v\|_{\partial\omega} \leq \mathcal{C}_{\text{trace}} \left(\frac{1}{\sqrt{h_\omega}} \|v\|_\omega + \sqrt{h_\omega} \|\text{grad}[v]\|_\omega \right) \quad \forall v(\mathbf{x}) \in H^1(\omega) \quad (2.28)$$

$$\|\mathbf{v}\|_{\partial\omega} \leq \mathcal{C}_{\text{trace}} \left(\frac{1}{\sqrt{h_\omega}} \|\mathbf{v}\|_\omega + \sqrt{h_\omega} \|\text{grad}[\mathbf{v}]\|_\omega \right) \quad \forall \mathbf{v}(\mathbf{x}) \in (H^1(\omega))^{nd} \quad (2.29)$$

where the $\mathcal{C}_{\text{trace}}$ depends on the shape parameter (i.e., \mathcal{C}_{sp}) and the number of spatial dimensions (nd) but it is not dependent on h_ω .

Let $\mathcal{P}^m(\omega)$ denote the set of all polynomials up to and including m -th order over $\omega \in \mathcal{T}_h$. We then have the following discrete inequalities.

⁴For these results we assume that the velocity fields belong to $(H^1(\omega))^{nd}$ instead of $H(\text{div}, \omega)$, which was the case in the function space (2.21a). The reason is that one has to deal with half-Sobolev spaces and corresponding dual spaces (i.e., negative half-spaces) for trace inequalities under $H(\text{div})$; which makes the convergence and error analyses more involved. Moreover, the authors are not aware of any discrete trace inequalities available in the mathematical analysis literature that can be easily used under half-Sobolev spaces.

LEMMA 2.2. (*Discrete inverse inequality.*) Let \mathcal{T}_h be an admissible mesh. Then the following estimates hold $\forall \omega \in \mathcal{T}_h$:

$$\|\text{grad}[v^h]\|_\omega \leq \mathcal{C}_{\text{inv}} h_\omega^{-1} \|v^h\|_\omega \quad \forall v^h(\mathbf{x}) \in H^1(\omega) \cap \mathcal{P}^m(\omega) \quad (2.30)$$

$$\|\text{grad}[\mathbf{v}^h]\|_\omega \leq \mathcal{C}_{\text{inv}} h_\omega^{-1} \|\mathbf{v}^h\|_\omega \quad \forall \mathbf{v}^h(\mathbf{x}) \in (H^1(\omega))^{nd} \cap (\mathcal{P}^m(\omega))^{nd} \quad (2.31)$$

where \mathcal{C}_{inv} is a constant dependent on the shape parameter (\mathcal{C}_{sp}), the number of spatial dimensions (nd) and the polynomial order (m), but it does not depend on h_ω or on the fields $v^h(\mathbf{x})$ and $\mathbf{v}^h(\mathbf{x})$.

LEMMA 2.3. (*Discrete trace inequality.*) For an admissible mesh \mathcal{T}_h , the following estimates hold $\forall \omega \in \mathcal{T}_h$:

$$\|v^h\|_{\partial\omega} \leq \mathcal{C}_{\text{trace}} (1 + \mathcal{C}_{\text{inv}}) \frac{1}{\sqrt{h_\omega}} \|v^h\|_\omega \quad \forall v^h(\mathbf{x}) \in H^1(\omega) \cap \mathcal{P}^m(\omega) \quad (2.32)$$

$$\|\mathbf{v}^h\|_{\partial\omega} \leq \mathcal{C}_{\text{trace}} (1 + \mathcal{C}_{\text{inv}}) \frac{1}{\sqrt{h_\omega}} \|\mathbf{v}^h\|_\omega \quad \forall \mathbf{v}^h(\mathbf{x}) \in (H^1(\omega))^{nd} \cap (\mathcal{P}^m(\omega))^{nd} \quad (2.33)$$

3. A STABILIZED MIXED DG FORMULATION

We propose a stabilized *four-field* formulation for the DPP model. The proposed formulation draws its inspiration from the stabilized *two-field* formulations proposed by [Badia and Codina, 2010; Hughes et al., 2006] for Darcy equations, which describe the flow of an incompressible fluid through a porous medium with a single pore-network.

3.1. Weak form in terms of numerical fluxes. Multiplying the governing equations (2.1a)–(2.1d) by weighting functions, integrating over an element ω , and using equation (2.1e) and the divergence theorem, we obtain the following:

$$\begin{aligned} & (\mathbf{w}_1; \mu k_1^{-1} \mathbf{u}_1)_\omega - (\text{div}[\mathbf{w}_1]; p_1)_\omega + \left(\mathbf{w}_1 \cdot \hat{\mathbf{n}}; \overset{*}{p}_1 \right)_{\partial\omega} + (\mathbf{w}_2; \mu k_2^{-1} \mathbf{u}_2)_\omega - (\text{div}[\mathbf{w}_2]; p_2)_\omega + \left(\mathbf{w}_2 \cdot \hat{\mathbf{n}}; \overset{*}{p}_2 \right)_{\partial\omega} \\ & + (q_1; \text{div}[\mathbf{u}_1])_\omega + \left(q_1; \left(\overset{*}{\mathbf{u}}_1 - \mathbf{u}_1 \right) \cdot \hat{\mathbf{n}} \right)_{\partial\omega} + (q_2; \text{div}[\mathbf{u}_2])_\omega + \left(q_2; \left(\overset{*}{\mathbf{u}}_2 - \mathbf{u}_2 \right) \cdot \hat{\mathbf{n}} \right)_{\partial\omega} \\ & + \left(q_1 - q_2; \frac{\beta}{\mu} (p_1 - p_2) \right)_\omega = (\mathbf{w}_1; \gamma \mathbf{b}_1)_\omega + (\mathbf{w}_2; \gamma \mathbf{b}_2)_\omega \end{aligned} \quad (3.1)$$

where $\overset{*}{p}_1$ and $\overset{*}{p}_2$ are the numerical fluxes for the pressures and $\overset{*}{\mathbf{u}}_1$ and $\overset{*}{\mathbf{u}}_2$ are the numerical fluxes for the velocities. Summing the above equation over all the elements and using the identity (2.14), we obtain the following weak form in terms of numerical fluxes:

$$\begin{aligned} & (\mathbf{w}_1; \mu k_1^{-1} \mathbf{u}_1) - (\text{div}[\mathbf{w}_1]; p_1) + \left(\{\!\{ \mathbf{w}_1 \}\!\}; \{\!\{ \overset{*}{p}_1 \}\!\} \right)_{\Gamma^{\text{int}}} + \left(\llbracket \mathbf{w}_1 \rrbracket; \{\!\{ \overset{*}{p}_1 \}\!\} \right)_{\Gamma^{\text{int}}} + \left(\mathbf{w}_1 \cdot \hat{\mathbf{n}}; \overset{*}{p}_1 \right)_{\partial\Omega} \\ & + (\mathbf{w}_2; \mu k_2^{-1} \mathbf{u}_2) - (\text{div}[\mathbf{w}_2]; p_2) + \left(\{\!\{ \mathbf{w}_2 \}\!\}; \{\!\{ \overset{*}{p}_2 \}\!\} \right)_{\Gamma^{\text{int}}} + \left(\llbracket \mathbf{w}_2 \rrbracket; \{\!\{ \overset{*}{p}_2 \}\!\} \right)_{\Gamma^{\text{int}}} + \left(\mathbf{w}_2 \cdot \hat{\mathbf{n}}; \overset{*}{p}_2 \right)_{\partial\Omega} \\ & + (q_1; \text{div}[\mathbf{u}_1]) + \left(\{\!\{ q_1 \}\!\}; \llbracket \overset{*}{\mathbf{u}}_1 \rrbracket - \llbracket \mathbf{u}_1 \rrbracket \right)_{\Gamma^{\text{int}}} + \left(\llbracket q_1 \rrbracket; \{\!\{ \overset{*}{\mathbf{u}}_1 \}\!\} - \{\!\{ \mathbf{u}_1 \}\!\} \right)_{\Gamma^{\text{int}}} + \left(q_1; \left(\overset{*}{\mathbf{u}}_1 - \mathbf{u}_1 \right) \cdot \hat{\mathbf{n}} \right)_{\partial\Omega} \\ & + (q_2; \text{div}[\mathbf{u}_2]) + \left(\{\!\{ q_2 \}\!\}; \llbracket \overset{*}{\mathbf{u}}_2 \rrbracket - \llbracket \mathbf{u}_2 \rrbracket \right)_{\Gamma^{\text{int}}} + \left(\llbracket q_2 \rrbracket; \{\!\{ \overset{*}{\mathbf{u}}_2 \}\!\} - \{\!\{ \mathbf{u}_2 \}\!\} \right)_{\Gamma^{\text{int}}} + \left(q_2; \left(\overset{*}{\mathbf{u}}_2 - \mathbf{u}_2 \right) \cdot \hat{\mathbf{n}} \right)_{\partial\Omega} \\ & + \left(q_1 - q_2; \frac{\beta}{\mu} (p_1 - p_2) \right) = (\mathbf{w}_1; \gamma \mathbf{b}_1) + (\mathbf{w}_2; \gamma \mathbf{b}_2) \end{aligned} \quad (3.2)$$

Physically, the jumps in pressures and the normal component of velocities should vanish on any curve which is entirely inside the domain, and in particular, on any interior edge. That is,

$$\llbracket p_1 \rrbracket = \mathbf{0}, \llbracket p_2 \rrbracket = \mathbf{0}, \llbracket \mathbf{u}_1 \rrbracket = 0 \text{ and } \llbracket \mathbf{u}_2 \rrbracket = 0 \quad \text{on } \Gamma^{\text{int}} \quad (3.3)$$

Numerical fluxes are important components of DG methods, which have to be selected carefully. The choice of these numerical fluxes can greatly affect the stability of a DG formulation. Herein, we consider the following general expressions for the numerical fluxes:

$$\star p_1 = \begin{cases} \lambda_1^{(1)} \{\{p_1\}\} + \frac{\lambda_1^{(2)}}{2} \llbracket p_1 \rrbracket \cdot \hat{\mathbf{n}} + \lambda_1^{(3)} \llbracket \mathbf{u}_1 \rrbracket & \text{on } \Gamma^{\text{int}} \\ p_1 & \text{on } \Gamma_1^u \\ p_{01} & \text{on } \Gamma_1^p \end{cases} \quad (3.4)$$

$$\star p_2 = \begin{cases} \lambda_2^{(1)} \{\{p_2\}\} + \frac{\lambda_2^{(2)}}{2} \llbracket p_2 \rrbracket \cdot \hat{\mathbf{n}} + \lambda_2^{(3)} \llbracket \mathbf{u}_2 \rrbracket & \text{on } \Gamma^{\text{int}} \\ p_2 & \text{on } \Gamma_2^u \\ p_{02} & \text{on } \Gamma_2^p \end{cases} \quad (3.5)$$

$$\star \mathbf{u}_1 = \Lambda_1^{(1)} \{\{\mathbf{u}_1\}\} + \frac{\Lambda_1^{(2)}}{2} \llbracket \mathbf{u}_1 \rrbracket \hat{\mathbf{n}} + \Lambda_1^{(3)} \llbracket p_1 \rrbracket \quad \text{on } \Gamma^{\text{int}} \quad (3.6a)$$

$$\star \mathbf{u}_1 \cdot \hat{\mathbf{n}} = \begin{cases} u_{n1} & \text{on } \Gamma_1^u \\ \mathbf{u}_1 \cdot \hat{\mathbf{n}} & \text{on } \Gamma_1^p \end{cases} \quad (3.6b)$$

$$\star \mathbf{u}_2 = \Lambda_2^{(1)} \{\{\mathbf{u}_2\}\} + \frac{\Lambda_2^{(2)}}{2} \llbracket \mathbf{u}_2 \rrbracket \hat{\mathbf{n}} + \Lambda_2^{(3)} \llbracket p_2 \rrbracket \quad \text{on } \Gamma^{\text{int}} \quad (3.7a)$$

$$\star \mathbf{u}_2 \cdot \hat{\mathbf{n}} = \begin{cases} u_{n2} & \text{on } \Gamma_2^u \\ \mathbf{u}_2 \cdot \hat{\mathbf{n}} & \text{on } \Gamma_2^p \end{cases} \quad (3.7b)$$

where $\lambda_i^{(j)}$ and $\Lambda_i^{(j)}$ ($i, j = 1$ or 2) are constants. It is easy to check that these numerical fluxes satisfy the following relations on Γ^{int} :

$$\{\{\star p_1\}\} = \lambda_1^{(1)} \{\{p_1\}\} + \lambda_1^{(3)} \llbracket \mathbf{u}_1 \rrbracket \quad \text{and} \quad \llbracket \star p_1 \rrbracket = \lambda_1^{(2)} \llbracket p_1 \rrbracket \quad (3.8a)$$

$$\{\{\star p_2\}\} = \lambda_2^{(1)} \{\{p_2\}\} + \lambda_2^{(3)} \llbracket \mathbf{u}_2 \rrbracket \quad \text{and} \quad \llbracket \star p_2 \rrbracket = \lambda_2^{(2)} \llbracket p_2 \rrbracket \quad (3.8b)$$

$$\{\{\star \mathbf{u}_1\}\} = \Lambda_1^{(1)} \{\{\mathbf{u}_1\}\} + \Lambda_1^{(3)} \llbracket p_1 \rrbracket \quad \text{and} \quad \llbracket \star \mathbf{u}_1 \rrbracket = \Lambda_1^{(2)} \llbracket \mathbf{u}_1 \rrbracket \quad (3.8c)$$

$$\{\{\star \mathbf{u}_2\}\} = \Lambda_2^{(1)} \{\{\mathbf{u}_2\}\} + \Lambda_2^{(3)} \llbracket p_2 \rrbracket \quad \text{and} \quad \llbracket \star \mathbf{u}_2 \rrbracket = \Lambda_2^{(2)} \llbracket \mathbf{u}_2 \rrbracket \quad (3.8d)$$

3.2. The classical mixed DG formulation. This formulation is based on the Galerkin formalism and can be obtained by making the following choices:

$$\lambda_1^{(1)} = \lambda_2^{(1)} = \Lambda_1^{(1)} = \Lambda_2^{(1)} = 1 \quad (3.9)$$

and the other constants in equations (3.4)–(3.7) are taken to be zeros. The numerical fluxes on Γ^{int} under the classical mixed DG formulation take the following form:

$$\star p_1 = \{\{p_1\}\}, \quad \star p_2 = \{\{p_2\}\}, \quad \star \mathbf{u}_1 = \{\{\mathbf{u}_1\}\} \quad \text{and} \quad \star \mathbf{u}_2 = \{\{\mathbf{u}_2\}\} \quad (3.10)$$

The above numerical fluxes are similar to the ones employed by [Bassi and Rebay, 1997], which are known to be consistent but do not result in a stable DG method [Arnold et al., 2002]. The corresponding weak formulation reads: Find $(\mathbf{u}_1(\mathbf{x}), \mathbf{u}_2(\mathbf{x})) \in \mathcal{U} \times \mathcal{U}$, $(p_1(\mathbf{x}), p_2(\mathbf{x})) \in \mathcal{P}$ such that we have

$$\begin{aligned} \mathcal{B}_{\text{Gal}}^{\text{DG}}(\mathbf{w}_1, \mathbf{w}_2, q_1, q_2; \mathbf{u}_1, \mathbf{u}_2, p_1, p_2) &= \mathcal{L}_{\text{Gal}}^{\text{DG}}(\mathbf{w}_1, \mathbf{w}_2, q_1, q_2) \\ \forall (\mathbf{w}_1(\mathbf{x}), \mathbf{w}_2(\mathbf{x})) \in \mathcal{U} \times \mathcal{U}, (q_1(\mathbf{x}), q_2(\mathbf{x})) \in \mathcal{P} & \end{aligned} \quad (3.11)$$

where the bilinear form and the linear functional are, respectively, defined as follows:

$$\begin{aligned} \mathcal{B}_{\text{Gal}}^{\text{DG}} := & (\mathbf{w}_1; \mu k_1^{-1} \mathbf{u}_1) - (\text{div}[\mathbf{w}_1]; p_1) + (q_1; \text{div}[\mathbf{u}_1]) + (\llbracket \mathbf{w}_1 \rrbracket; \{\{p_1\}\})_{\Gamma^{\text{int}}} - (\{\{q_1\}\}; \llbracket \mathbf{u}_1 \rrbracket)_{\Gamma^{\text{int}}} \\ & + (\mathbf{w}_2; \mu k_2^{-1} \mathbf{u}_2) - (\text{div}[\mathbf{w}_2]; p_2) + (q_2; \text{div}[\mathbf{u}_2]) + (\llbracket \mathbf{w}_2 \rrbracket; \{\{p_2\}\})_{\Gamma^{\text{int}}} - (\{\{q_2\}\}; \llbracket \mathbf{u}_2 \rrbracket)_{\Gamma^{\text{int}}} \\ & + \left(q_1 - q_2; \frac{\beta}{\mu} (p_1 - p_2) \right) + (\mathbf{w}_1 \cdot \hat{\mathbf{n}}; p_1)_{\Gamma_1^u} + (\mathbf{w}_2 \cdot \hat{\mathbf{n}}; p_2)_{\Gamma_2^u} - (q_1; \mathbf{u}_1 \cdot \hat{\mathbf{n}})_{\Gamma_1^u} - (q_2; \mathbf{u}_2 \cdot \hat{\mathbf{n}})_{\Gamma_2^u} \end{aligned} \quad (3.12a)$$

$$\mathcal{L}_{\text{Gal}}^{\text{DG}} := (\mathbf{w}_1; \gamma \mathbf{b}_1) + (\mathbf{w}_2; \gamma \mathbf{b}_2) - (\mathbf{w}_1 \cdot \hat{\mathbf{n}}; p_{01})_{\Gamma_1^p} - (\mathbf{w}_2 \cdot \hat{\mathbf{n}}; p_{02})_{\Gamma_2^p} - (q_1; u_{n1})_{\Gamma_1^u} - (q_2; u_{n2})_{\Gamma_2^u} \quad (3.12b)$$

The classical mixed DG formulation is not stable under all combinations of interpolation functions for the field variables, which is due to the violation of the LBB *inf-sup* stability condition [Brezzi and Fortin, 1991]. Specifically, equal-order interpolation for all the field variables is not stable under the classical mixed DG formulation. This numerical instability (due to the interpolation functions) is different from the aforementioned instability due to the numerical fluxes (i.e., Bassi-Rebay DG method). We develop a stabilized mixed DG formulation which does not suffer from any of the aforementioned instabilities. This is achieved by adding adjoint-type, residual-based stabilization terms (which are defined over the subdomains and circumvent the LBB *inf-sup* stability condition) and by incorporating appropriate numerical fluxes (which are consistent and stable and are defined along the subdomain interfaces).

3.3. Proposed stabilized mixed DG formulation. This formulation makes the following choices:

$$\lambda_1^{(1)} = \lambda_2^{(1)} = 1, \quad \lambda_1^{(3)} = \eta_u h_\Upsilon \{\{\mu k_1^{-1}\}\} \text{ and } \lambda_2^{(3)} = \eta_u h_\Upsilon \{\{\mu k_2^{-1}\}\} \quad (3.13a)$$

$$\Lambda_1^{(1)} = \Lambda_2^{(1)} = 1, \quad \Lambda_1^{(3)} = \frac{\eta_p}{h_\Upsilon} \{\{\mu^{-1} k_1\}\} \text{ and } \Lambda_2^{(3)} = \frac{\eta_p}{h_\Upsilon} \{\{\mu^{-1} k_2\}\} \quad (3.13b)$$

and the other constants in equations (3.4)–(3.7) are taken to be zero. η_u and η_p are non-negative, non-dimensional bounded constants. The corresponding numerical fluxes on Γ^{int} take the following form:

$$\begin{aligned} \overset{*}{p}_1 &= \{\{p_1\}\} + \eta_u h_\Upsilon \{\{\mu k_1^{-1}\}\} \llbracket \mathbf{u}_1 \rrbracket, \quad \overset{*}{p}_2 = \{\{p_2\}\} + \eta_u h_\Upsilon \{\{\mu k_2^{-1}\}\} \llbracket \mathbf{u}_2 \rrbracket, \\ \overset{*}{\mathbf{u}}_1 &= \llbracket \mathbf{u}_1 \rrbracket + \frac{\eta_p}{h_\Upsilon} \{\{\mu^{-1} k_1\}\} \llbracket p_1 \rrbracket \text{ and } \overset{*}{\mathbf{u}}_2 = \llbracket \mathbf{u}_2 \rrbracket + \frac{\eta_p}{h_\Upsilon} \{\{\mu^{-1} k_2\}\} \llbracket p_2 \rrbracket \end{aligned} \quad (3.14)$$

The mathematical statement of the proposed stabilized mixed DG formulation reads as follows: Find $(\mathbf{u}_1(\mathbf{x}), \mathbf{u}_2(\mathbf{x})) \in \mathcal{U} \times \mathcal{U}$, $(p_1(\mathbf{x}), p_2(\mathbf{x})) \in \mathcal{Q}$ such that we have

$$\begin{aligned} \mathcal{B}_{\text{stab}}^{\text{DG}}(\mathbf{w}_1, \mathbf{w}_2, q_1, q_2; \mathbf{u}_1, \mathbf{u}_2, p_1, p_2) &= \mathcal{L}_{\text{stab}}^{\text{DG}}(\mathbf{w}_1, \mathbf{w}_2, q_1, q_2) \\ \forall (\mathbf{w}_1(\mathbf{x}), \mathbf{w}_2(\mathbf{x})) \in \mathcal{U} \times \mathcal{U}, (q_1(\mathbf{x}), q_2(\mathbf{x})) \in \mathcal{Q} \end{aligned} \quad (3.15)$$

where the bilinear form and the linear functional are, respectively, defined as follows:

$$\begin{aligned} \mathcal{B}_{\text{stab}}^{\text{DG}} := & \mathcal{B}_{\text{Gal}}^{\text{DG}} - \frac{1}{2} (\mu k_1^{-1} \mathbf{w}_1 - \text{grad}[q_1]; \mu^{-1} k_1 (\mu k_1^{-1} \mathbf{u}_1 + \text{grad}[p_1])) \\ & - \frac{1}{2} (\mu k_2^{-1} \mathbf{w}_2 - \text{grad}[q_2]; \mu^{-1} k_2 (\mu k_2^{-1} \mathbf{u}_2 + \text{grad}[p_2])) \\ & + (\eta_u h_\Upsilon \{\{\mu k_1^{-1}\}\} \llbracket \mathbf{w}_1 \rrbracket; \llbracket \mathbf{u}_1 \rrbracket)_{\Gamma^{\text{int}}} + (\eta_u h_\Upsilon \{\{\mu k_2^{-1}\}\} \llbracket \mathbf{w}_2 \rrbracket; \llbracket \mathbf{u}_2 \rrbracket)_{\Gamma^{\text{int}}} \end{aligned}$$

$$+ \left(\frac{\eta_p}{h_\Upsilon} \{ \mu^{-1} k_1 \} \llbracket q_1 \rrbracket; \llbracket p_1 \rrbracket \right)_{\Gamma^{\text{int}}} + \left(\frac{\eta_p}{h_\Upsilon} \{ \mu^{-1} k_2 \} \llbracket q_2 \rrbracket; \llbracket p_2 \rrbracket \right)_{\Gamma^{\text{int}}} \quad (3.16a)$$

$$\mathcal{L}_{\text{stab}}^{\text{DG}} := \mathcal{L}_{\text{Gal}}^{\text{DG}} - \frac{1}{2} (\mu k_1^{-1} \mathbf{w}_1 - \text{grad}[q_1]; \mu^{-1} k_1 \gamma \mathbf{b}_1) - \frac{1}{2} (\mu k_2^{-1} \mathbf{w}_2 - \text{grad}[q_2]; \mu^{-1} k_2 \gamma \mathbf{b}_2) \quad (3.16b)$$

To completely define the formulation, the parameters η_u and η_p have to be prescribed. We make the following recommendation, which is based on the theoretical convergence analysis (see §4) and extensive numerical simulations (see §5–§8):

- (i) For conforming approximations, the parameters can be taken to be $\eta_u = \eta_p = 0$.
- (ii) For non-conforming approximations, the parameters can be taken to be $\eta_u = \eta_p = 10$ or 100. (See § 5.2.1).

A few remarks about the stabilized formulation are in order.

- (a) The above stabilized formulation is an adjoint-type formulation. We have posed even the classical mixed formulation as an adjoint-type (see the bilinear form (3.12a)). In addition, the stabilization terms within the elements (i.e., in $\tilde{\Omega}$) are of adjoint-type, which look similar to the one proposed by [Hughes et al., 2006] for the **two-field** Darcy equations.
- (b) Since the formulation is of adjoint-type, the formulation will not give rise to symmetric coefficient (“stiffness”) matrix. But the coefficient matrix will be positive definite, which can be inferred from Lemma 4.1. Alternatively, the above stabilized formulation can be posed as an equivalent symmetric formulation by replacing q_1 and q_2 with $-q_1$ and $-q_2$, respectively; which is justified as q_1 and q_2 are arbitrary weighting functions. In this case, the resulting symmetric formulation will not result in positive-definite coefficient matrix.
- (c) In order to minimize the drift in the solution fields, especially in the case of non-conforming discretization, additional stabilization terms on the interior boundaries (i.e., terms containing η_u and η_p) are required in both networks. The necessity of employing such stabilization parameters has been addressed by [Badia and Codina, 2010] for the case of Darcy equations. It is noteworthy that η_u parameter was not included in the formulation proposed by [Hughes et al., 2006], as they did not consider non-conforming approximations.
- (d) Due to the presence of the terms containing η_u and η_p , the above numerical fluxes are no longer similar to the ones proposed by [Bassi and Rebay, 1997]. The numerical fluxes employed in the proposed formulation are not the same as any of the DG methods discussed in the review paper [Arnold et al., 2002].
- (e) In the case of Darcy equations, a stabilized formulation without edge stabilization terms has been developed and its convergence has been established by utilizing a lifting operator [Brezzi et al., 2005]. The question about whether such an approach can be extended to the DPP model is worthy of an investigation, but is beyond the scope of this paper.

4. A THEORETICAL ANALYSIS OF THE PROPOSED DG FORMULATION

We start by grouping the field variables and their corresponding weighting functions as follows:

$$\mathbf{U} = (\mathbf{u}_1(\mathbf{x}), \mathbf{u}_2(\mathbf{x}), p_1(\mathbf{x}), p_2(\mathbf{x})) \in \mathbb{U} \quad (4.1a)$$

$$\mathbf{W} = (\mathbf{w}_1(\mathbf{x}), \mathbf{w}_2(\mathbf{x}), q_1(\mathbf{x}), q_2(\mathbf{x})) \in \mathbb{U} \quad (4.1b)$$

where the product space \mathbb{U} is defined as follows:

$$\mathbb{U} = \mathcal{U} \times \mathcal{U} \times \mathcal{Q} \quad (4.2)$$

The proposed stabilized mixed DG formulation (3.15) can then be compactly written as follows: Find $\mathbf{U} \in \mathbb{U}$ such that we have

$$\mathcal{B}_{\text{stab}}^{\text{DG}}(\mathbf{W}; \mathbf{U}) = \mathcal{L}_{\text{stab}}^{\text{DG}}(\mathbf{W}) \quad \forall \mathbf{W} \in \mathbb{U} \quad (4.3)$$

The stability of the proposed weak formulation will be established under the following norm:

$$\begin{aligned} (\|\mathbf{W}\|_{\text{stab}}^{\text{DG}})^2 := \mathcal{B}_{\text{stab}}^{\text{DG}}(\mathbf{W}; \mathbf{W}) &= \frac{1}{2} \left\| \sqrt{\frac{\mu}{k_1}} \mathbf{w}_1 \right\|^2 + \frac{1}{2} \left\| \sqrt{\frac{k_1}{\mu}} \text{grad}[q_1] \right\|^2 \\ &+ \frac{1}{2} \left\| \sqrt{\frac{\mu}{k_2}} \mathbf{w}_2 \right\|^2 + \frac{1}{2} \left\| \sqrt{\frac{k_2}{\mu}} \text{grad}[q_2] \right\|^2 + \left\| \sqrt{\frac{\beta}{\mu}} (q_1 - q_2) \right\|^2 \\ &+ \left\| \sqrt{\eta_u h_{\Upsilon} \{\mu k_1^{-1}\}} [\mathbf{w}_1] \right\|_{\Gamma^{\text{int}}}^2 + \left\| \sqrt{\frac{\eta_p}{h_{\Upsilon}} \{\mu^{-1} k_1\}} [q_1] \right\|_{\Gamma^{\text{int}}}^2 \\ &+ \left\| \sqrt{\eta_u h_{\Upsilon} \{\mu k_2^{-1}\}} [\mathbf{w}_2] \right\|_{\Gamma^{\text{int}}}^2 + \left\| \sqrt{\frac{\eta_p}{h_{\Upsilon}} \{\mu^{-1} k_2\}} [q_2] \right\|_{\Gamma^{\text{int}}}^2 \quad \forall \mathbf{W} \in \mathbb{U} \end{aligned} \quad (4.4)$$

LEMMA 4.1. (*Stability norm*) $\|\cdot\|_{\text{stab}}^{\text{DG}}$ is a norm on \mathbb{U} .

PROOF. The mathematical proof is similar to that of the continuous formulation, which is provided in [Joodat et al., 2018]. \square

4.1. Convergence theorem and error analysis. In order to perform the error analysis of the proposed stabilized mixed DG formulation, we need to define the finite element solution \mathbf{U}^h and the corresponding weighting function as

$$\mathbf{U}^h = (\mathbf{u}_1^h(\mathbf{x}), \mathbf{u}_2^h(\mathbf{x}), p_1^h(\mathbf{x}), p_2^h(\mathbf{x})) \in \mathbb{U}^h \quad (4.5a)$$

$$\mathbf{W}^h = (\mathbf{w}_1^h(\mathbf{x}), \mathbf{w}_2^h(\mathbf{x}), q_1^h(\mathbf{x}), q_2^h(\mathbf{x})) \in \mathbb{U}^h \quad (4.5b)$$

\mathbb{U}^h is the closed linear subspace of \mathbb{U} and is defined as follows:

$$\mathbb{U}^h = \mathcal{U}^h \times \mathcal{U}^h \times \mathcal{Q}^h \quad (4.6)$$

where

$$\mathcal{U}^h := \left\{ \mathbf{u}^h(\mathbf{x}) \in \mathcal{U} \mid \mathbf{u}^h(\mathbf{x}) \in (C^0(\bar{\omega}^i))^{nd}; \mathbf{u}^h(\mathbf{x})|_{\omega^i} \in (\mathcal{P}^k(\omega^i))^{nd}; i = 1, \dots, Nele \right\} \quad (4.7a)$$

$$\mathcal{Q}^h := \left\{ (p_1^h, p_2^h) \in \mathcal{Q} \mid p_1^h(\mathbf{x}), p_2^h(\mathbf{x}) \in C^0(\bar{\omega}^i); p_1^h(\mathbf{x}), p_2^h(\mathbf{x})|_{\omega^i} \in \mathcal{P}^l(\omega^i); i = 1, \dots, Nele \right\} \quad (4.7b)$$

and $C^0(\bar{\omega}^i)$ is the set of all continuous functions defined on $\bar{\omega}^i$ (which is the set closure of ω^i).

The finite element formulation corresponding to the proposed stabilized mixed DG formulation is defined as follows: Find $\mathbf{U}^h \in \mathbb{U}^h$ such that we have

$$\mathcal{B}_{\text{stab}}^{\text{DG}}(\mathbf{W}^h; \mathbf{U}^h) = \mathcal{L}_{\text{stab}}^{\text{DG}}(\mathbf{W}^h) \quad \forall \mathbf{W}^h \in \mathbb{U}^h \quad (4.8)$$

The error in the finite element solution \mathbf{E} is defined as the difference between the finite element solution and the exact solution. If we define $\tilde{\mathbf{U}}^h$ as an ‘‘interpolate’’ of \mathbf{U} onto \mathbb{U}^h [Brenner and Scott, 1994], decomposition of the error can be performed as follows:

$$\mathbf{E} := \mathbf{U}^h - \mathbf{U} = \mathbf{E}^h + \mathbf{H} \quad (4.9)$$

where $\mathbf{E}^h = \mathbf{U}^h - \tilde{\mathbf{U}}^h$ is the approximation error and $\mathbf{H} = \tilde{\mathbf{U}}^h - \mathbf{U}$ is the interpolation error. The components of \mathbf{E} and \mathbf{H} are as follows:

$$\mathbf{E} = \{\mathbf{e}_{\mathbf{u}_1}, \mathbf{e}_{\mathbf{u}_2}, e_{p_1}, e_{p_2}\} \quad \text{and} \quad \mathbf{H} = \{\boldsymbol{\eta}_{\mathbf{u}_1}, \boldsymbol{\eta}_{\mathbf{u}_2}, \eta_{p_1}, \eta_{p_2}\} \quad (4.10)$$

LEMMA 4.2. (*Estimates for approximation errors on Γ^{int} .*) *On a sequence of admissible meshes, the following estimates hold:*

$$\left\| \sqrt{h_\Upsilon \{\mu k_1^{-1}\}} \{\mathbf{e}_{\mathbf{u}_1}\} \right\|_{\Gamma^{\text{int}}}^2 \leq \mathcal{C}_{\mathbf{e}_{\mathbf{u}_1}} \left\| \sqrt{\mu k_1^{-1}} \mathbf{e}_{\mathbf{u}_1} \right\|^2 \quad (4.11)$$

$$\left\| \sqrt{h_\Upsilon \{\mu k_2^{-1}\}} \{\mathbf{e}_{\mathbf{u}_2}\} \right\|_{\Gamma^{\text{int}}}^2 \leq \mathcal{C}_{\mathbf{e}_{\mathbf{u}_2}} \left\| \sqrt{\mu k_2^{-1}} \mathbf{e}_{\mathbf{u}_2} \right\|^2 \quad (4.12)$$

PROOF. We first note that

$$\left\| \sqrt{h_\Upsilon \{\mu k_1^{-1}\}} \{\mathbf{e}_{\mathbf{u}_1}\} \right\|_{\Gamma^{\text{int}}}^2 = \sum_{\Upsilon \in \mathcal{E}^{\text{int}}} \left\| \sqrt{h_\Upsilon \{\mu k_1^{-1}\}} \{\mathbf{e}_{\mathbf{u}_1}\} \right\|_{\Upsilon}^2 \quad (4.13)$$

We now bound the approximation error of \mathbf{u}_1 on an interior edge $\Upsilon \in \mathcal{E}^{\text{int}}$. The Cauchy-Schwarz inequality implies the following:

$$\left\| \sqrt{h_\Upsilon \{\mu k_1^{-1}\}} \{\mathbf{e}_{\mathbf{u}_1}\} \right\|_{\Upsilon}^2 \leq \frac{1}{2} \left(\left\| \sqrt{h_\Upsilon \{\mu k_1^{-1}\}} \mathbf{e}_{\mathbf{u}_1} \right\|_{\partial\omega_\Upsilon^+ \cap \Upsilon}^2 + \left\| \sqrt{h_\Upsilon \{\mu k_1^{-1}\}} \mathbf{e}_{\mathbf{u}_1} \right\|_{\partial\omega_\Upsilon^- \cap \Upsilon}^2 \right) \quad (4.14)$$

Noting the boundedness of the drag coefficients (i.e., equation (2.4)), we obtain the following:

$$\left\| \sqrt{h_\Upsilon \{\mu k_1^{-1}\}} \{\mathbf{e}_{\mathbf{u}_1}\} \right\|_{\Upsilon}^2 \leq \frac{1}{2} \mathcal{C}_{\text{drag},1} \left(\left\| \sqrt{h_\Upsilon \mu k_1^{-1}} \mathbf{e}_{\mathbf{u}_1} \right\|_{\partial\omega_\Upsilon^+ \cap \Upsilon}^2 + \left\| \sqrt{h_\Upsilon \mu k_1^{-1}} \mathbf{e}_{\mathbf{u}_1} \right\|_{\partial\omega_\Upsilon^- \cap \Upsilon}^2 \right) \quad (4.15)$$

Using the bound based on the locally quasi-uniform condition (i.e., inequality (2.19)) we obtain the following:

$$\left\| \sqrt{h_\Upsilon \{\mu k_1^{-1}\}} \{\mathbf{e}_{\mathbf{u}_1}\} \right\|_{\Upsilon}^2 \leq \frac{1}{4} \mathcal{C}_{\text{drag},1} (1 + \mathcal{C}_{\text{lqu}}) \left(\left\| \sqrt{h_{\omega_\Upsilon^+} \mu k_1^{-1}} \mathbf{e}_{\mathbf{u}_1} \right\|_{\partial\omega_\Upsilon^+ \cap \Upsilon}^2 + \left\| \sqrt{h_{\omega_\Upsilon^-} \mu k_1^{-1}} \mathbf{e}_{\mathbf{u}_1} \right\|_{\partial\omega_\Upsilon^- \cap \Upsilon}^2 \right) \quad (4.16)$$

By summing over all the interior edges we obtain the following:

$$\begin{aligned} \sum_{\Upsilon \in \mathcal{E}^{\text{int}}} \left\| \sqrt{h_\Upsilon \{\mu k_1^{-1}\}} \{\mathbf{e}_{\mathbf{u}_1}\} \right\|_{\Upsilon}^2 &\leq \frac{1}{4} \mathcal{C}_{\text{drag},1} (1 + \mathcal{C}_{\text{lqu}}) \sum_{\omega \in \mathcal{T}} \left\| \sqrt{h_\omega \mu k_1^{-1}} \mathbf{e}_{\mathbf{u}_1} \right\|_{\partial\omega \setminus \partial\Omega}^2 \\ &\leq \frac{1}{4} \mathcal{C}_{\text{drag},1} (1 + \mathcal{C}_{\text{lqu}}) \sum_{\omega \in \mathcal{T}} \left\| \sqrt{h_\omega \mu k_1^{-1}} \mathbf{e}_{\mathbf{u}_1} \right\|_{\partial\omega}^2 \end{aligned} \quad (4.17)$$

By invoking the discrete trace inequality (2.33) we obtain the following:

$$\begin{aligned} \sum_{\Upsilon \in \mathcal{E}^{\text{int}}} \left\| \sqrt{h_\Upsilon \{\mu k_1^{-1}\}} \{\mathbf{e}_{\mathbf{u}_1}\} \right\|_{\Upsilon}^2 &\leq \frac{1}{4} \mathcal{C}_{\text{drag},1} (1 + \mathcal{C}_{\text{lqu}}) \mathcal{C}_{\text{trace}}^2 (1 + \mathcal{C}_{\text{inv}})^2 \sum_{\omega \in \mathcal{T}} \left\| \sqrt{\mu k_1^{-1}} \mathbf{e}_{\mathbf{u}_1} \right\|_{\omega}^2 \\ &\leq \frac{1}{4} \mathcal{C}_{\text{drag},1} \mathcal{C}_{\text{trace}}^2 (1 + \mathcal{C}_{\text{inv}})^2 (1 + \mathcal{C}_{\text{lqu}}) \left\| \sqrt{\mu k_1^{-1}} \mathbf{e}_{\mathbf{u}_1} \right\|_{\omega}^2 \end{aligned} \quad (4.18)$$

(Recall that the subscript will be dropped if the L_2 norm is over $\tilde{\Omega} := \cup_{\omega \in \mathcal{T}} \omega$.) Thus,

$$\mathcal{C}_{\mathbf{e}_{\mathbf{u}_1}} := \frac{1}{4} \mathcal{C}_{\text{drag},1} \mathcal{C}_{\text{trace}}^2 (1 + \mathcal{C}_{\text{inv}})^2 (1 + \mathcal{C}_{\text{lqu}}) \quad (4.19)$$

On similar lines, one can establish the estimate (4.12) with

$$\mathcal{C}_{\mathbf{e}_{\mathbf{u}_2}} := \frac{1}{4} \mathcal{C}_{\text{drag},2} \mathcal{C}_{\text{trace}}^2 (1 + \mathcal{C}_{\text{inv}})^2 (1 + \mathcal{C}_{\text{liqu}}) \quad (4.20)$$

□

If a p -th order polynomial is employed for a field variable $f(\mathbf{x})$ on an element $\omega \in \mathcal{T}$ and the corresponding interpolate denoted by \tilde{f}^h , the following estimate holds for the interpolation error [Brezzi and Fortin, 1991]:

$$\|f - \tilde{f}^h\|_{\omega} \leq \mathcal{C}_{\text{int}} h_{\omega}^{p+1} |f|_{H^{p+1}(\omega)} \quad (4.21)$$

where h_{ω} is the element diameter of ω , \mathcal{C}_{int} is a non-dimensional constant independent of h_{ω} and f , and $|\cdot|_{H^{p+1}(\omega)}$ is a Sobolev semi-norm, which is defined in equation (2.26).

To avoid further introduction of constants, we employ the notation $A \lesssim B$ to denote that there exists a constant \mathcal{C} , independent of the mesh size, such that $A \leq \mathcal{C}B$. A similar definition holds for $A \gtrsim B$. The notation $A \sim B$ denotes the case when $A \lesssim B$ and $A \gtrsim B$ hold simultaneously.

LEMMA 4.3. (*Estimates for interpolation errors on Γ^{int} .*) *If polynomial orders used for interpolation of \mathbf{u}_1 , \mathbf{u}_2 , p_1 and p_2 are, respectively, p , q , r and s then the following estimates hold for the interpolation errors on Γ^{int} :*

$$\left\| \sqrt{\frac{h_{\Upsilon}}{\eta_p} \{\{\mu k_1^{-1}\}\}} \{\{\boldsymbol{\eta}_{\mathbf{u}_1}\}\} \right\|_{\Gamma^{\text{int}}}^2 \lesssim \sum_{\omega \in \mathcal{T}_h} h_{\omega}^{2(p+1)} |\mathbf{u}_1|_{H^{p+1}(\omega)}^2 \quad (4.22)$$

$$\left\| \sqrt{\frac{h_{\Upsilon}}{\eta_p} \{\{\mu k_2^{-1}\}\}} \{\{\boldsymbol{\eta}_{\mathbf{u}_2}\}\} \right\|_{\Gamma^{\text{int}}}^2 \lesssim \sum_{\omega \in \mathcal{T}_h} h_{\omega}^{2(q+1)} |\mathbf{u}_2|_{H^{q+1}(\omega)}^2 \quad (4.23)$$

$$\left\| \sqrt{h_{\Upsilon}^{-1} \{\{\mu^{-1} k_1\}\}} \llbracket \eta_{p_1} \rrbracket \right\|_{\Gamma^{\text{int}}}^2 \lesssim \sum_{\omega \in \mathcal{T}_h} h_{\omega}^{2r} |p_1|_{H^{r+1}(\omega)}^2 \quad (4.24)$$

$$\left\| \sqrt{h_{\Upsilon}^{-1} \{\{\mu^{-1} k_2\}\}} \llbracket \eta_{p_2} \rrbracket \right\|_{\Gamma^{\text{int}}}^2 \lesssim \sum_{\omega \in \mathcal{T}_h} h_{\omega}^{2s} |p_2|_{H^{s+1}(\omega)}^2 \quad (4.25)$$

PROOF. We first establish the estimate (4.22). The boundedness of the drag coefficient $\mu/k_1(\mathbf{x})$ and the linearity of a norm imply the following:

$$\left\| \sqrt{\frac{h_{\Upsilon}}{\eta_p} \{\{\mu k_1^{-1}\}\}} \{\{\boldsymbol{\eta}_{\mathbf{u}_1}\}\} \right\|_{\Upsilon}^2 \leq \frac{1}{\eta_p} \left(\sup_{\mathbf{x} \in \Omega} \frac{\mu}{k_1(\mathbf{x})} \right) \left\| \sqrt{h_{\Upsilon}} \{\{\boldsymbol{\eta}_{\mathbf{u}_1}\}\} \right\|_{\Upsilon}^2 \quad \forall \Upsilon \in \mathcal{E}^{\text{int}} \quad (4.26)$$

Using the triangle inequality and the bound from the locally quasi-uniform condition (2.19), we obtain the following:

$$\left\| \sqrt{\frac{h_{\Upsilon}}{\eta_p} \{\{\mu k_1^{-1}\}\}} \{\{\boldsymbol{\eta}_{\mathbf{u}_1}\}\} \right\|_{\Upsilon}^2 \lesssim \frac{1}{4} (1 + \mathcal{C}_{\text{liqu}}) \left(\left\| \sqrt{h_{\omega_{\Upsilon}^+}} \boldsymbol{\eta}_{\mathbf{u}_1} \right\|_{\partial\omega_{\Upsilon}^+ \cap \Upsilon}^2 + \left\| \sqrt{h_{\omega_{\Upsilon}^-}} \boldsymbol{\eta}_{\mathbf{u}_1} \right\|_{\partial\omega_{\Upsilon}^- \cap \Upsilon}^2 \right) \quad \forall \Upsilon \in \mathcal{E}^{\text{int}} \quad (4.27)$$

By summing over all the interior edges and noting the linearity of a norm, we obtain the following:

$$\left\| \sqrt{\frac{h_{\Upsilon}}{\eta_p} \{\{\mu k_1^{-1}\}\}} \{\{\boldsymbol{\eta}_{\mathbf{u}_1}\}\} \right\|_{\Gamma^{\text{int}}}^2 = \sum_{\Upsilon \in \mathcal{E}^{\text{int}}} \left\| \sqrt{\frac{h_{\Upsilon}}{\eta_p} \{\{\mu k_1^{-1}\}\}} \{\{\boldsymbol{\eta}_{\mathbf{u}_1}\}\} \right\|_{\Upsilon}^2 \lesssim \sum_{\omega \in \mathcal{T}_h} (h_{\omega} \|\boldsymbol{\eta}_{\mathbf{u}_1}\|_{\partial\omega}^2) \quad (4.28)$$

By invoking the discrete trace inequality (2.33), we obtain the following inequality:

$$\left\| \sqrt{\frac{h_\Upsilon}{\eta_p}} \{\mu k_1^{-1}\} \{\boldsymbol{\eta}_{\mathbf{u}_1}\} \right\|_{\Gamma^{\text{int}}}^2 \lesssim \sum_{\omega \in \mathcal{T}_h} \|\boldsymbol{\eta}_{\mathbf{u}_1}\|_\omega^2 \quad (4.29)$$

If a polynomial of order p is employed for approximating \mathbf{u}_1 , then the standard estimate for the interpolation error (4.21) provides the following:

$$\left\| \sqrt{\frac{h_\Upsilon}{\eta_p}} \{\mu k_1^{-1}\} \{\boldsymbol{\eta}_{\mathbf{u}_1}\} \right\|_{\Gamma^{\text{int}}}^2 \lesssim \sum_{\omega \in \mathcal{T}_h} h_\omega^{2(p+1)} |\mathbf{u}_1|_{H^{p+1}(\omega)}^2 \quad (4.30)$$

which is the estimate (4.22). By reasoning out on similar lines, one can establish the estimate (4.23).

We now establish the estimate (4.24). The boundedness of the drag coefficient $\mu/k_1(\mathbf{x})$ and the linearity of a norm imply the following:

$$\left\| \sqrt{h_\Upsilon^{-1} \{\mu^{-1} k_1\}} \llbracket \eta_{p_1} \rrbracket \right\|_\Upsilon^2 \leq \left(\inf_{\mathbf{x} \in \Omega} \frac{\mu}{k_1(\mathbf{x})} \right) \left\| \sqrt{h_\Upsilon^{-1}} \llbracket \eta_{p_1} \rrbracket \right\|_\Upsilon^2 \quad \forall \Upsilon \in \mathcal{E}^{\text{int}} \quad (4.31)$$

Using the triangle inequality and the bound from the locally quasi-uniform condition (2.19), we obtain the following:

$$\left\| \sqrt{h_\Upsilon^{-1} \{\mu^{-1} k_1\}} \llbracket \eta_{p_1} \rrbracket \right\|_\Upsilon^2 \lesssim 4 \left(1 + \frac{1}{\mathcal{C}_{\text{qu}}} \right)^{-1} \left(\left\| \sqrt{h_{\omega_\Upsilon^+}^{-1}} \eta_{p_1} \right\|_{\partial\omega_\Upsilon^+ \cap \Upsilon}^2 + \left\| \sqrt{h_{\omega_\Upsilon^-}^{-1}} \eta_{p_1} \right\|_{\partial\omega_\Upsilon^- \cap \Upsilon}^2 \right) \quad \forall \Upsilon \in \mathcal{E}^{\text{int}} \quad (4.32)$$

By summing over all the interior edges and noting the linearity of a norm, we obtain the following:

$$\left\| \sqrt{h_\Upsilon^{-1} \{\mu^{-1} k_1\}} \llbracket \eta_{p_1} \rrbracket \right\|_{\Gamma^{\text{int}}}^2 = \sum_{\Upsilon \in \mathcal{E}^{\text{int}}} \left\| \sqrt{h_\Upsilon^{-1} \{\mu^{-1} k_1\}} \llbracket \eta_{p_1} \rrbracket \right\|_\Upsilon^2 \lesssim \sum_{\omega \in \mathcal{T}_h} \left(h_\omega^{-1} \|\eta_{p_1}\|_{\partial\omega}^2 \right) \quad (4.33)$$

By invoking the discrete trace inequality (2.32), we obtain the following inequality:

$$\left\| \sqrt{h_\Upsilon^{-1} \{\mu^{-1} k_1\}} \llbracket \eta_{p_1} \rrbracket \right\|_{\Gamma^{\text{int}}}^2 \lesssim \sum_{\omega \in \mathcal{T}_h} \left(h_\omega^{-2} \|\eta_{p_1}\|_\omega^2 \right) \quad (4.34)$$

If a polynomial of order r is employed for approximating p_1 , then the standard estimate for the interpolation error (4.21) provides the following:

$$\left\| \sqrt{h_\Upsilon^{-1} \{\mu^{-1} k_1\}} \llbracket \eta_{p_1} \rrbracket \right\|_{\Gamma^{\text{int}}}^2 \lesssim \sum_{\omega \in \mathcal{T}_h} h_\omega^{2r} |p_1|_{H^{r+1}(\omega)}^2 \quad (4.35)$$

which is the estimate (4.24). By reasoning out on similar lines, one can establish the estimate (4.25). \square

LEMMA 4.4. (*Estimate for \mathbf{H} under the stability norm.*) *If polynomial orders used for interpolation of \mathbf{u}_1 , \mathbf{u}_2 , p_1 and p_2 are, respectively, p , q , r and s then the following estimate holds:*

$$\left(\|\mathbf{H}\|_{\text{stab}}^{\text{DG}} \right)^2 \lesssim \sum_{\omega \in \mathcal{T}_h} \left(h_\omega^{2(p+1)} |\mathbf{u}_1|_{H^{p+1}(\omega)}^2 + h_\omega^{2(q+1)} |\mathbf{u}_2|_{H^{q+1}(\omega)}^2 + (1 + h_\omega^2) h_\omega^{2r} |p_1|_{H^{r+1}(\omega)}^2 + (1 + h_\omega^2) h_\omega^{2s} |p_2|_{H^{s+1}(\omega)}^2 \right) \quad (4.36)$$

where the constant in the estimate is independent of the characteristic mesh length (h or h_ω) and the solution fields (\mathbf{u}_1 , \mathbf{u}_2 , p_1 and p_2).

PROOF. The definition of the stability norm (4.4) and the components of \mathbf{H} (4.10) imply the following:

$$\begin{aligned}
(\|\mathbf{H}\|_{\text{stab}}^{\text{DG}})^2 &= \frac{1}{2} \left\| \sqrt{\frac{\mu}{k_1}} \boldsymbol{\eta}_{\mathbf{u}_1} \right\|^2 + \frac{1}{2} \left\| \sqrt{\frac{k_1}{\mu}} \text{grad}[\eta_{p_1}] \right\|^2 + \frac{1}{2} \left\| \sqrt{\frac{\mu}{k_2}} \boldsymbol{\eta}_{\mathbf{u}_2} \right\|^2 + \frac{1}{2} \left\| \sqrt{\frac{k_2}{\mu}} \text{grad}[\eta_{p_2}] \right\|^2 \\
&+ \left\| \sqrt{\frac{\beta}{\mu}} (\eta_{p_1} - \eta_{p_2}) \right\|^2 + \left\| \sqrt{\eta_u h_\Upsilon \{\mu k_1^{-1}\}} \llbracket \boldsymbol{\eta}_{\mathbf{u}_1} \rrbracket \right\|_{\Gamma^{\text{int}}}^2 + \left\| \sqrt{\frac{\eta_p}{h_\Upsilon} \{\mu^{-1} k_1\}} \llbracket \eta_{p_1} \rrbracket \right\|_{\Gamma^{\text{int}}}^2 \\
&+ \left\| \sqrt{\eta_u h_\Upsilon \{\mu k_2^{-1}\}} \llbracket \boldsymbol{\eta}_{\mathbf{u}_2} \rrbracket \right\|_{\Gamma^{\text{int}}}^2 + \left\| \sqrt{\frac{\eta_p}{h_\Upsilon} \{\mu^{-1} k_2\}} \llbracket \eta_{p_2} \rrbracket \right\|_{\Gamma^{\text{int}}}^2
\end{aligned} \tag{4.37}$$

Using the boundedness of the drag coefficient of the first pore-network, linearity of a norm and the standard estimate for the interpolation error (4.21), and noting that the polynomial order of approximation for \mathbf{u}_1 is p , we obtain the following:

$$\frac{1}{2} \left\| \sqrt{\frac{\mu}{k_1}} \boldsymbol{\eta}_{\mathbf{u}_1} \right\|^2 \leq \frac{1}{2} \sup_{\mathbf{x} \in \Omega} \frac{\mu}{k_1(\mathbf{x})} \sum_{\omega \in \mathcal{T}_h} \|\boldsymbol{\eta}_{\mathbf{u}_1}\|_{\omega}^2 \lesssim \sum_{\omega \in \mathcal{T}_h} h_{\omega}^{2(p+1)} |\mathbf{u}_1|_{H^{p+1}(\omega)}^2 \tag{4.38}$$

Similarly,

$$\frac{1}{2} \left\| \sqrt{\frac{\mu}{k_2}} \boldsymbol{\eta}_{\mathbf{u}_2} \right\|^2 \leq \frac{1}{2} \sup_{\mathbf{x} \in \Omega} \frac{\mu}{k_2(\mathbf{x})} \sum_{\omega \in \mathcal{T}_h} \|\boldsymbol{\eta}_{\mathbf{u}_2}\|_{\omega}^2 \lesssim \sum_{\omega \in \mathcal{T}_h} h_{\omega}^{2(q+1)} |\mathbf{u}_2|_{H^{q+1}(\omega)}^2 \tag{4.39}$$

For the *second* term, we proceed as follows by first noting the boundedness of the drag coefficient in the first pore-network:

$$\begin{aligned}
\frac{1}{2} \left\| \sqrt{\frac{k_1}{\mu}} \text{grad}[\eta_{p_1}] \right\|^2 &\leq \frac{1}{2} \inf_{\mathbf{x} \in \Omega} \frac{\mu}{k_1(\mathbf{x})} \sum_{\omega \in \mathcal{T}_h} \|\text{grad}[\eta_{p_1}]\|_{\omega}^2 \\
&\leq \frac{1}{2} \inf_{\mathbf{x} \in \Omega} \frac{\mu}{k_1(\mathbf{x})} C_{\text{inv}}^2 \sum_{\omega \in \mathcal{T}_h} h_{\omega}^{-2} \|\eta_{p_1}\|_{\omega}^2 \quad [\text{inverse estimate (2.30)}] \\
&\lesssim \sum_{\omega \in \mathcal{T}_h} h_{\omega}^{2r} |p_1|_{H^{r+1}(\omega)}^2 \quad [\text{interpolation estimate (4.21)}]
\end{aligned} \tag{4.40}$$

Similarly, one can derive the following estimate for the *fourth* term:

$$\frac{1}{2} \left\| \sqrt{\frac{k_2}{\mu}} \text{grad}[\eta_{p_2}] \right\|^2 \lesssim \sum_{\omega \in \mathcal{T}_h} h_{\omega}^{2s} |p_2|_{H^{s+1}(\omega)}^2 \tag{4.41}$$

The estimate for the *fifth* term utilizes the triangle inequality and the interpolation estimate (4.21) and it can be obtained as follows:

$$\left\| \sqrt{\frac{\beta}{\mu}} (\eta_{p_1} - \eta_{p_2}) \right\|^2 \leq \frac{\beta}{\mu} \sum_{\omega \in \mathcal{T}_h} (\|\eta_{p_1}\|_{\omega}^2 + \|\eta_{p_2}\|_{\omega}^2) \lesssim \sum_{\omega \in \mathcal{T}_h} (h_{\omega}^{2(r+1)} |p_1|_{H^{r+1}(\omega)}^2 + h_{\omega}^{2(s+1)} |p_2|_{H^{s+1}(\omega)}^2) \tag{4.42}$$

Using the boundedness of η_u and the drag coefficient of the first pore-network and noting the linearity of a norm, we obtain the following estimate for the *sixth* term:

$$\left\| \sqrt{\eta_u h_\Upsilon \{\mu k_1^{-1}\}} \llbracket \boldsymbol{\eta}_{\mathbf{u}_1} \rrbracket \right\|_{\Gamma^{\text{int}}}^2 \lesssim \sum_{\Upsilon \in \mathcal{E}^{\text{int}}} \left\| \sqrt{h_\Upsilon} \llbracket \boldsymbol{\eta}_{\mathbf{u}_1} \rrbracket \right\|_{\Upsilon}^2 \tag{4.43}$$

Using the bound based on the locally quasi-uniform condition (2.19) and the triangle inequality, we obtain the following:

$$\begin{aligned} \left\| \sqrt{\eta_u h_\Upsilon \{\mu k_1^{-1}\}} \llbracket \boldsymbol{\eta}_{\mathbf{u}_1} \rrbracket \right\|_{\Gamma^{\text{int}}}^2 &\lesssim \sum_{\Upsilon \in \mathcal{E}^{\text{int}}} \left(\left\| \sqrt{h_{\omega_\Upsilon^+}} \boldsymbol{\eta}_{\mathbf{u}_1} \right\|_{\partial\omega_\Upsilon^+ \cap \Upsilon}^2 + \left\| \sqrt{h_{\omega_\Upsilon^-}} \boldsymbol{\eta}_{\mathbf{u}_1} \right\|_{\partial\omega_\Upsilon^- \cap \Upsilon}^2 \right) \\ &\lesssim \sum_{\omega \in \mathcal{T}_h} h_\omega \|\boldsymbol{\eta}_{\mathbf{u}_1}\|_{\partial\omega}^2 \end{aligned} \quad (4.44)$$

Using the discrete trace inequality (2.33) and the standard interpolation estimate (4.21), we obtain the following:

$$\left\| \sqrt{\eta_u h_\Upsilon \{\mu k_1^{-1}\}} \llbracket \boldsymbol{\eta}_{\mathbf{u}_1} \rrbracket \right\|_{\Gamma^{\text{int}}}^2 \lesssim \sum_{\omega \in \mathcal{T}_h} \|\boldsymbol{\eta}_{\mathbf{u}_1}\|_{\omega}^2 \lesssim \sum_{\omega \in \mathcal{T}_h} h_\omega^{2(p+1)} |\mathbf{u}_1|_{H^{p+1}(\omega)}^2 \quad (4.45)$$

A similar argument gives rise to the following estimate for the *eighth* term:

$$\left\| \sqrt{\eta_u h_\Upsilon \{\mu k_2^{-1}\}} \llbracket \boldsymbol{\eta}_{\mathbf{u}_2} \rrbracket \right\|_{\Gamma^{\text{int}}}^2 \lesssim \sum_{\omega \in \mathcal{T}_h} h_\omega^{2(q+1)} |\mathbf{u}_2|_{H^{q+1}(\omega)}^2 \quad (4.46)$$

Noting that η_p is a bounded constant, estimates (4.24) and (4.25) immediately imply the following estimates for the *seventh* and *ninth* terms:

$$\left\| \sqrt{\frac{\eta_p}{h_\Upsilon} \{\mu^{-1} k_1\}} \llbracket \eta_{p_1} \rrbracket \right\|_{\Gamma^{\text{int}}}^2 \lesssim \sum_{\omega \in \mathcal{T}_h} h_\omega^{2r} |p_1|_{H^{r+1}(\omega)}^2 \quad (4.47)$$

$$\left\| \sqrt{\frac{\eta_p}{h_\Upsilon} \{\mu^{-1} k_2\}} \llbracket \eta_{p_2} \rrbracket \right\|_{\Gamma^{\text{int}}}^2 \lesssim \sum_{\omega \in \mathcal{T}_h} h_\omega^{2s} |p_2|_{H^{s+1}(\omega)}^2 \quad (4.48)$$

By adding up the individual estimates for all the terms, we obtain the desired result. \square

THEOREM 4.5. (*Consistency*) *The error in the finite element solution satisfies*

$$\mathcal{B}_{\text{stab}}^{\text{DG}}(\mathbf{W}^h; \mathbf{E}) = 0 \quad \forall \mathbf{W}^h \in \mathbb{U}^h \subset \mathbb{U} \quad (4.49)$$

PROOF. The proof follows a standard procedure employed in the literature. Equation (4.3) implies that for all $\mathbf{W}^h \in \mathbb{U}^h \subset \mathbb{U}$ we have the following:

$$\mathcal{B}_{\text{stab}}^{\text{DG}}(\mathbf{W}^h; \mathbb{U}^h) = \mathcal{L}_{\text{stab}}^{\text{DG}}(\mathbf{W}^h) \quad (4.50a)$$

$$\mathcal{B}_{\text{stab}}^{\text{DG}}(\mathbf{W}^h; \mathbb{U}) = \mathcal{L}_{\text{stab}}^{\text{DG}}(\mathbf{W}^h) \quad (4.50b)$$

By subtracting the above two equations, invoking the linearity in the second slot of $\mathcal{B}_{\text{stab}}^{\text{DG}}(\cdot; \cdot)$ and noting the definition of \mathbf{E} given by (4.9), we obtain the desired result. \square

THEOREM 4.6. (*Convergence*) *Under a sequence of admissible meshes, the finite element solution $\mathbf{U}^h \in \mathbb{U}^h$ tends to the exact solution $\mathbf{U} \in \mathbb{U}$ almost everywhere⁵ as the mesh-size $h \rightarrow 0$.*

PROOF. The error with respect to the stability norm can be rewritten as follows:

$$(\|\mathbf{E}\|_{\text{stab}}^{\text{DG}})^2 = \mathcal{B}_{\text{stab}}^{\text{DG}}(\mathbf{E}; \mathbf{E}) = \mathcal{B}_{\text{stab}}^{\text{DG}}(\mathbf{E}^h + \mathbf{H}; \mathbf{E}) = \mathcal{B}_{\text{stab}}^{\text{DG}}(\mathbf{E}^h; \mathbf{E}) + \mathcal{B}_{\text{stab}}^{\text{DG}}(\mathbf{H}; \mathbf{E}) = \mathcal{B}_{\text{stab}}^{\text{DG}}(\mathbf{H}; \mathbf{E}) \quad (4.51)$$

We invoked the definition of $\|\cdot\|_{\text{stab}}^{\text{DG}}$ norm (i.e., Eq. (4.4)) for establishing the first equality, the decomposition of the error (i.e., Eq. (4.9)) for the second equality, linearity in the first slot of

⁵Two quantities that are the same except on a set of measure zero are said to be equal almost everywhere [Evans, 1998].

$\mathcal{B}_{\text{stab}}^{\text{DG}}(\cdot; \cdot)$ for the third equality, and consistency (i.e., Theorem 4.5) for the fourth equality. We now expand $\mathcal{B}_{\text{stab}}^{\text{DG}}(\mathbf{H}; \mathbf{E})$ as follows:

$$\begin{aligned}
\mathcal{B}_{\text{stab}}^{\text{DG}}(\mathbf{H}; \mathbf{E}) &= \mathcal{B}_{\text{stab}}^{\text{DG}}(\boldsymbol{\eta}_{\mathbf{u}_1}, \boldsymbol{\eta}_{\mathbf{u}_2}, \eta_{p_1}, \eta_{p_2}; \mathbf{e}_{\mathbf{u}_1}, \mathbf{e}_{\mathbf{u}_2}, e_{p_1}, e_{p_2}) \\
&= \frac{1}{2}(\boldsymbol{\eta}_{\mathbf{u}_1}; \mu k_1^{-1} \mathbf{e}_{\mathbf{u}_1}) + \frac{1}{2}(\boldsymbol{\eta}_{\mathbf{u}_1}; \text{grad}[e_{p_1}]) - \frac{1}{2}(\text{grad}[\eta_{p_1}]; \mathbf{e}_{\mathbf{u}_1}) + \frac{1}{2} \left(\text{grad}[\eta_{p_1}]; \frac{k_1}{\mu} \text{grad}[e_{p_1}] \right) \\
&+ \frac{1}{2}(\boldsymbol{\eta}_{\mathbf{u}_2}; \mu k_2^{-1} \mathbf{e}_{\mathbf{u}_2}) + \frac{1}{2}(\boldsymbol{\eta}_{\mathbf{u}_2}; \text{grad}[e_{p_2}]) - \frac{1}{2}(\text{grad}[\eta_{p_2}]; \mathbf{e}_{\mathbf{u}_2}) + \frac{1}{2} \left(\text{grad}[\eta_{p_2}]; \frac{k_2}{\mu} \text{grad}[e_{p_2}] \right) \\
&+ \left((\eta_{p_1} - \eta_{p_2}); \frac{\beta}{\mu} (e_{p_1} - e_{p_2}) \right) \\
&- (\{\{\boldsymbol{\eta}_{\mathbf{u}_1}\}\}; [e_{p_1}])_{\Gamma^{\text{int}}} + ([\eta_{p_1}]; \{\{\mathbf{e}_{\mathbf{u}_1}\}\})_{\Gamma^{\text{int}}} - (\{\{\boldsymbol{\eta}_{\mathbf{u}_2}\}\}; [e_{p_2}])_{\Gamma^{\text{int}}} + ([\eta_{p_2}]; \{\{\mathbf{e}_{\mathbf{u}_2}\}\})_{\Gamma^{\text{int}}} \\
&+ (\eta_u h_{\Upsilon} \{\{\mu k_1^{-1}\}\} [\boldsymbol{\eta}_{\mathbf{u}_1}]; [\mathbf{e}_{\mathbf{u}_1}])_{\Gamma^{\text{int}}} + \left(\frac{\eta_p}{h_{\Upsilon}} \{\{\mu^{-1} k_1\}\} [\eta_{p_1}]; [e_{p_1}] \right)_{\Gamma^{\text{int}}} \\
&+ (\eta_u h_{\Upsilon} \{\{\mu k_2^{-1}\}\} [\boldsymbol{\eta}_{\mathbf{u}_2}]; [\mathbf{e}_{\mathbf{u}_2}])_{\Gamma^{\text{int}}} + \left(\frac{\eta_p}{h_{\Upsilon}} \{\{\mu^{-1} k_2\}\} [\eta_{p_2}]; [e_{p_2}] \right)_{\Gamma^{\text{int}}} \tag{4.52}
\end{aligned}$$

By employing Cauchy-Schwarz and Peter-Paul inequalities, we obtain the following bound⁶:

$$\begin{aligned}
2\mathcal{B}_{\text{stab}}^{\text{DG}}(\mathbf{H}; \mathbf{E}) &\leq \frac{\varepsilon_1}{2} \left\| \sqrt{\frac{\mu}{k_1}} \boldsymbol{\eta}_{\mathbf{u}_1} \right\|^2 + \frac{1}{2\varepsilon_1} \left\| \sqrt{\frac{\mu}{k_1}} \mathbf{e}_{\mathbf{u}_1} \right\|^2 + \frac{\varepsilon_2}{2} \left\| \sqrt{\frac{\mu}{k_1}} \boldsymbol{\eta}_{\mathbf{u}_1} \right\|^2 + \frac{1}{2\varepsilon_2} \left\| \sqrt{\frac{k_1}{\mu}} \text{grad}[e_{p_1}] \right\|^2 \\
&+ \frac{\varepsilon_3}{2} \left\| \sqrt{\frac{k_1}{\mu}} \text{grad}[\eta_{p_1}] \right\|^2 + \frac{1}{2\varepsilon_3} \left\| \sqrt{\frac{\mu}{k_1}} \mathbf{e}_{\mathbf{u}_1} \right\|^2 + \frac{\varepsilon_4}{2} \left\| \sqrt{\frac{k_1}{\mu}} \text{grad}[\eta_{p_1}] \right\|^2 + \frac{1}{2\varepsilon_4} \left\| \sqrt{\frac{k_1}{\mu}} \text{grad}[e_{p_1}] \right\|^2 \\
&+ \frac{\varepsilon_5}{2} \left\| \sqrt{\frac{\mu}{k_2}} \boldsymbol{\eta}_{\mathbf{u}_2} \right\|^2 + \frac{1}{2\varepsilon_5} \left\| \sqrt{\frac{\mu}{k_2}} \mathbf{e}_{\mathbf{u}_2} \right\|^2 + \frac{\varepsilon_6}{2} \left\| \sqrt{\frac{\mu}{k_2}} \boldsymbol{\eta}_{\mathbf{u}_2} \right\|^2 + \frac{1}{2\varepsilon_6} \left\| \sqrt{\frac{k_2}{\mu}} \text{grad}[e_{p_2}] \right\|^2 \\
&+ \frac{\varepsilon_7}{2} \left\| \sqrt{\frac{k_2}{\mu}} \text{grad}[\eta_{p_2}] \right\|^2 + \frac{1}{2\varepsilon_7} \left\| \sqrt{\frac{\mu}{k_2}} \mathbf{e}_{\mathbf{u}_2} \right\|^2 + \frac{\varepsilon_8}{2} \left\| \sqrt{\frac{k_2}{\mu}} \text{grad}[\eta_{p_2}] \right\|^2 + \frac{1}{2\varepsilon_8} \left\| \sqrt{\frac{k_2}{\mu}} \text{grad}[e_{p_2}] \right\|^2 \\
&+ \varepsilon_9 \left\| \sqrt{\frac{\beta}{\mu}} (\eta_{p_1} - \eta_{p_2}) \right\|^2 + \frac{1}{\varepsilon_9} \left\| \sqrt{\frac{\beta}{\mu}} (e_{p_1} - e_{p_2}) \right\|^2 \\
&+ \varepsilon_{10} \left\| \sqrt{\frac{h_{\Upsilon}}{\eta_p}} \{\{\mu k_1^{-1}\}\} \{\{\boldsymbol{\eta}_{\mathbf{u}_1}\}\} \right\|_{\Gamma^{\text{int}}}^2 + \frac{1}{\varepsilon_{10}} \left\| \sqrt{\frac{\eta_p}{h_{\Upsilon}}} \{\{\mu^{-1} k_1\}\} [e_{p_1}] \right\|_{\Gamma^{\text{int}}}^2 \\
&+ \varepsilon_{11} \left\| \sqrt{\frac{h_{\Upsilon}^{-1}}{\eta_p}} \{\{\mu^{-1} k_1\}\} [\eta_{p_1}] \right\|_{\Gamma^{\text{int}}}^2 + \frac{1}{\varepsilon_{11}} \left\| \sqrt{h_{\Upsilon}} \{\{\mu k_1^{-1}\}\} \{\{\mathbf{e}_{\mathbf{u}_1}\}\} \right\|_{\Gamma^{\text{int}}}^2 \\
&+ \varepsilon_{12} \left\| \sqrt{\frac{h_{\Upsilon}}{\eta_p}} \{\{\mu k_2^{-1}\}\} \{\{\boldsymbol{\eta}_{\mathbf{u}_2}\}\} \right\|_{\Gamma^{\text{int}}}^2 + \frac{1}{\varepsilon_{12}} \left\| \sqrt{\frac{\eta_p}{h_{\Upsilon}}} \{\{\mu^{-1} k_2\}\} [e_{p_2}] \right\|_{\Gamma^{\text{int}}}^2 \\
&+ \varepsilon_{13} \left\| \sqrt{\frac{h_{\Upsilon}^{-1}}{\eta_p}} \{\{\mu^{-1} k_2\}\} [\eta_{p_2}] \right\|_{\Gamma^{\text{int}}}^2 + \frac{1}{\varepsilon_{13}} \left\| \sqrt{h_{\Upsilon}} \{\{\mu k_2^{-1}\}\} \{\{\mathbf{e}_{\mathbf{u}_2}\}\} \right\|_{\Gamma^{\text{int}}}^2 \\
&+ \varepsilon_{14} \left\| \sqrt{\eta_u h_{\Upsilon}} \{\{\mu k_1^{-1}\}\} [\boldsymbol{\eta}_{\mathbf{u}_1}] \right\|_{\Gamma^{\text{int}}}^2 + \frac{1}{\varepsilon_{14}} \left\| \sqrt{\eta_u h_{\Upsilon}} \{\{\mu k_1^{-1}\}\} [\mathbf{e}_{\mathbf{u}_1}] \right\|_{\Gamma^{\text{int}}}^2 \\
&+ \varepsilon_{15} \left\| \sqrt{\frac{\eta_p}{h_{\Upsilon}}} \{\{\mu^{-1} k_1\}\} [\eta_{p_1}] \right\|_{\Gamma^{\text{int}}}^2 + \frac{1}{\varepsilon_{15}} \left\| \sqrt{\frac{\eta_p}{h_{\Upsilon}}} \{\{\mu^{-1} k_1\}\} [e_{p_1}] \right\|_{\Gamma^{\text{int}}}^2
\end{aligned}$$

⁶For convenience of the reader, we color-coded the terms. (See the online version for the colored text.) The red-colored terms contain interpolation errors and contribute to $\|\mathbf{H}\|_{\text{stab}}^{\text{DG}}$. The blue-colored terms contain approximation errors and contribute to $\|\mathbf{E}\|_{\text{stab}}^{\text{DG}}$. We employ Lemma 4.2 on the magenta-colored terms and employ Lemma 4.3 on the green-colored terms.

$$\begin{aligned}
& +\varepsilon_{16} \left\| \sqrt{\eta_u h_\Upsilon \{\mu k_2^{-1}\}} \llbracket \boldsymbol{\eta}_{\mathbf{u}_2} \rrbracket \right\|_{\Gamma^{\text{int}}}^2 + \frac{1}{\varepsilon_{16}} \left\| \sqrt{\eta_u h_\Upsilon \{\mu k_2^{-1}\}} \llbracket \mathbf{e}_{\mathbf{u}_2} \rrbracket \right\|_{\Gamma^{\text{int}}}^2 \\
& +\varepsilon_{17} \left\| \sqrt{\frac{\eta_p}{h_\Upsilon} \{\mu^{-1} k_2\}} \llbracket \eta_{p_2} \rrbracket \right\|_{\Gamma^{\text{int}}}^2 + \frac{1}{\varepsilon_{17}} \left\| \sqrt{\frac{\eta_p}{h_\Upsilon} \{\mu^{-1} k_2\}} \llbracket e_{p_2} \rrbracket \right\|_{\Gamma^{\text{int}}}^2
\end{aligned} \tag{4.53}$$

with ε_i ($i = 1, \dots, 17$) are arbitrary positive constants. After employing Lemma 4.2, the above inequality can be grouped as follows:

$$\begin{aligned}
2\mathcal{B}_{\text{stab}}^{\text{DG}}(\mathbf{H}; \mathbf{E}) & \leq \left(\frac{1}{2\varepsilon_1} + \frac{1}{2\varepsilon_3} + \frac{\mathcal{C}_{\mathbf{e}_{\mathbf{u}_1}}}{\varepsilon_{11}} \right) \left\| \sqrt{\frac{\mu}{k_1}} \mathbf{e}_{\mathbf{u}_1} \right\|^2 + \left(\frac{1}{2\varepsilon_2} + \frac{1}{2\varepsilon_4} \right) \left\| \sqrt{\frac{k_1}{\mu}} \text{grad}[e_{p_1}] \right\|^2 \\
& + \left(\frac{1}{2\varepsilon_5} + \frac{1}{2\varepsilon_7} + \frac{\mathcal{C}_{\mathbf{e}_{\mathbf{u}_2}}}{\varepsilon_{13}} \right) \left\| \sqrt{\frac{\mu}{k_2}} \mathbf{e}_{\mathbf{u}_2} \right\|^2 + \left(\frac{1}{2\varepsilon_6} + \frac{1}{2\varepsilon_8} \right) \left\| \sqrt{\frac{k_2}{\mu}} \text{grad}[e_{p_2}] \right\|^2 \\
& + \frac{1}{\varepsilon_9} \left\| \sqrt{\frac{\beta}{\mu}} (e_{p_1} - e_{p_2}) \right\|^2 \\
& + \left(\frac{1}{\varepsilon_{10}} + \frac{1}{\varepsilon_{15}} \right) \left\| \sqrt{\frac{\eta_p}{h_\Upsilon} \{\mu^{-1} k_1\}} \llbracket e_{p_1} \rrbracket \right\|_{\Gamma^{\text{int}}}^2 + \frac{1}{\varepsilon_{14}} \left\| \sqrt{\eta_u h_\Upsilon \{\mu k_1^{-1}\}} \llbracket \mathbf{e}_{\mathbf{u}_1} \rrbracket \right\|_{\Gamma^{\text{int}}}^2 \\
& + \left(\frac{1}{\varepsilon_{12}} + \frac{1}{\varepsilon_{17}} \right) \left\| \sqrt{\frac{\eta_p}{h_\Upsilon} \{\mu^{-1} k_2\}} \llbracket e_{p_2} \rrbracket \right\|_{\Gamma^{\text{int}}}^2 + \frac{1}{\varepsilon_{16}} \left\| \sqrt{\eta_u h_\Upsilon \{\mu k_2^{-1}\}} \llbracket \mathbf{e}_{\mathbf{u}_2} \rrbracket \right\|_{\Gamma^{\text{int}}}^2 \\
& + \left(\frac{\varepsilon_1}{2} + \frac{\varepsilon_2}{2} \right) \left\| \sqrt{\frac{\mu}{k_1}} \boldsymbol{\eta}_{\mathbf{u}_1} \right\|^2 + \left(\frac{\varepsilon_3}{2} + \frac{\varepsilon_4}{2} \right) \left\| \sqrt{\frac{k_1}{\mu}} \text{grad}[\eta_{p_1}] \right\|^2 \\
& + \left(\frac{\varepsilon_5}{2} + \frac{\varepsilon_6}{2} \right) \left\| \sqrt{\frac{\mu}{k_2}} \boldsymbol{\eta}_{\mathbf{u}_2} \right\|^2 + \left(\frac{\varepsilon_7}{2} + \frac{\varepsilon_8}{2} \right) \left\| \sqrt{\frac{k_2}{\mu}} \text{grad}[\eta_{p_2}] \right\|^2 \\
& + \varepsilon_9 \left\| \sqrt{\frac{\beta}{\mu}} (\eta_{p_1} - \eta_{p_2}) \right\|^2 \\
& + \varepsilon_{14} \left\| \sqrt{\eta_u h_\Upsilon \{\mu k_1^{-1}\}} \llbracket \boldsymbol{\eta}_{\mathbf{u}_1} \rrbracket \right\|_{\Gamma^{\text{int}}}^2 + \varepsilon_{15} \left\| \sqrt{\frac{\eta_p}{h_\Upsilon} \{\mu^{-1} k_1\}} \llbracket \eta_{p_1} \rrbracket \right\|_{\Gamma^{\text{int}}}^2 \\
& + \varepsilon_{16} \left\| \sqrt{\eta_u h_\Upsilon \{\mu k_2^{-1}\}} \llbracket \boldsymbol{\eta}_{\mathbf{u}_2} \rrbracket \right\|_{\Gamma^{\text{int}}}^2 + \varepsilon_{17} \left\| \sqrt{\frac{\eta_p}{h_\Upsilon} \{\mu^{-1} k_2\}} \llbracket \eta_{p_2} \rrbracket \right\|_{\Gamma^{\text{int}}}^2 \\
& + \varepsilon_{10} \left\| \sqrt{\frac{h_\Upsilon}{\eta_p} \{\mu k_1^{-1}\}} \llbracket \boldsymbol{\eta}_{\mathbf{u}_1} \rrbracket \right\|_{\Gamma^{\text{int}}}^2 + \varepsilon_{11} \left\| \sqrt{h_\Upsilon^{-1} \{\mu^{-1} k_1\}} \llbracket \eta_{p_1} \rrbracket \right\|_{\Gamma^{\text{int}}}^2 \\
& + \varepsilon_{12} \left\| \sqrt{\frac{h_\Upsilon}{\eta_p} \{\mu k_2^{-1}\}} \llbracket \boldsymbol{\eta}_{\mathbf{u}_2} \rrbracket \right\|_{\Gamma^{\text{int}}}^2 + \varepsilon_{13} \left\| \sqrt{h_\Upsilon^{-1} \{\mu^{-1} k_2\}} \llbracket \eta_{p_2} \rrbracket \right\|_{\Gamma^{\text{int}}}^2
\end{aligned} \tag{4.54}$$

We choose the coefficients of the first nine terms (i.e., blue-colored terms) in such a way that these nine terms add up to the square of $\|\mathbf{E}\|_{\text{stab}}^{\text{DG}}$. This can be achieved by choosing these coefficients as follows:

$$\begin{aligned}
\frac{1}{2\varepsilon_1} + \frac{1}{2\varepsilon_3} + \frac{\mathcal{C}_{\mathbf{e}_{\mathbf{u}_1}}}{\varepsilon_{11}} & = \frac{1}{2\varepsilon_5} + \frac{1}{2\varepsilon_7} + \frac{\mathcal{C}_{\mathbf{e}_{\mathbf{u}_2}}}{\varepsilon_{13}} = \frac{1}{2}, \quad \left(\frac{1}{2\varepsilon_2} + \frac{1}{2\varepsilon_4} \right) = \left(\frac{1}{2\varepsilon_6} + \frac{1}{2\varepsilon_8} \right) = \frac{1}{2}, \\
\frac{1}{\varepsilon_9} & = \frac{1}{\varepsilon_{14}} = \frac{1}{\varepsilon_{16}} = 1, \quad \text{and} \quad \left(\frac{1}{\varepsilon_{10}} + \frac{1}{\varepsilon_{15}} \right) = \left(\frac{1}{\varepsilon_{12}} + \frac{1}{\varepsilon_{17}} \right) = 1
\end{aligned} \tag{4.55}$$

One way to satisfy the above constraints is to make the following choices for the individual constants:

$$\begin{aligned}
\varepsilon_1 = \varepsilon_3 = \varepsilon_5 = \varepsilon_7 = 4, \quad \varepsilon_2 = \varepsilon_4 = \varepsilon_6 = \varepsilon_8 = \varepsilon_{10} = \varepsilon_{12} = \varepsilon_{15} = \varepsilon_{17} = 2, \quad \varepsilon_9 = \varepsilon_{14} = \varepsilon_{16} = 1, \\
\varepsilon_{11} = 4\mathcal{C}_{\mathbf{e}_{\mathbf{u}_1}} \quad \text{and} \quad \varepsilon_{13} = 4\mathcal{C}_{\mathbf{e}_{\mathbf{u}_2}}
\end{aligned} \tag{4.56}$$

By incorporating the above choices into inequality (4.54), we obtain the following:

$$\begin{aligned}
2(\|\mathbf{E}\|_{\text{stab}}^{\text{DG}})^2 &\leq \left(\|\mathbf{E}\|_{\text{stab}}^{\text{DG}}\right)^2 + 3\left\|\sqrt{\frac{\mu}{k_1}}\boldsymbol{\eta}_{\mathbf{u}_1}\right\|^2 + 3\left\|\sqrt{\frac{k_1}{\mu}}\text{grad}[\eta_{p_1}]\right\|^2 \\
&\quad + 3\left\|\sqrt{\frac{\mu}{k_2}}\boldsymbol{\eta}_{\mathbf{u}_2}\right\|^2 + 3\left\|\frac{k_2}{\sqrt{\mu}}\text{grad}[\eta_{p_2}]\right\|^2 + \left\|\sqrt{\frac{\beta}{\mu}}(\eta_{p_1} - \eta_{p_2})\right\|^2 \\
&\quad + 2\left\|\sqrt{\frac{\eta_p}{h_\Upsilon}}\{\{\mu^{-1}k_1\}\}[\eta_{p_1}]\right\|_{\Gamma^{\text{int}}}^2 + 2\left\|\sqrt{\frac{\eta_p}{h_\Upsilon}}\{\{\mu^{-1}k_2\}\}^{1/2}[\eta_{p_2}]\right\|_{\Gamma^{\text{int}}}^2 \\
&\quad + \left\|\sqrt{\eta_u h_\Upsilon}\{\{\mu k_1^{-1}\}\}[\boldsymbol{\eta}_{\mathbf{u}_1}]\right\|_{\Gamma^{\text{int}}}^2 + \left\|\sqrt{\eta_u h_\Upsilon}\{\{\mu k_2^{-1}\}\}[\boldsymbol{\eta}_{\mathbf{u}_2}]\right\|_{\Gamma^{\text{int}}}^2 \\
&\quad + 4\mathcal{C}_{\mathbf{e}_{\mathbf{u}_1}}\left\|\sqrt{h_\Upsilon^{-1}}\{\{\mu^{-1}k_1\}\}[\eta_{p_1}]\right\|_{\Gamma^{\text{int}}}^2 + 4\mathcal{C}_{\mathbf{e}_{\mathbf{u}_2}}\left\|\sqrt{h_\Upsilon^{-1}}\{\{\mu^{-1}k_2\}\}[\eta_{p_2}]\right\|_{\Gamma^{\text{int}}}^2 \\
&\quad + 2\left\|\sqrt{\frac{h_\Upsilon}{\eta_p}}\{\{\mu k_1^{-1}\}\}[\boldsymbol{\eta}_{\mathbf{u}_1}]\right\|_{\Gamma^{\text{int}}}^2 + 2\left\|\sqrt{\frac{h_\Upsilon}{\eta_p}}\{\{\mu k_2^{-1}\}\}[\boldsymbol{\eta}_{\mathbf{u}_2}]\right\|_{\Gamma^{\text{int}}}^2 \\
&\leq \left(\|\mathbf{E}\|_{\text{stab}}^{\text{DG}}\right)^2 + 6\left(\|\mathbf{H}\|_{\text{stab}}^{\text{DG}}\right)^2 \\
&\quad + 4\mathcal{C}_{\mathbf{e}_{\mathbf{u}_1}}\left\|\sqrt{h_\Upsilon^{-1}}\{\{\mu^{-1}k_1\}\}[\eta_{p_1}]\right\|_{\Gamma^{\text{int}}}^2 + 4\mathcal{C}_{\mathbf{e}_{\mathbf{u}_2}}\left\|\sqrt{h_\Upsilon^{-1}}\{\{\mu^{-1}k_2\}\}[\eta_{p_2}]\right\|_{\Gamma^{\text{int}}}^2 \\
&\quad + 2\left\|\sqrt{\frac{h_\Upsilon}{\eta_p}}\{\{\mu k_1^{-1}\}\}[\boldsymbol{\eta}_{\mathbf{u}_1}]\right\|_{\Gamma^{\text{int}}}^2 + 2\left\|\sqrt{\frac{h_\Upsilon}{\eta_p}}\{\{\mu k_2^{-1}\}\}[\boldsymbol{\eta}_{\mathbf{u}_2}]\right\|_{\Gamma^{\text{int}}}^2 \tag{4.57}
\end{aligned}$$

Lemma 4.3 implies the following:

$$\begin{aligned}
\left(\|\mathbf{E}\|_{\text{stab}}^{\text{DG}}\right)^2 &\lesssim 6\left(\|\mathbf{H}\|_{\text{stab}}^{\text{DG}}\right)^2 + \sum_{\omega \in \mathcal{T}_h} \left(h_\omega^{2(p+1)}|\mathbf{u}_1|_{H^{p+1}(\omega)}^2 + h_\omega^{2(q+1)}|\mathbf{u}_2|_{H^{q+1}(\omega)}^2 \right. \\
&\quad \left. + h_\omega^{2r}|p_1|_{H^{r+1}(\omega)}^2 + h_\omega^{2s}|p_2|_{H^{s+1}(\omega)}^2 \right) \tag{4.58}
\end{aligned}$$

As $h \rightarrow 0$, $h_\omega \rightarrow 0 \forall \omega \in \mathcal{T}_h$, which in turn implies that $\|\mathbf{H}\|_{\text{stab}}^{\text{DG}} \rightarrow 0$ (using Lemma 4.4) and all other terms on the right hand side tend to zero (using Lemma 4.3). Thus, $\|\mathbf{E}\|_{\text{stab}}^{\text{DG}} \rightarrow 0$ as $h \rightarrow 0$. Since $\|\cdot\|_{\text{stab}}^{\text{DG}}$ is a norm (i.e., Lemma 4.1), one can conclude that $\mathbf{U}^h \rightarrow \mathbf{U}$ almost everywhere as $h \rightarrow 0$. \square

REMARK 4.1. *The selection of constants ε_i ($i = 1, \dots, 17$) in equation (4.56) is arbitrary. We do not claim that this selection provides an optimal bound, which is not the aim of our paper. However, the selection is sufficient to establish the convergence of the proposed formulation.*

Lemmas 4.3 and 4.4 immediately give the following result:

COROLLARY 4.7. *(Rates of convergence.) Let p, q, r and s be the polynomial orders for approximating the fields $\mathbf{u}_1, \mathbf{u}_2, p_1$ and p_2 . Let the orders of regularity in terms of the Sobolev semi-norm for these solution fields be $\hat{p}, \hat{q}, \hat{r}$ and \hat{s} . Then the rates of convergence for these fields will be, respectively, $\min[p + 1, \hat{p}]$, $\min[q + 1, \hat{q}]$, $\min[r, \hat{r}]$ and $\min[s, \hat{s}]$.*

REMARK 4.2. *In order for Lemma 4.3 to hold, $\eta_p \neq 0$, as η_p is in the denominator of the estimates (4.22) and (4.23). Since the convergence theorem utilizes Lemma 4.3, the convergence of*

the proposed DG formulation is thus established for the case $\eta_p \neq 0$. However, numerical simulations suggest that the parameters η_u and η_p do not seem to have a noticeable effect on the results for problems involving conforming meshes and conforming interpolations.

5. PATCH TESTS

Patch tests are generally used to indicate the quality of a finite element. Despite some debated mathematical controversies regarding the patch test, “the patch test is the most practically useful technique for assessing element behavior” as nicely pinpointed by [Hughes, 2012]. In this section, different constant flow patch tests are used to showcase various features of the proposed stabilized mixed DG formulation. First, the capability of the proposed formulation for modeling flow in a highly heterogeneous, layered porous domain with abrupt changes in macro- and micro-permeabilities, is shown. Then, the ability of the proposed stabilized mixed DG formulation for supporting non-conforming discretization, in the form of non-conforming order refinement and non-conforming element refinement, is assessed. Finally, the proposed stabilized mixed DG formulation is employed on meshes with non-constant Jacobian elements. For the case of non-conforming order refinement, a parametric study is performed to assess the sensitivity of the solutions with respect to the stabilization parameters η_u and η_p .

5.1. Velocity-driven patch test. In reality, heterogeneity of the material properties is indispensable when it comes to porous domains. In many geological systems, medium properties can vary by many orders of magnitude and rapid changes may occur over small spatial scales. The aim of this boundary value problem is to show that the proposed stabilized mixed DG formulation can perform satisfactorily when the medium properties are heterogeneous.

The heterogeneous domain consists of five horizontal layers with different macro- and micro-permeabilities in each layer. As shown in **Fig. 3**, on the left side of each layer, a constant normal velocity ($\mathbf{u}_i \cdot \hat{\mathbf{n}} = -\frac{k_i^{\# \text{ layer}}}{\mu}$) is applied and on the right side, $\mathbf{u}_i \cdot \hat{\mathbf{n}} = \frac{k_i^{\# \text{ layer}}}{\mu}$ is prescribed. On the top and bottom of the domain, normal components of macro- and micro-velocities are prescribed to be zero. For uniqueness of the solution, pressure is prescribed on one corner of the domain. Table 1 provides the model parameters for this problem.

TABLE 1. Model parameters for velocity-driven patch test.

Parameter	Value
$\gamma \mathbf{b}$	{0.0, 0.0}
L_x	5.0
L_y	4.0
μ	1.0
β	1.0
k	0.2
η_u	100.0
η_p	100.0
h	structured T3 mesh of size 0.04 used

As can be seen in **Fig. 4**, velocities are constant and pressures are linearly varying in the horizontal direction in each layer, which are in agreement with the exact solution of this problem

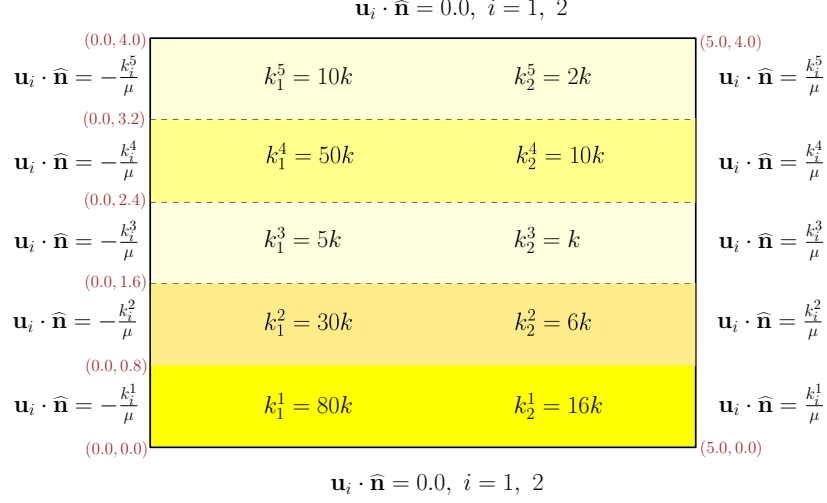


FIGURE 3. Velocity-driven patch test: This figure shows the computational domain, boundary conditions, and macro- and micro-permeabilities in each layer.

as remarked by [Hughes et al., 2006]. This problem is also solved using the stabilized continuous Galerkin (CG) formulation of the DPP model developed by [Joodat et al., 2018] and the x-components of velocity profiles are compared under both DG and CG formulations at $x=2.5$ throughout the domain as shown in **Fig. 5**. As can be seen, spurious oscillations are observed along the interfaces of the layers under the CG formulation. Under the DG formulation, however, such oscillations are completely eliminated and the physical jumps in the velocity profiles are accurately captured across the interfaces.

5.2. Non-conforming discretization. One of the features of DG formulations is that the global error of the computation can be controlled by adjusting the numerical resolution in a selected set of the elements. Such a *non-conforming discretization* can be obtained in two ways [Hesthaven and Warburton, 2007]: One can either modify the local order of the interpolation, or locally change the element size in parts of the computational domain. [Babuška and Dorr, 1981; Babuška and Strouboulis, 2001] have discussed that the former method, also known as *non-conforming order refinement* or *non-conforming polynomial orders*, is more preferred for smooth problems. However, for the non-smooth case, which is due to the geometric features, sources, or boundary conditions, *non-conforming element refinement* is the best choice. In the following, we show the application of non-conforming discretization under the proposed stabilized DG formulation using simply designed boundary value problems.

5.2.1. *Non-conforming polynomial orders.* Since the element communication under the DG formulations takes place through fluxes, each element can independently possess a desired order of interpolation. Hence, the DG methods can easily support the non-conforming polynomial orders (see [Canouet et al., 2005; Hesthaven and Warburton, 2004; Remacle et al., 2003]).

In order to investigate the performance of our proposed stabilized mixed DG formulation under non-conforming polynomial orders, a problem taken from [Joodat et al., 2018] is used. The domain is considered to be a unit square, with pressures being prescribed on the entire boundary of both pore-networks as shown in **Fig. 6**. Prescribed pressure values on the respective boundary edges are obtained using the analytical solutions of this problem. The analytical solution for the pressure

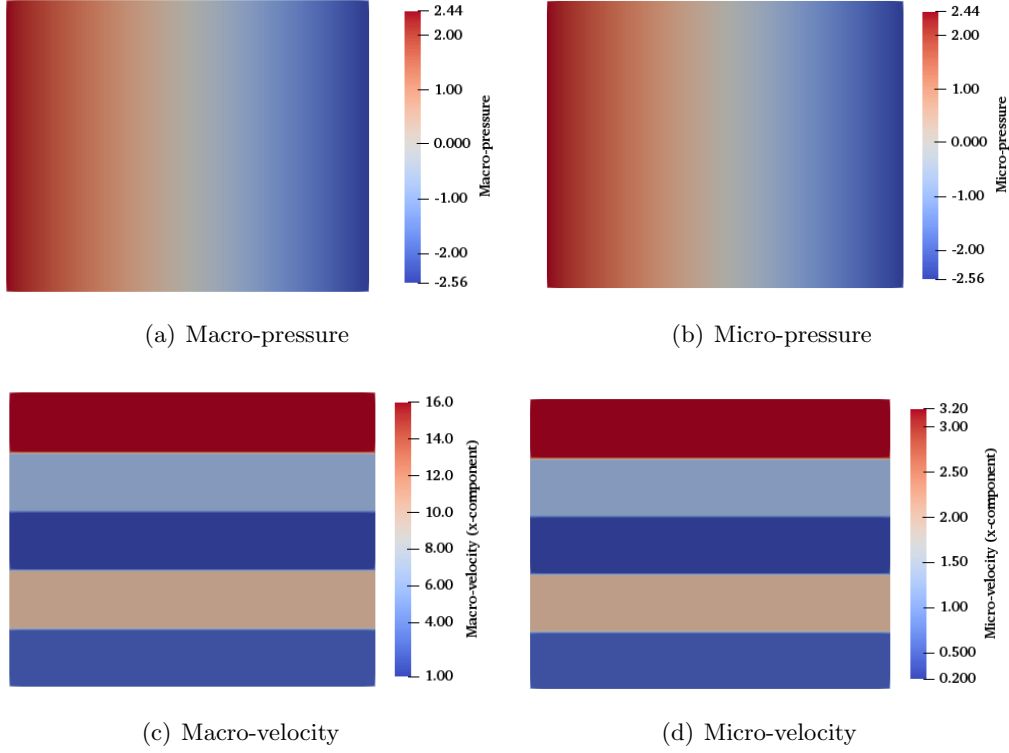


FIGURE 4. Velocity-driven patch test: Velocities are constant within each layer and pressures are linearly varying in the horizontal direction which are in agreement with the exact solution of this problem. These results imply that the proposed formulation has successfully passed the velocity-driven patch test.

and velocity fields can be written as

$$p_1(x, y) = \frac{\mu}{\pi} \exp(\pi x) \sin(\pi y) - \frac{\mu}{\beta k_1} \exp(\eta y) \quad (5.1)$$

$$p_2(x, y) = \frac{\mu}{\pi} \exp(\pi x) \sin(\pi y) + \frac{\mu}{\beta k_2} \exp(\eta y) \quad (5.2)$$

$$\mathbf{u}_1(x, y) = -k_1 \begin{pmatrix} \exp(\pi x) \sin(\pi y) \\ \exp(\pi x) \cos(\pi y) \end{pmatrix} + \begin{pmatrix} 0 \\ \frac{\eta}{\beta} \exp(\eta y) \end{pmatrix} \quad (5.3)$$

$$\mathbf{u}_2(x, y) = -k_2 \begin{pmatrix} \exp(\pi x) \sin(\pi y) \\ \exp(\pi x) \cos(\pi y) \end{pmatrix} - \begin{pmatrix} 0 \\ \frac{\eta}{\beta} \exp(\eta y) \end{pmatrix} \quad (5.4)$$

where

$$\eta := \sqrt{\beta \frac{k_1 + k_2}{k_1 k_2}} \quad (5.5)$$

η is a useful parameter to characterize the flow of fluids through porous media with double porosity/permeability [Nakshatrala et al., 2018].

Table 2 provides the parameter values for this problem. In the left and right parts of the domain, two different sets of equal-order interpolation are employed for velocities and pressures as shown in Fig. 7. In the left half, third order interpolation polynomials are employed for velocities

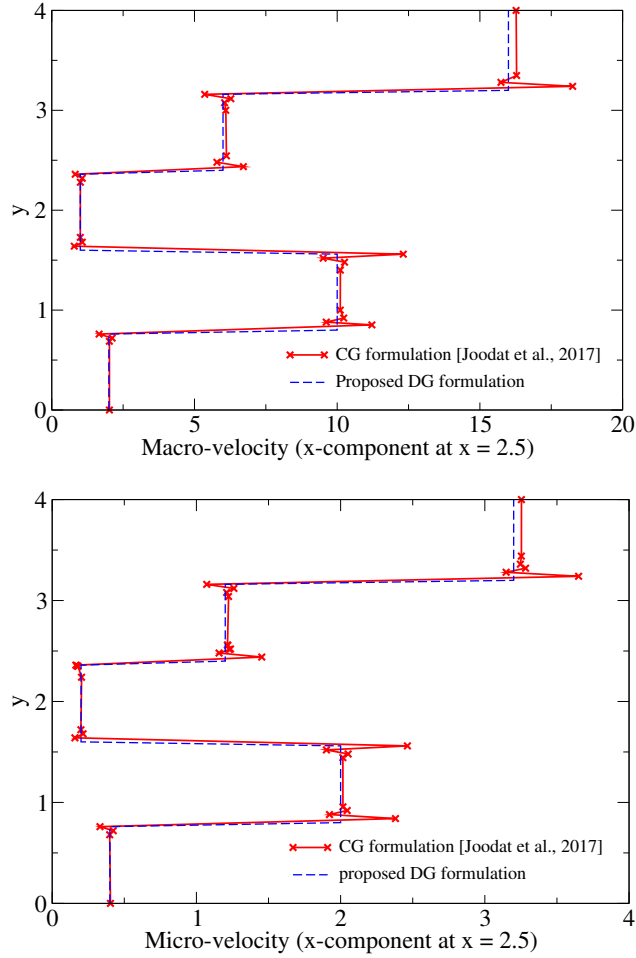


FIGURE 5. Velocity-driven patch test: This figure compares the velocities profiles obtained under the stabilized mixed CG formulation and the proposed DG formulation. The x-components of the macro-velocity (top) and micro-velocity (bottom) at $x = 2.5$ are plotted. Under the CG formulation, overshoots and undershoots are observed along the interfaces of the layers. On the other hand, the proposed DG formulation is able to capture the physical jumps across the interfaces.

and pressures in each pore-network while in the right half, first-order interpolation polynomials are used.

Smooth velocity profiles along the non-conforming edge ($x = 0.5$) are not achievable for a coarse mesh (e.g., of size 10×10 elements mesh) without using extra stabilization terms (i.e., $\eta_u = \eta_p = 0$). One can either apply exhaustive mesh refinement, which in turn leads to a much higher computational cost, or can circumvent the unnecessary refinements by alternatively taking advantage of non-zero η_u and η_p . **Figs. 8–10** illustrate the sensitivity of x-component of velocities along the non-conforming edge with respect to η_u , η_p and their combined effect. According to **Figs. 8(a)** and **8(b)**, the increase in η_p per se in the absence of η_u slightly improves the results. However, for the case of $\eta_p = 0$ and non-zero η_u , a drastic enhancement is captured with η_u of order

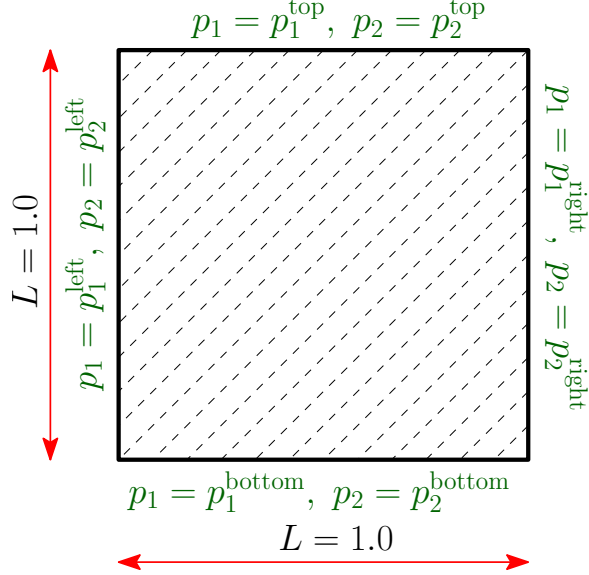


FIGURE 6. Non-conforming polynomial orders: The computational domain in the 2D setting is a unit square. Pressures are prescribed on the entire boundary of both pore-networks. Prescribed pressure values on the respective boundary edges are obtained using the analytical solutions (5.1) and (5.2).

TABLE 2. Model parameters for non-conforming polynomial orders, element-wise mass balance study, and 2D numerical convergence analysis.

Parameter	Value
$\gamma \mathbf{b}$	$\{0.0, 0.0\}$
L	1.0
μ	1.0
β	1.0
k_1	1.0
k_2	0.1
η	$\sqrt{11} \simeq 3.3166$
η_u	10.0
η_p	1.0
h	structured T3 mesh of size 0.1 used
$p_i^{\text{left}}, i = 1, 2$ $p_i^{\text{right}}, i = 1, 2$ $p_i^{\text{top}}, i = 1, 2$ $p_i^{\text{bottom}}, i = 1, 2$	Obtained by evaluating the analytical solution (equations (5.1) and (5.2)) on the respective boundaries.

one as shown in **Figs. 9(a)** and **9(b)**. **Figs. 10(a)** and **10(b)** show the combined effect of η_u and η_p along the non-conforming edge in minimizing the drifts of macro and micro-velocity fields.

Figs. 11 and **12** compare the exact and numerical solutions for the pressure and velocity fields by taking $\eta_u = 10$ and $\eta_p = 1$. As can be seen, the numerical and the exact solutions

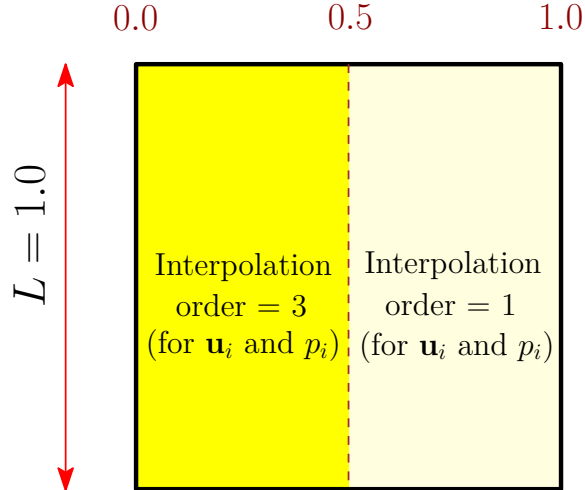


FIGURE 7. Non-conforming polynomial orders: Different sets of equal-order interpolations used for this problem are shown in this figure. In the left part of the domain, third order interpolation polynomials are used for velocities and pressures, while in the right part, first order interpolation polynomials are used.

match, which implies that the proposed mixed DG formulation can nicely handle non-conforming polynomial orders. [Badia and Codina, 2010] suggests the need for such additional stabilization terms for modeling flow under Darcy equations. However, to the best of the authors' knowledge, no numerical simulation has been reported to quantify the effect of these stabilization parameters on the accuracy of results under the DPP model for the problems exhibiting mismatching interpolation order.

5.2.2. *Non-conforming element refinement.* In mesh refinement procedures, one can either uphold the conformity of the mesh or produce irregular (non-conforming) meshes. The ability of DG formulations to support non-conforming elements obviates the user from propagating refinements beyond the desired elements [Hesthaven and Warburton, 2007]. The non-conforming meshes introduce *hanging nodes* on the edge of neighboring elements. In general, there are two strategies for handling non-matching interface discretization. In the first approach, extra degrees of freedom are assigned to the hanging nodes; hence the shape functions are generated on both regular and hanging nodes in such a way that both Kronecker delta and partition of unity properties are satisfied. Constructing these special shape functions for two- and three-dimensional problems is discussed in [Gupta, 1978; Morton et al., 1995]. In the second approach, which is known as constrained approximation, the shape functions are generated only on the corner nodes of each element and the stiffness matrix is assembled via conventional algorithms. The constraints at hanging nodes are then designed to be the average of their neighboring corner nodes. This can be enforced either through Lagrange multipliers or multiplication by the connectivity matrix [Ainsworth and Senior, 1997; Bank et al., 1983]. This method is a classical standard procedure in treatment of mismatching grids and hanging nodes. For further details refer to [Oden et al., 1989]. Herein, we resort to the second approach by introducing *virtual nodes*, as the refinement algorithm is more straightforward compared to the first approach [Fries et al., 2011].

Applications of mesh refinement in the light of DG formulations are provided by [Burstedde et al., 2008; Hartmann and Houston, 2002; Koper and Giraldo, 2014], where the numerical fluxes

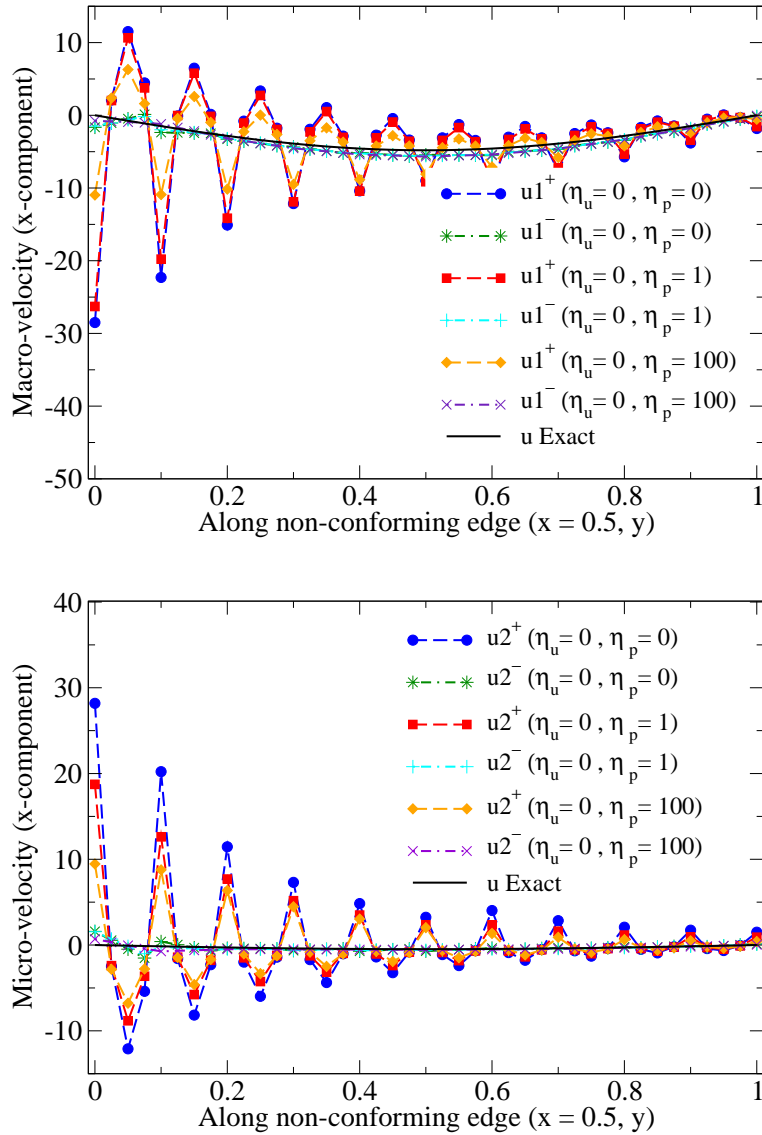


FIGURE 8. Non-conforming polynomial orders: This parametric study demonstrates that an increase in η_p in the absence of η_u slightly improves the accuracy in capturing the jumps of the (macro- and micro-) velocities across a non-conforming edge.

on the non-conforming meshes are incorporated in the DG solver. In the following problem, the capability of our proposed stabilized mixed DG formulation for supporting the non-conforming element refinement is investigated. The domain is homogeneous with pressures being prescribed on the left and right boundaries of both pore-networks. The normal components of velocities are zero on top and bottom of the domain. The model parameters for this problem can be found in Table 3. The refinement provided is based on physical considerations and takes place on the right half of the domain, where the mismatching edge is shared by more than two elements, as can be seen in Fig. 13(a).

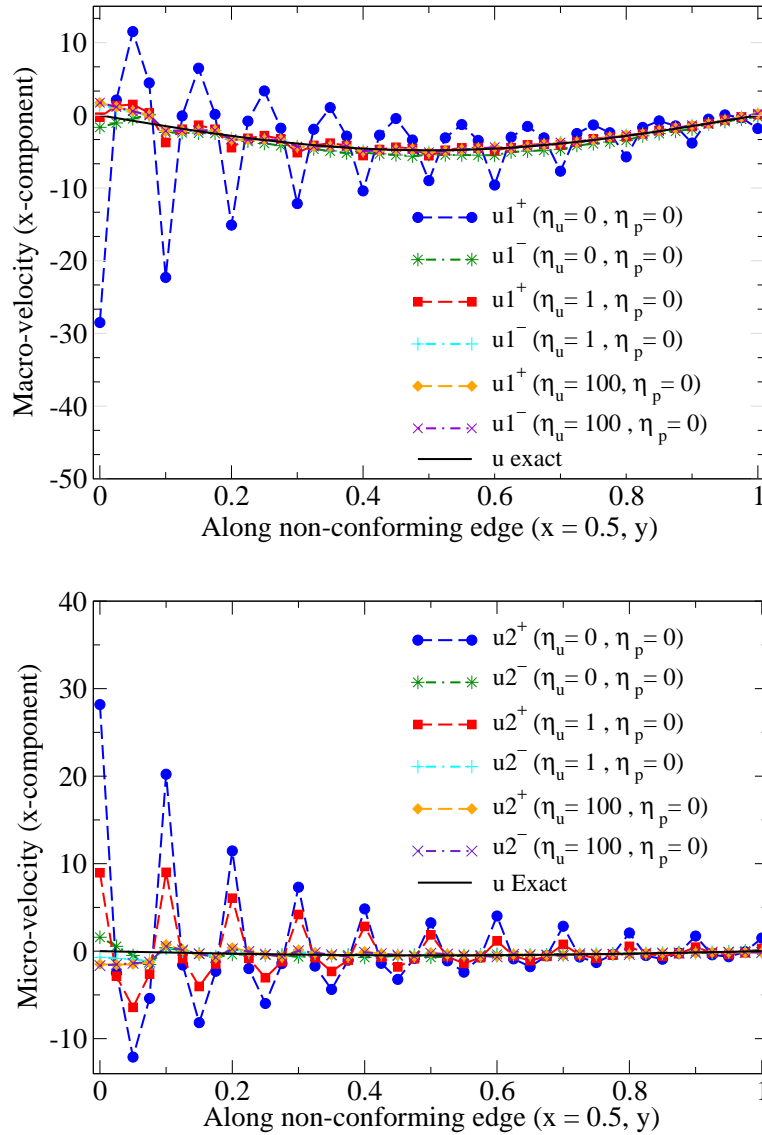


FIGURE 9. Non-conforming polynomial orders: This figure shows a parametric study performed on the effect of η_u on velocity profiles. For the case of $\eta_p = 0$ and non-zero η_u , a drastic enhancement is captured with η_u of order 1.

The virtual nodes laid down on the non-conforming boundary face (nodes 13 and 14 in **Fig. 13(b)**), each store a linear interpolation of nodes 2 and 3. These nodes (similar to hanging nodes 8 and 9) do not initially impose any additional degrees of freedom and are merely auxiliary nodes on the edge of element 1 for programming convenience. The usual DG algorithm for the assembly of the global stiffness matrix is followed. Then, we enforce constraints for degrees of freedom corresponding to hanging nodes (and virtual nodes) by Lagrange multiplier's approach as described in details in [Fries et al., 2011; Karniadakis and Sherwin, 2013]. At this stage, the interactions of node 8 with nodes 2 and 3 was facilitated via virtual node 13, and similarly, the interaction of node 9

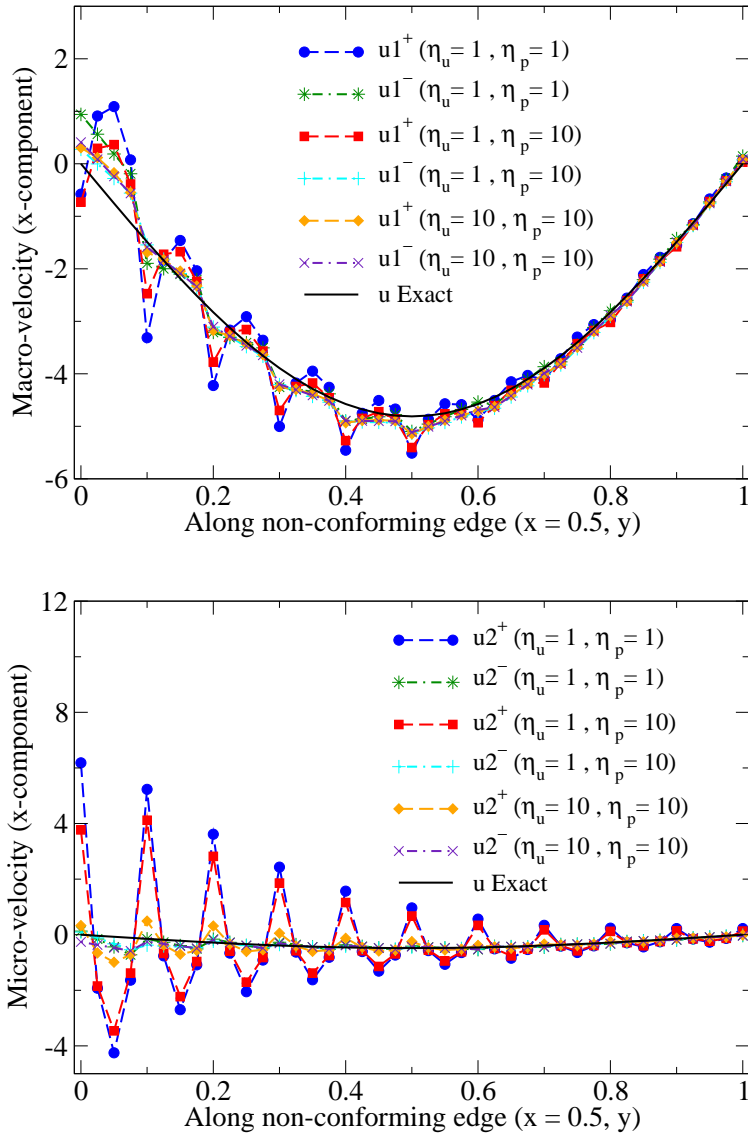


FIGURE 10. Non-conforming polynomial orders: This figure shows a parametric study performed on the combined effect of η_u and η_p on minimizing the drifts of macro and micro-velocity fields.

with nodes 2 and 3 was assisted via virtual node 14. **Fig. 14** shows the velocity and pressure profiles within the domain. Pressures in both pore-networks are varying linearly and velocities are constant throughout the domain. These results show that the proposed stabilized DG formulation is capable of handling non-conforming element refinement (with hanging nodes in the mesh).

5.3. Non-constant Jacobian elements. In practice, many hydrogeological systems have complex shapes and modeling of such domains, especially in the 3D settings, requires using of elements with irregular shapes. Divergent boundaries in such elements result in non-constant Jacobian

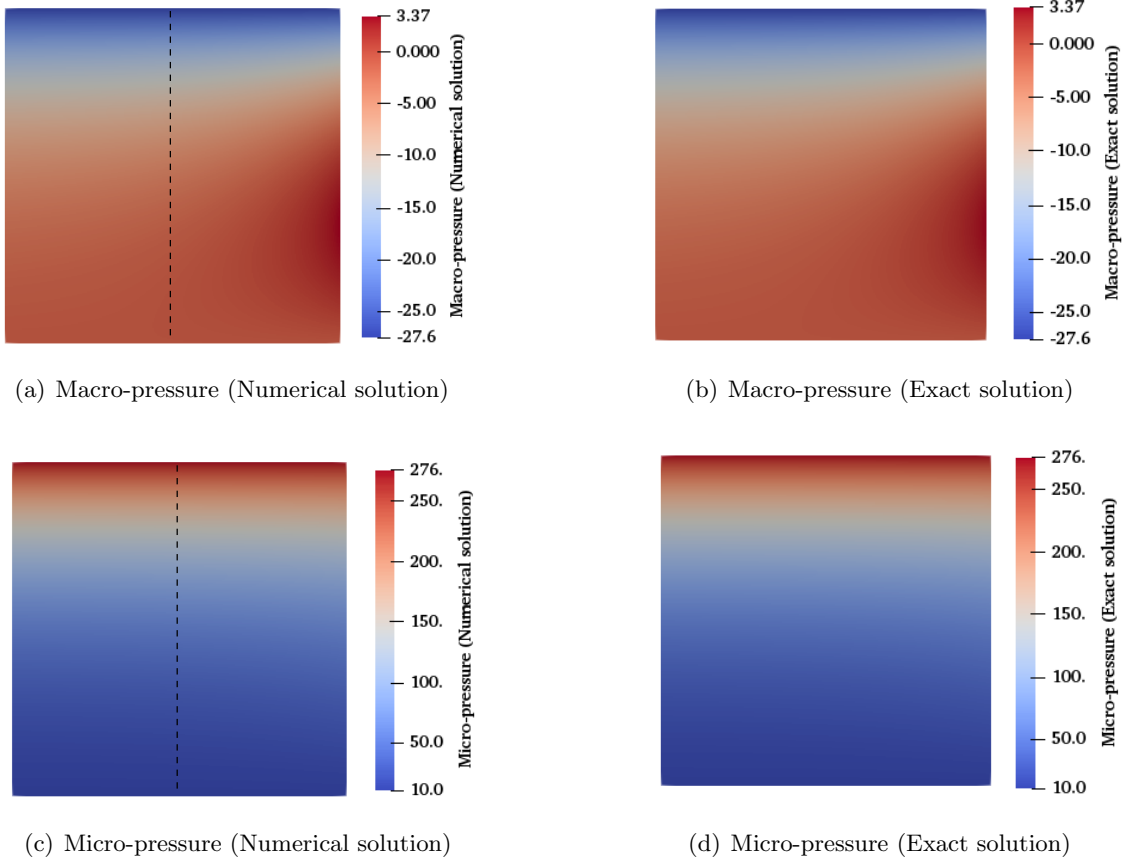


FIGURE 11. Non-conforming polynomial orders: This figure shows the exact and numerical solutions for the pressure profiles within the domain. In the left half of the domain, third order interpolation polynomials are used for velocities and pressures, while in the right half, first order interpolation polynomials are used. The exact and numerical solutions match which shows that the proposed stabilized DG formulation supports non-conforming order refinement.

TABLE 3. Model parameters for non-conforming element refinement problem.

Parameter	Value
$\gamma \mathbf{b}$	$\{0.0, 0.0\}$
L_x	2.0
L_y	1.0
μ	1.0
β	1.0
k_1	1.0
k_2	0.1
η_u	0.0
η_p	0.0

determinants. Herein, the aim is to show that the proposed stabilized mixed DG formulation can

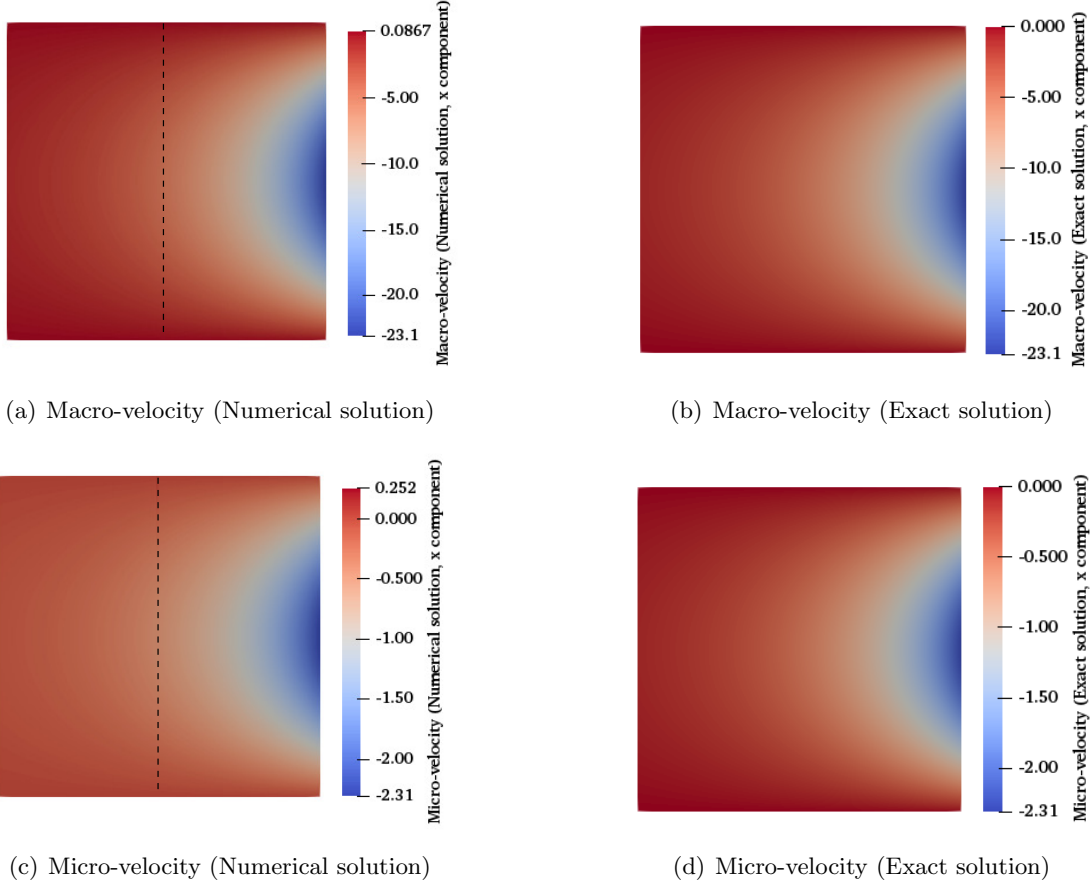


FIGURE 12. Non-conforming polynomial orders: This figure shows the exact and numerical solutions for the velocity profiles within the domain. In the left half of the domain, third order interpolation polynomials are used for velocities and pressures, while in the right half, first order interpolation polynomials are used. The exact and numerical solutions match which shows the proposed stabilized DG formulation supports non-conforming order refinement.

perform satisfactorily to model flow through computational domains composed of non-constant Jacobian elements. It will be shown that under the equal-order interpolation for the field variables, our proposed formulation is still able to pass the constant flow patch test with irregular elements. Two different computational domains with sample meshes having non-constant Jacobian brick elements are depicted in **Fig. 15** and model parameters are provided in Table 4. Pressures are prescribed at both left and right faces of the two pore-networks ($p_1(x = 0, y, z) = p_2(x = 0, y, z) = p^L$ and $p_1(x = 1, y, z) = p_2(x = 1, y, z) = p^R$). On the other faces, the normal component of velocity in both pore-networks is assumed to be zero (i.e., $\mathbf{u}_1 \cdot \hat{\mathbf{n}} = \mathbf{u}_2 \cdot \hat{\mathbf{n}} = 0$). The pressure and velocity profiles for both domains are shown in **Figs. 16** and **17**. In both domains, pressures are varying linearly from the left face to the right one and velocities are constant throughout the domain as expected. These results show that the proposed mixed DG formulation is capable of providing accurate results using non-constant Jacobian elements.

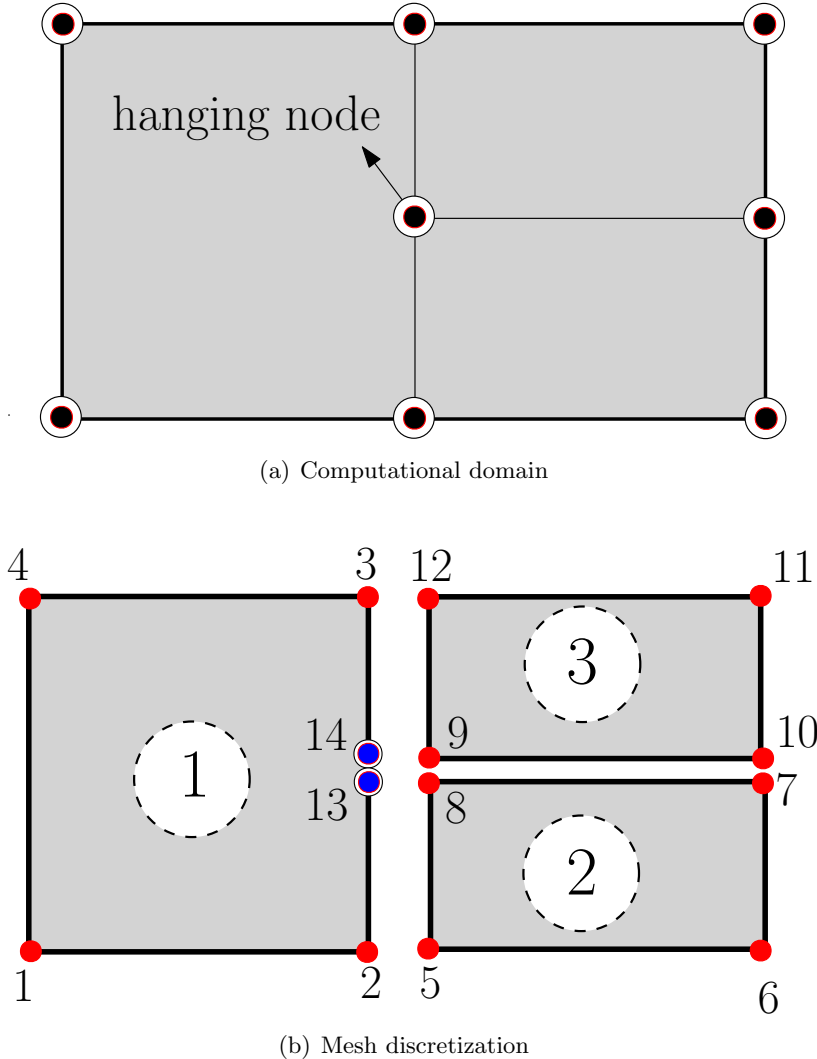


FIGURE 13. Non-conforming element refinement: The top figure shows the representative computational domain with non-conforming element refinement (the hanging node on the non-conforming boundary is shown). The bottom figure shows the DG discretization of this domain. The blue nodes are the virtual nodes, each of which are a linear interpolation of nodes 2 and 3. They do not jack up the order of stiffness matrix as no degree of freedom is assigned to them.

6. NUMERICAL CONVERGENCE ANALYSIS

In this section, we perform numerical convergence analysis of the proposed stabilized DG formulation with respect to both h - and p -refinements.

6.1. 2D numerical convergence analysis: Convergence analysis in the 2D setting is performed on the boundary value problem described in Section 5.2.1. This problem was also employed by [Joodat et al., 2018] for the convergence analysis of the stabilized mixed *continuous* Galerkin (CG) formulation of the DPP model. The exact solutions for the pressures and velocities are provided by equations (5.1) – (5.4). The domain for this problem is homogeneous (macro- and

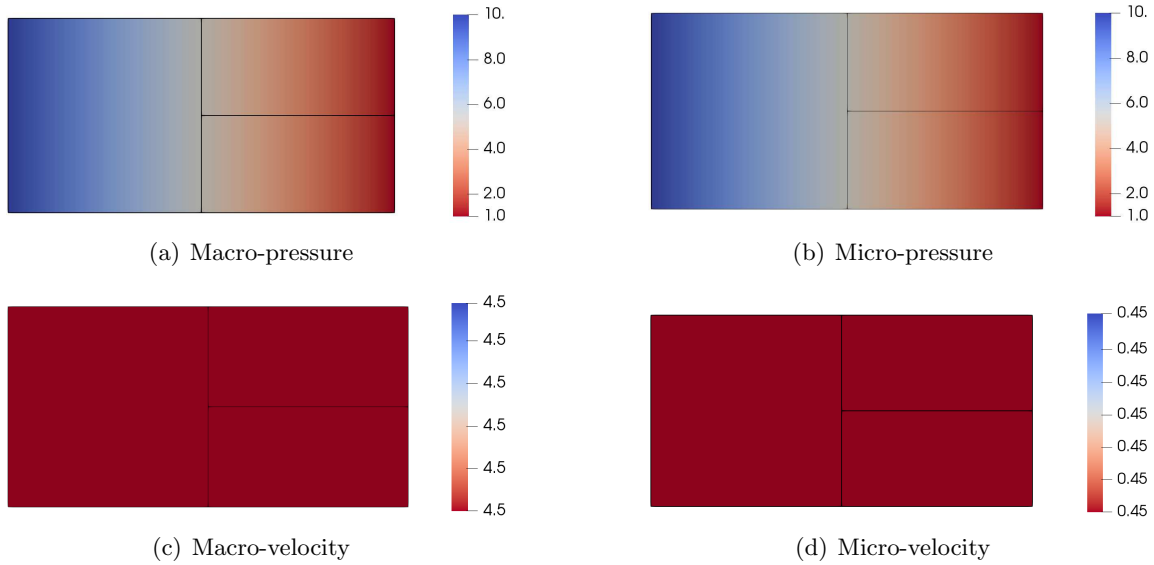


FIGURE 14. Non-conforming element refinement: Pressures in both pore-networks are varying linearly and velocities are constant throughout the domain. These results show that the proposed stabilized DG formulation is capable of handling non-conforming element refinement (with hanging nodes in the mesh).

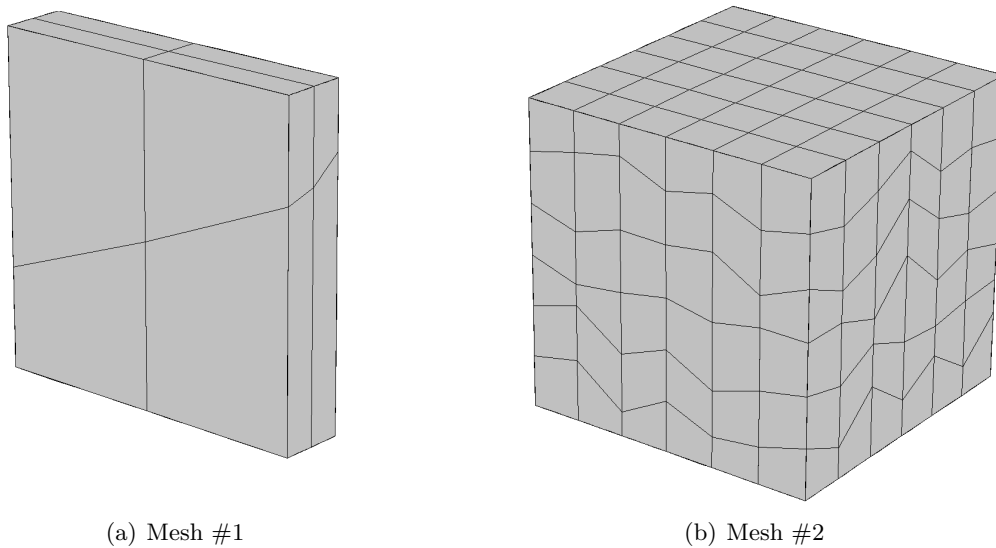


FIGURE 15. Non-constant Jacobian elements: This figure shows two different computational domains and their corresponding meshes for the constant flow patch test. For this problem, non-constant Jacobian brick elements are used.

micro-permeabilities are constant within the domain) and same equal-order interpolations are used throughout the domain. The computational domain is shown in **Fig. 6** and the parameter values are provided in Table 2. The three-node triangular element (T3), which is a simplicial finite element, is employed in the numerical simulation and the convergence is obtained under both *h-refinement*

TABLE 4. Model parameters for 3D computational domains with non-constant Jacobian elements.

Parameter	Mesh #1	Mesh #2
$\gamma\mathbf{b}$	{0.0, 0.0, 0.0}	{0.0, 0.0, 0.0}
L_x	1.0	1.0
L_y	1.0	0.2
L_z	1.0	1.0
μ	1.0	1.0
β	1.0	1.0
k_1	1.0	1.0
k_2	0.1	0.1
η_u	0.0	0.0
η_p	0.0	0.0

and p -refinement. In **Figs. 18** and **19**, the convergence rates under h -refinement and p -refinement are provided for the L_2 -norm and the H^1 -norm of the pressure fields in the two pore-networks. The rates of convergence under h - and p -refinements are observed to be polynomial and exponential, respectively. These results are in accordance with the theory (viz. Corollary 4.7).

6.2. 3D numerical convergence analysis. The computational domain of this problem is a unit cube with pressure being prescribed on the entire boundary of the two pore-networks. The analytical solution takes the following form:

$$p_1(x, y, z) = \frac{\mu}{\pi} \exp(\pi x) (\sin(\pi y) + \sin(\pi z)) - \frac{\mu}{\beta k_1} (\exp(\eta y) + \exp(\eta z)) \quad (6.1)$$

$$p_2(x, y, z) = \frac{\mu}{\pi} \exp(\pi x) (\sin(\pi y) + \sin(\pi z)) + \frac{\mu}{\beta k_2} (\exp(\eta y) + \exp(\eta z)) \quad (6.2)$$

$$\mathbf{u}_1(x, y, z) = -k_1 \exp(\pi x) \begin{pmatrix} \sin(\pi y) + \sin(\pi z) \\ \cos(\pi y) \\ \cos(\pi z) \end{pmatrix} + \frac{\eta}{\beta} \begin{pmatrix} 0 \\ \exp(\eta y) \\ \exp(\eta z) \end{pmatrix} \quad (6.3)$$

$$\mathbf{u}_2(x, y, z) = -k_2 \exp(\pi x) \begin{pmatrix} \sin(\pi y) + \sin(\pi z) \\ \cos(\pi y) \\ \cos(\pi z) \end{pmatrix} - \frac{\eta}{\beta} \begin{pmatrix} 0 \\ \exp(\eta y) \\ \exp(\eta z) \end{pmatrix} \quad (6.4)$$

Pressure boundary conditions on each face are obtained by evaluating the analytical solution on the corresponding boundary of each pore-network. Table 5 provides the parameter values employed in the numerical simulation.

The eight-node brick element (B8), which is a non-simplicial element, is employed in this numerical simulation. **Figs. 20** and **21** respectively provide the convergence rates under h -refinement and p -refinement for the L_2 -norm and the H^1 -norm of the pressure fields in the two pore-networks. As can be seen, the rates of convergence under the h - and p -refinements are polynomial and exponential, respectively; which are in accordance with the theory (viz. Corollary 4.7).

7. CANONICAL PROBLEM AND STRUCTURE PRESERVING PROPERTIES

In this section, first, robustness of the proposed stabilized mixed DG formulation is assessed using a standard test problem, with abrupt changes in material properties and elliptic singularities. In the literature, this problem is typically referred to as the quarter five-spot checkerboard problem.

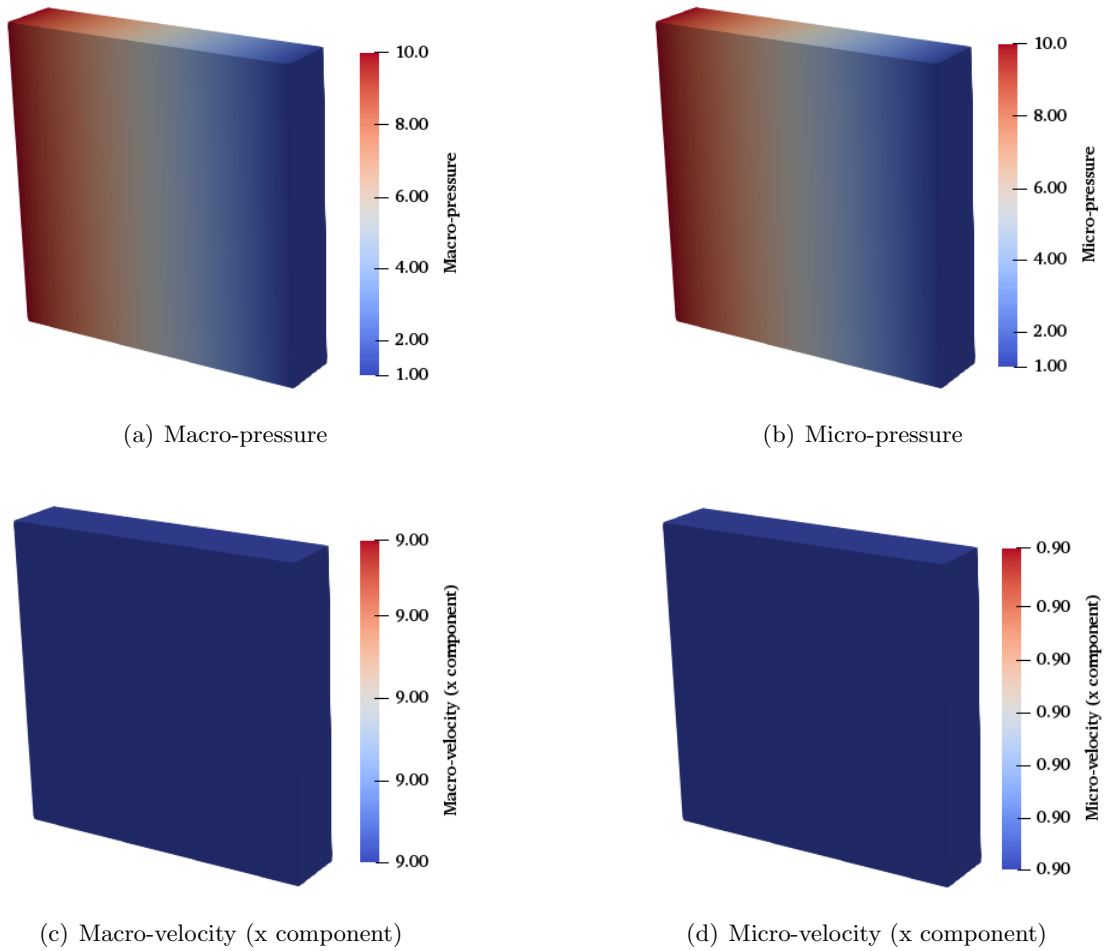


FIGURE 16. Non-constant Jacobian elements: Pressure and velocity profiles are shown for Mesh #1 (Fig. 15(a)) with non-constant Jacobian elements. Pressures are varying linearly from the left face to the right one and velocities are constant throughout the domain as expected. These results show that the proposed mixed DG formulation is capable of providing accurate results using non-constant Jacobian elements.

Second, the element-wise mass balance property associated with the CG and DG formulations is compared.

7.1. Quarter five-spot checkerboard problem. The original form of this problem, known as “five-spot problem” with homogeneous properties, has been firstly designed for the Darcy equations. Herein, we extend this problem to the DPP model with modified boundary conditions and heterogeneous medium properties. Fig. 22 shows the computational domain and the boundary conditions for the five-spot problem. An injection well surrounded by four production wells placed at four corners of a square domain form a typical setting in the enhanced oil recovery applications. The underlying symmetry allows for solving the problem only in the top right quadrant, which is referred to as a “quarter” five-spot problem. In the well-known “checkerboard problem”, such a

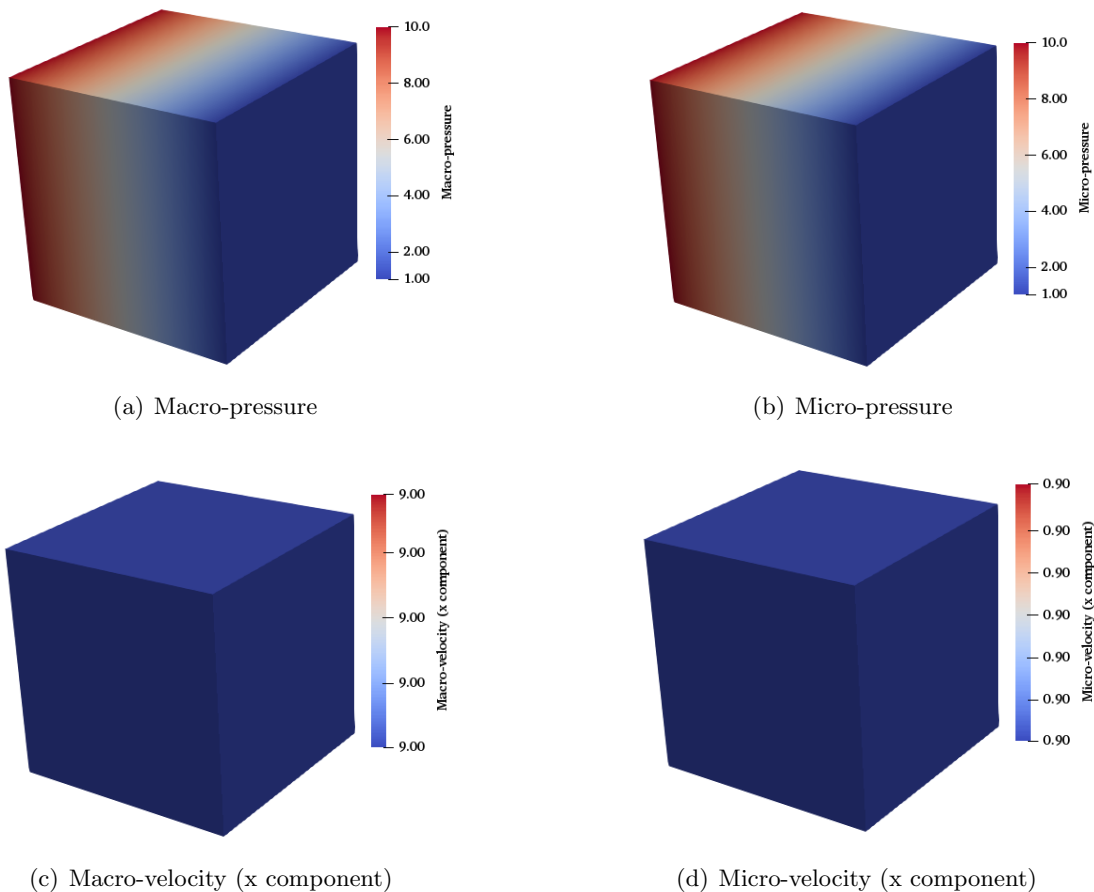


FIGURE 17. Non-constant Jacobian elements: Pressure and velocity contours are shown for Mesh #2 (Fig. 15(b)) with non-constant Jacobian elements. Pressures are varying linearly from the left face to the right one and velocities are constant throughout the domain as expected. These results show that the proposed mixed DG formulation is capable of providing accurate results using non-constant Jacobian elements.

computational domain is divided into four sub-regions I, II, III, and IV with abrupt changes in the permeability.

In this problem, elliptic singularities are observed near the injection and production wells which are located at the opposite corners of the diagonals (denoted by C_{inj} and C_{prod} , respectively). The normal component of velocity is prescribed to be zero on the entire boundary of the micro-pore network. In the macro-network, however, velocity at the injection and production wells is prescribed by applying a source/sink term while zero normal velocity is assumed on the rest of the boundary. It is worth mentioning that the prescribed source and sink strengths at injection and production wells are, respectively, equal to +1 and -1. However, instead of applying a pointwise sink/source at the location of wells, the normal component of velocity is applied along the external edges of the corner element in x - and y -directions with an equivalent distribution as shown in Fig. 22.

Table 6 provides the parameter values for this problem. The permeability parameters in sub-regions I and IV and the ones in sub-regions II and III are mutually equal. Herein, we assume that

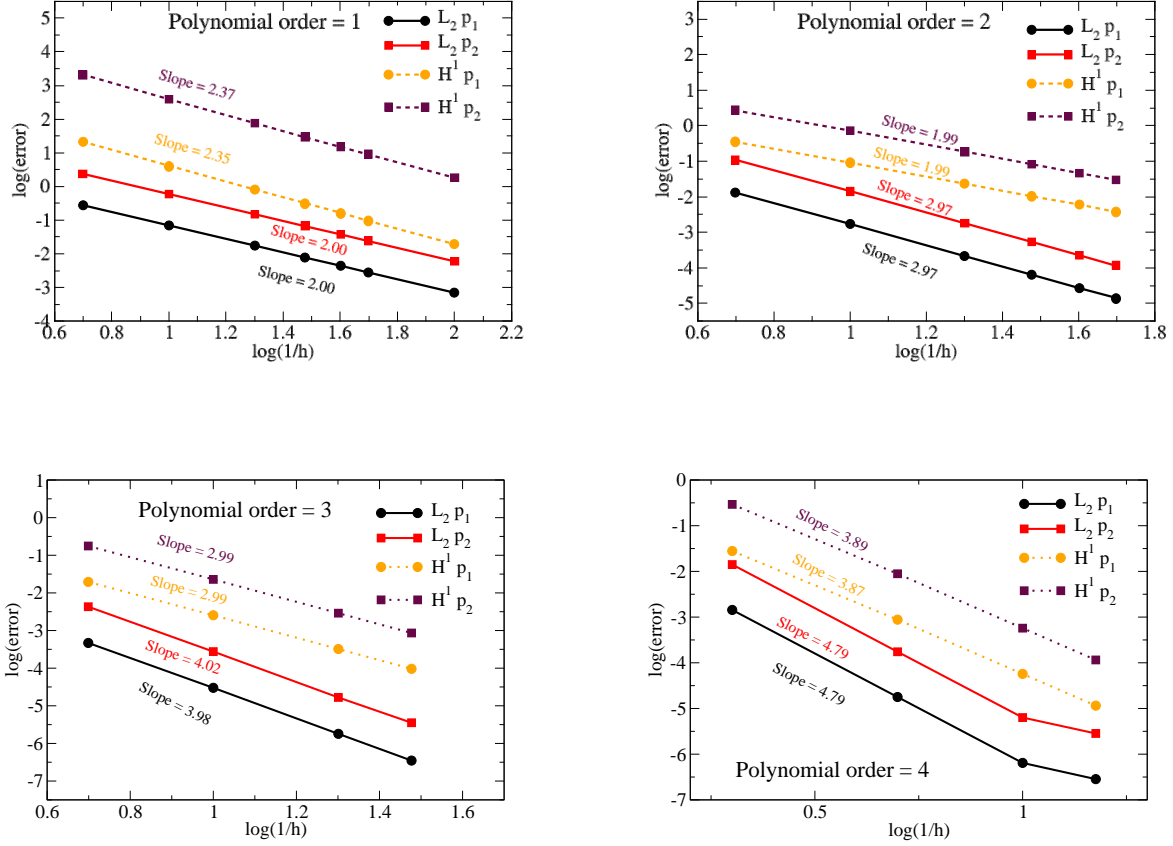


FIGURE 18. 2D numerical convergence analysis: This figure provides the convergence rates under h -refinement for various polynomial orders. The rate of convergence is polynomial, which is in accordance with the theory (viz. Corollary 4.7).

sub-regions I and IV are more permeable compared to sub-regions II and III with the following drag coefficients:

$$\begin{aligned} \left(\frac{\mu}{k_1}\right)_I &= \left(\frac{\mu}{k_1}\right)_{IV} = 1, & \left(\frac{\mu}{k_1}\right)_{II} &= \left(\frac{\mu}{k_1}\right)_{III} = 100, \\ \left(\frac{\mu}{k_2}\right)_I &= \left(\frac{\mu}{k_2}\right)_{IV} = 10, & \text{and } \left(\frac{\mu}{k_2}\right)_{II} &= \left(\frac{\mu}{k_2}\right)_{III} = 1000 \end{aligned} \quad (7.1)$$

Fig. 23 shows the macro- and micro pressure profiles for this problem. Steep gradients near the injection and production wells with no spurious oscillation in the pressure fields are observed under the proposed DG formulation which confirm the robustness of the numerical formulation. In order to further explore the effect of stabilization parameters on the solution profiles, this problem has been solved for different combinations of η_u and η_p as shown in **Fig. 24**. As can be seen, η_u and η_p have no noticeable effect on x-component of velocities under the DG formulation. However, spurious oscillations are observed under the CG formulation at the interface of sub-regions with

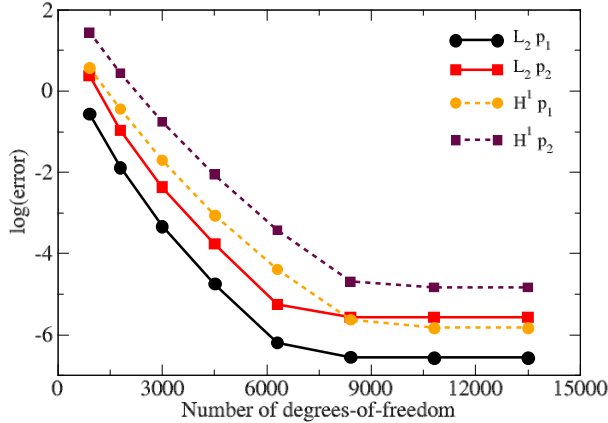


FIGURE 19. 2D numerical convergence analysis: This figure shows the results of numerical convergence under p -refinement for a fixed mesh size ($h = 0.2$). The number of degrees-of-freedom corresponds to $p = 1$ to 8. The rate of convergence is exponential, which is in accordance with the theory (viz. Corollary 4.7).

TABLE 5. Model parameters for 3D numerical convergence analysis.

Parameter	Value
$\gamma \mathbf{b}$	$\{0.0, 0.0, 0.0\}$
L_x	1.0
L_y	1.0
μ	1.0
β	1.0
k_1	1.0
k_2	0.1
η	$\sqrt{11} \simeq 3.3166$
η_u	100.0
η_p	0.0
$p_i^{\text{left}}, i = 1, 2$ $p_i^{\text{right}}, i = 1, 2$ $p_i^{\text{top}}, i = 1, 2$ $p_i^{\text{bottom}}, i = 1, 2$	Obtained by evaluating the analytical solution (equations (6.1) and (6.2)) on the respective boundaries.

different permeability values which implies that CG formulations fall short in capturing material discontinuities.

7.2. Element-wise mass balance. A DG method, when designed properly, can exhibit superior element-wise properties compared to its continuous counterpart. CG formulations may suffer from poor element-wise conservation; however, they satisfy a global mass balance [Hughes et al., 2000]. The importance of element-wise mass balance in subsurface modeling is discussed in [Turner et al., 2012], which is particularly true when the flow is coupled with transport and/or chemical reactions.

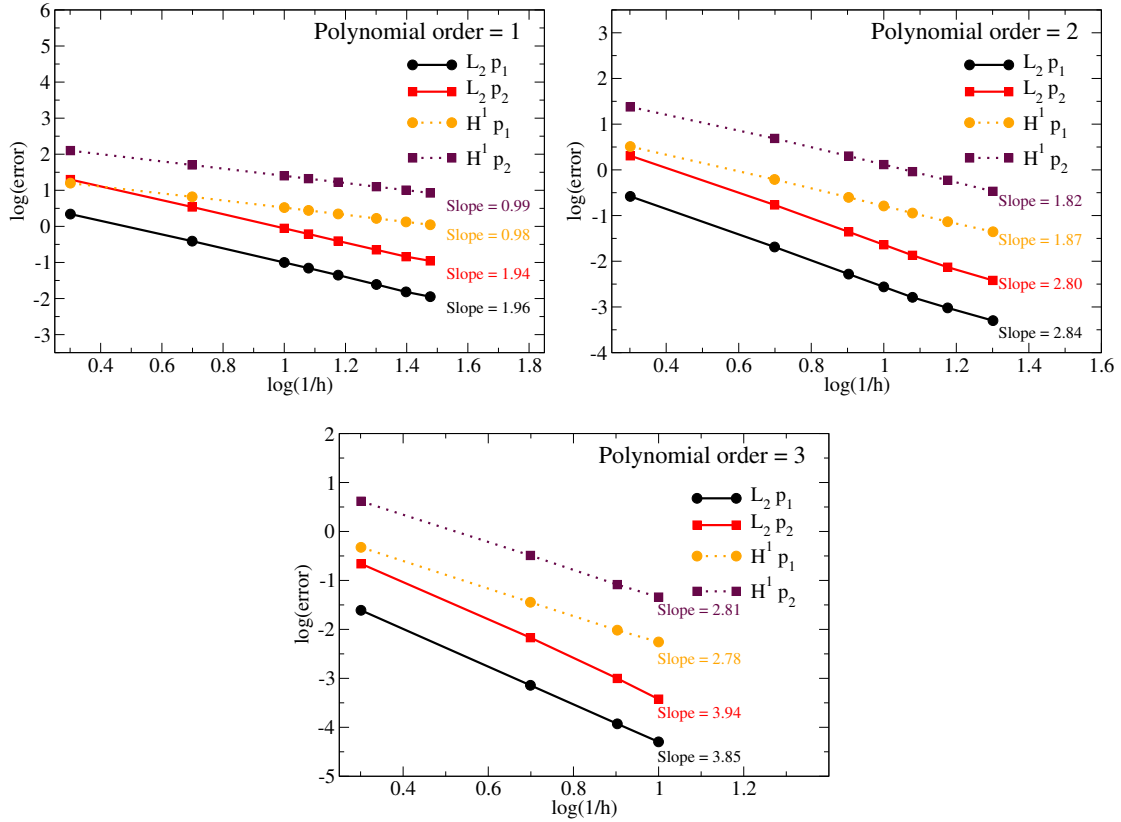


FIGURE 20. 3D numerical convergence analysis: This figure provides the convergence rates under h -refinement for various polynomial orders. The rate of convergence is polynomial, which is in accordance with the theory (viz. Corollary 4.7).

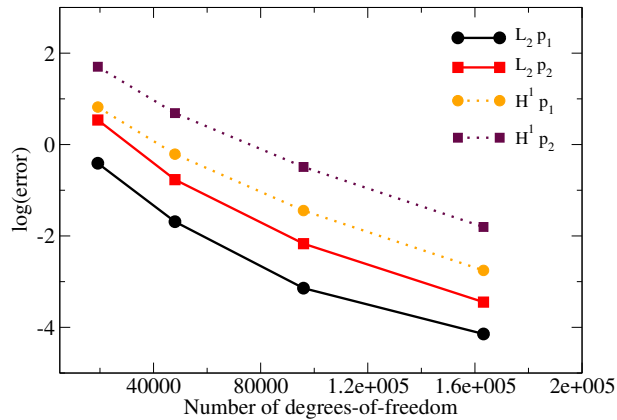


FIGURE 21. 3D numerical convergence analysis: This figure shows the results of numerical convergence under p -refinement for a fixed mesh size ($h = 0.2$). The number of degrees-of-freedom corresponds to $p = 1$ to 4. The rate of convergence is exponential, which is in accordance with the theory (viz. Corollary 4.7).

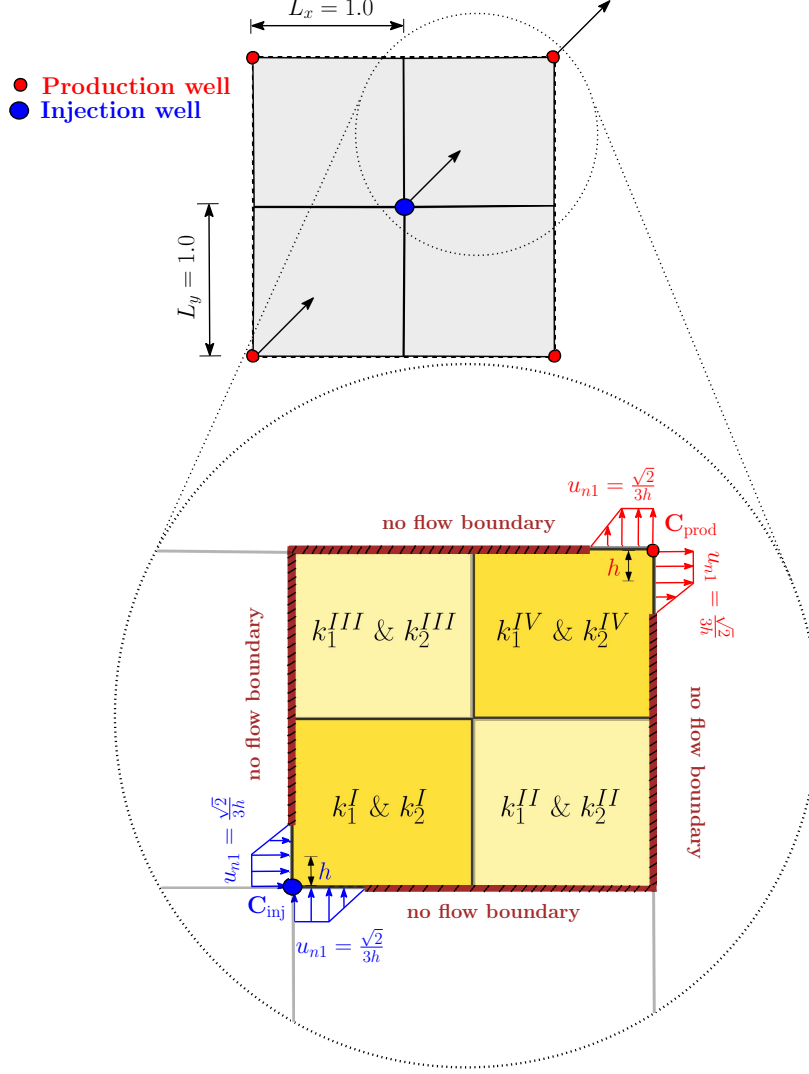


FIGURE 22. Quarter five-spot checkerboard problem: This figure shows the computational domain and boundary conditions for the quarter five-spot checkerboard problem. The heterogeneous domain is divided into four sub-regions with permeabilities shown in equation (7.1). The normal component of micro-velocity is equal to zero on the entire boundary. In the macro-network, however, source/sink strengths are prescribed in form of equivalent normal velocity distributions at the production (C_{prod}) and injection (C_{inj}) wells. On the rest of the boundary, the normal component of macro-velocity is assumed to be zero.

In this section, element-wise mass balance error is investigated under the proposed stabilized mixed DG formulation for the DPP model, and the results are compared with its continuous counterpart. In the context of DPP, the net rate of volumetric flux from both pore-networks can be obtained as follows for an element $\omega \in \mathcal{T}_h$:

$$m(\omega) := \int_{\partial\omega} (\mathbf{u}_1 + \mathbf{u}_2) \cdot \hat{\mathbf{n}} \, d\Gamma \quad (7.2)$$

TABLE 6. Model parameters for the quarter five-spot checkerboard problem.

Parameter	Value
$\gamma \mathbf{b}$	$\{0.0, 0.0\}$
L_x	1.0
L_y	1.0
μ	1.0
β	1.0
k_1, k_2	refer to Eqn. (7.1)
u_{n1}	0.0 On $\partial\Omega - \{C_{\text{prod}} \& C_{\text{inj}}\}$
u_{n2}	0.0 On $\partial\Omega$
source and sink strength	-1 at C_{prod} +1 at C_{inj}
η_u	0, 10, 100
η_p	0, 10, 100
h	structured T3 mesh of size 0.01 used

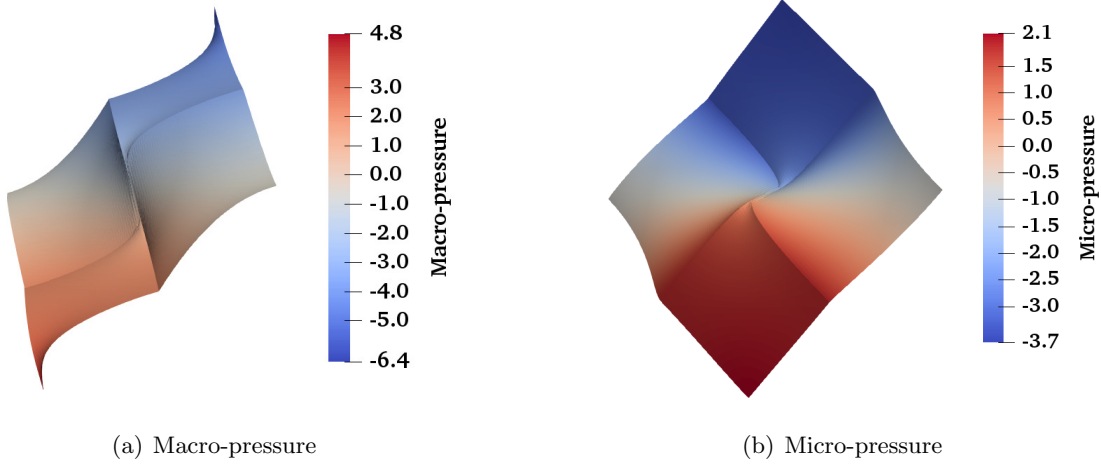


FIGURE 23. Quarter five-spot checkerboard problem: This figure shows that steep pressure gradients near the injection and production wells are correctly captured under the proposed DG formulation. However, no spurious oscillation are observed in the pressure fields which shows the robustness of our numerical formulation. These results are obtained for $\eta_u = \eta_p = 0$.

After calculation, this equation should result in a zero value. The maximum element-wise mass inflow/outflow flux can be obtained as follows:

$$m_{\max}^{\text{out}} := \max_{\omega \in \mathcal{T}_h} [\max[m(\omega), 0]] \quad (7.3a)$$

$$m_{\max}^{\text{in}} := \max_{\omega \in \mathcal{T}_h} [\max[-m(\omega), 0]] \quad (7.3b)$$

It should be noted that the definition of the local mass flux presented in equation (7.2) is different from the corresponding one under the Darcy equations. For the case of single porosity and under Darcy equations, the net flux is zero for the velocity. However, under the DPP model the net flux need not be zero for the individual velocities and it is shown to be zero for the summation of \mathbf{u}_1 and

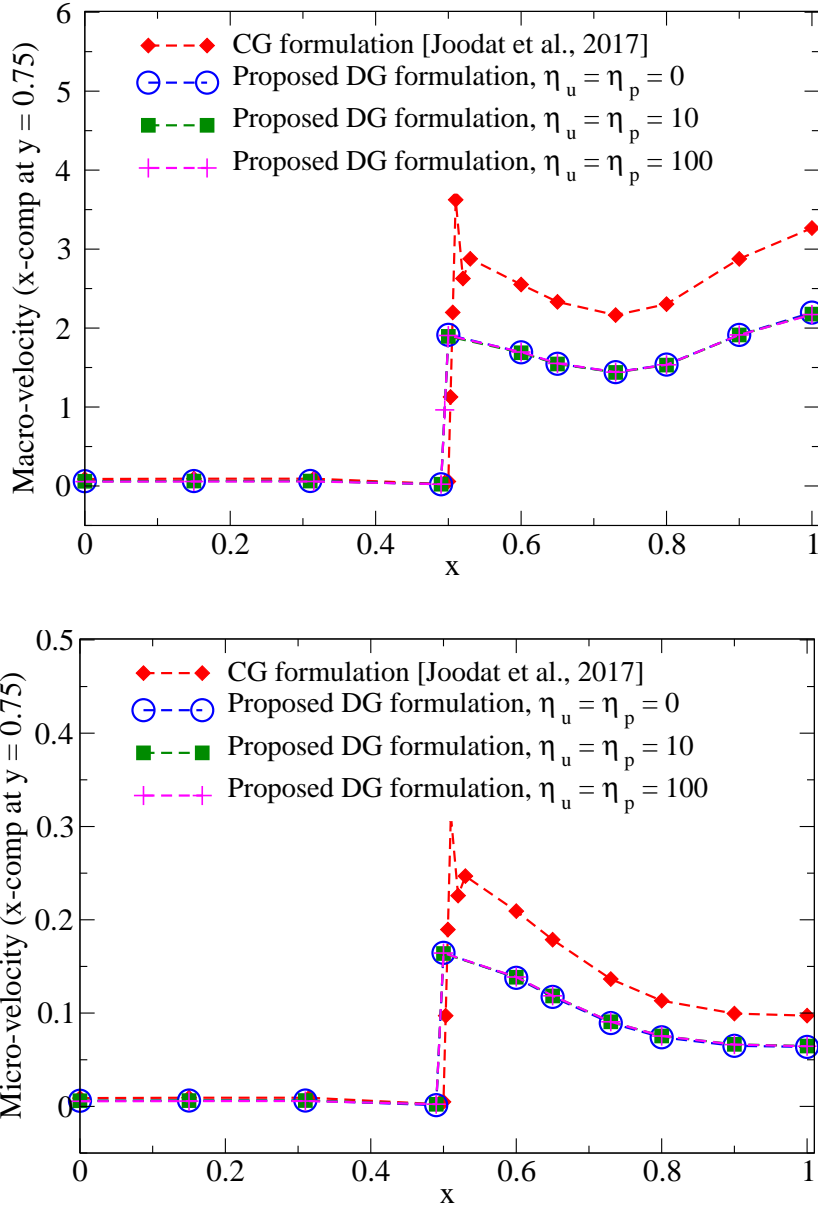


FIGURE 24. Quarter five-spot checkerboard problem: This figure compares the x-component of the macro-velocity (top) and micro-velocity (bottom) profiles under the CG formulation and the proposed DG formulation with different values of stabilization parameters η_u and η_p . As can be seen, under CG formulation, spurious oscillations are observed at the interface of sub-regions with different permeabilities. Moreover, η_u and η_p have no noticeable effect on solutions obtained under the DG formulation.

\mathbf{u}_2 . The domain is discretized with structured T3 mesh of size 0.2. We employ the same boundary value problem as stated in subsection 5.2.1 with parameter values provided in Table 2. Pressures are prescribed on the whole boundary in both pore-networks.

Comparisons of maximum local mass inflow/outflow with respect to different combinations of equal-order interpolation are illustrated in **Fig. 25** for both DG and CG formulations. **Fig. 26** shows the local mass balance error in each element for cubic equal-order polynomials. The error values obtained under CG and DG formulations suggest that the DG formulation returns smaller errors.

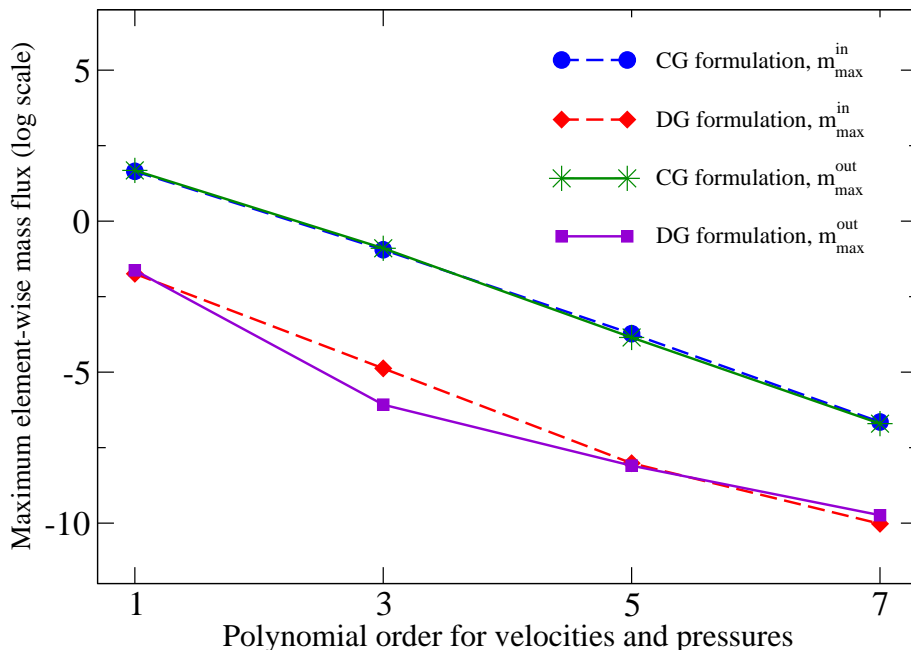


FIGURE 25. Element-wise mass balance: This figure shows the variation of the maximum element-wise inflow/outflow flux with interpolation polynomial orders.

8. COUPLED PROBLEM WITH HETEROGENEOUS MEDIUM PROPERTIES

In the previous sections, we used patch tests and canonical problems to demonstrate that the proposed stabilized mixed DG formulation can accurately capture the jumps in the solution fields across material interfaces. We will further illustrate the performance of this formulation using a representative problem pertaining to viscous fingering in heterogeneous porous media.

Viscous fingering is a coupled phenomenon which involves both flow and transport [Drazin, 2002]. In the flow of two immiscible fluids in a thin cell, typically called the Hele-Shaw cell, a more viscous fluid (with viscosity μ_H) is invaded by a less viscous one (with viscosity $\mu_L < \mu_H$), resulting in the creation of physical (displacement) instabilities [Homsy, 1987]. The classical viscous fingering in porous media with a single pore-network (i.e., under Darcy equations) has been studied by [Saffman and Taylor, 1958], and therefore, this instability is sometimes referred to as the Saffman-Taylor instability in the literature [Drazin, 2002]. Recently, [Joodat et al., 2018] have numerically shown that viscous-fingering-type instabilities can also occur in homogeneous porous media with

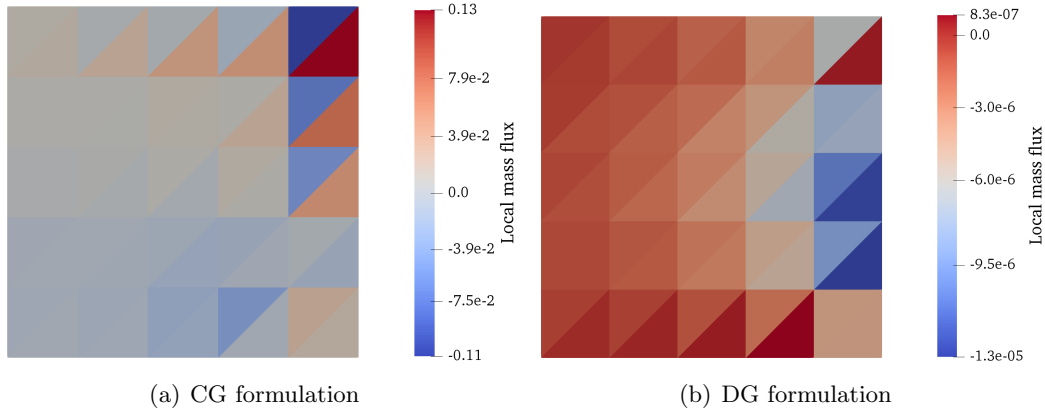


FIGURE 26. Element-wise mass balance: This figure shows the local mass balance error under both CG and DG formulations for cubic equal-order interpolation for all the field variables. As can be seen, the DG formulation returns smaller errors.

double pore-networks. They employed the continuous Galerkin (CG) formulation of the DPP model, as their studies were restricted to homogeneous porous media.

Herein, we will employ the proposed DG formulation to study the effect of *heterogeneity* on the appearance and growth of viscous-fingering-type physical instabilities in porous media with two pore-networks. The governing equations for this two-way coupled flow and transport problem consist of two parts. Flow under the DPP model is governed by equations (2.1a)–(2.1i) and the transient advection-diffusion problem is governed by the following set of equations:

$$\frac{\partial c(\mathbf{x}, t)}{\partial t} + \operatorname{div} [\mathbf{u}(\mathbf{x}, t)c(\mathbf{x}, t) - D(\mathbf{x}, t)\operatorname{grad}[c(\mathbf{x}, t)]] = f(\mathbf{x}, t) \quad \text{in } \Omega \times (0, T) \quad (8.1a)$$

$$c(\mathbf{x}, t) = c^p(\mathbf{x}, t) \quad \text{on } \Gamma^D \times (0, T) \quad (8.1b)$$

$$\hat{\mathbf{n}}(\mathbf{x}) \cdot (\mathbf{u}(\mathbf{x}, t)c(\mathbf{x}, t) - D(\mathbf{x}, t)\operatorname{grad}[c(\mathbf{x}, t)]) = q^p(\mathbf{x}, t) \quad \text{on } \Gamma^N \times (0, T) \quad (8.1c)$$

$$c(\mathbf{x}, t = 0) = c_0(\mathbf{x}) \quad \text{in } \Omega \quad (8.1d)$$

where $c(\mathbf{x}, t)$ denotes the concentration, $D(\mathbf{x}, t)$ is the diffusivity, and the advection velocity $\mathbf{u}(\mathbf{x}, t)$ is sum of the macro- and micro-velocity fields (which are obtained from the flow problem). That is,

$$\mathbf{u}(\mathbf{x}, t) = \mathbf{u}_1(\mathbf{x}, t) + \mathbf{u}_2(\mathbf{x}, t) \quad (8.2)$$

The concentration for the more viscous fluid is assumed to be zero and for the less viscous fluid is considered to be equal to 1. In order to complete the coupling of the flow and transport equations and upon introducing μ_0 as the base viscosity of the less viscous fluid and $R_c = \log(\mu_H/\mu_L)$ as the log-mobility ratio, the viscosity of the fluid is assumed to exponentially depend on the concentration of the diffusant as follows:

$$\mu(c(\mathbf{x}, t)) = \mu_0 \exp[R_c(1 - c(\mathbf{x}, t))] \quad (8.3)$$

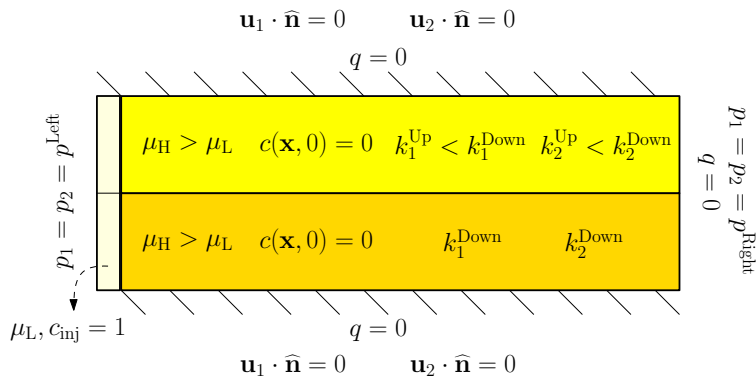


FIGURE 27. Coupled flow and transport problem: This figure shows the pictorial description of coupled flow-transport problem with heterogeneous medium properties along with initial and boundary conditions.

We consider a domain consisting of two horizontal layers with different permeabilities. The pictorial description of the problem is provided in **Fig. 27**. The values of macro- and micro-permeabilities in the bottom layer are assumed to be higher than those of the upper layer. Such heterogeneity in the permeability imposes a perturbation on the interface of the two fluids which causes the appearance of unstable finger-like patterns throughout the domain at the fluid-fluid interface. Moreover, a random function is used for defining the initial condition for the transport problem within the domain. Parameter values for this coupled flow and transport problem are provided in Table 7. For the advection-diffusion model given by equations (8.1a)–(8.1d), we have utilized Streamline Upwind Petrov-Galerkin (SUPG) formulation, as described in [Brooks and Hughes, 1982]. Also, see the computer code provided in Appendix A.

TABLE 7. Model parameters for coupled flow and transport problem in the heterogeneous domain.

Parameter	Value	Parameter	Value
$\gamma\mathbf{b}$	{0.0, 0.0}	k_2^{Down}	0.011
f	0.0	k_2^{Up}	0.009
L_x, L_y	1.0, 0.4	c_0	0.0
μ_0	1×10^{-3}	c_{inj}	1.0
R_c	3.0	p^{Left}	10.0
D	2×10^{-6}	p^{Right}	1.0
β	1.0	q	0.0
k_1^{Down}	1.1	Δt	5×10^{-5}
k_1^{Up}	0.9	T	1.5×10^{-3}
h	structured T3 mesh of size 0.01 used	η_u	0
		η_P	0

Fig. 28 shows the concentration profile at different time steps throughout the heterogeneous domain. The more viscous fluid is shown in dark blue and the less viscous fluid is shown in dark red. As can be seen, physical instabilities in form of separate finger-like intrusions are created at the fluid-fluid interface. These intrusions are similar to the viscous-fingering-type instabilities. At the early time steps, we have a larger number of fingers compared to the later time steps. These

smaller fingers merge and form fewer but much larger fingers as time goes by. It should be noted that finger-like physical instabilities grow at a higher rate in the bottom layer due to its higher permeability, as can be seen in **Fig. 28**. Moreover, at the later time steps, the fingers formed in the bottom layer tend to move towards the interface and enter the top layer. The proposed DG formulation eliminated the numerical instabilities (like Gibbs phenomenon and spurious node-to-node oscillations) but yet accurately captured the physical instabilities. It is worth mentioning that in our numerical simulations, the parameters η_u and η_p had no noticeable effect on the generation of fingers.

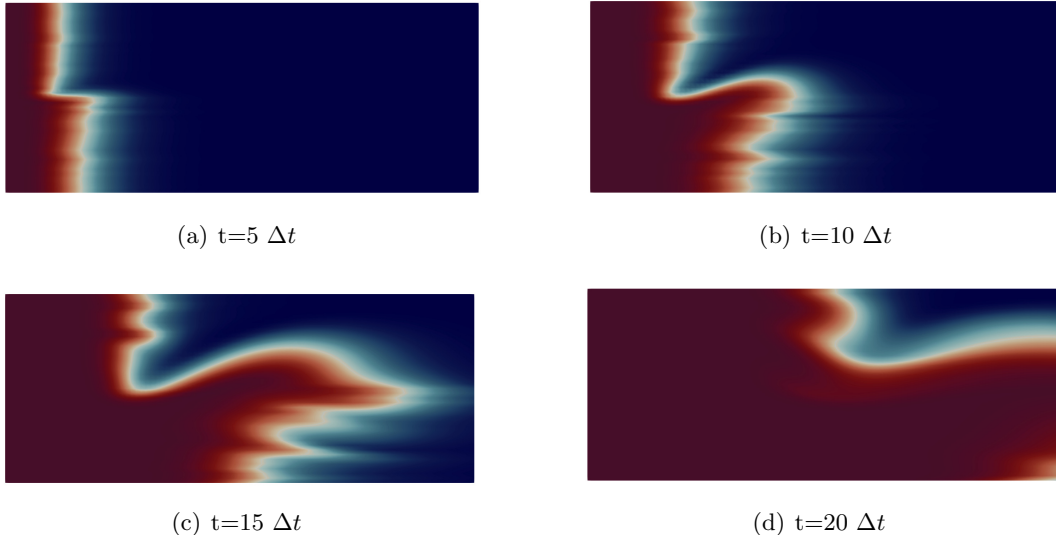


FIGURE 28. Coupled flow and transport problem: This figure illustrates that the proposed stabilized mixed DG formulation is capable of capturing well-known instabilities in fluid mechanics, similar to viscous-fingering instability, in a heterogeneous, layered porous domain with abrupt changes in permeabilities. Fingers are propagating at a higher rate in the bottom layer with higher macro- and micro-permeabilities. In our numerical simulations, the parameters η_u and η_p had no noticeable effect on the generation of fingers. We obtained similar results under $\eta_u = \eta_p = 10$ and $\eta_u = \eta_p = 100$; which are not shown here.

9. CONCLUDING REMARKS

A new stabilized mixed DG formulation has been presented for the DPP mathematical model, which describes the flow of a single-phase incompressible fluid through a porous medium with two dominant pore-networks. Some of the main findings of this paper on the *computational front* and the *nature of flow* through porous media with double pore-networks can be summarized as follows:

- (i) Arbitrary combinations of interpolation functions for the field variables are stable under the proposed DG formulation. Unlike the classical mixed DG formulation, which violates the LBB *inf-sup* stability condition under the equal-order interpolation for all the field variables, the proposed DG formulation circumvents the LBB condition. This implies that the proposed DG formulation does not suffer from node-to-node spurious oscillations when the computationally convenient equal-order interpolation for all the field variables is employed.

- (ii) Due to a careful selection of numerical fluxes, the proposed DG formulation does not suffer from the inherent instabilities that DG methods typically suffer from; for example, the Bassi-Rebay DG method.
- (iii) The stabilization terms inside the domain are of adjoint-type and residual-based, and the corresponding stabilization parameters do not contain any mesh-dependent parameters.
- (iv) The proposed stabilized formulation performs remarkably well, in comparison with its continuous counterpart, in the presence of heterogeneity in material properties. In other words, under the proposed DG formulation no unphysical numerical instabilities are generated at the vicinity of discontinuities in material properties due to Gibbs phenomenon.
- (v) The formulation passes patch tests, even on meshes with non-constant Jacobian elements, in 2D and 3D settings.
- (vi) The proposed DG formulation can support non-conforming discretization in form of non-conforming polynomial orders or non-conforming element refinement, thus allowing efficient h -, p -, and hp -adaptivities.
- (vii) A sensitivity study revealed the importance of η_u and η_p (i.e., jump terms with respect to the normal components of the velocities and pressures, respectively) to reduce the drift along the interior edges for the case of non-conforming polynomial orders.
- (viii) It is shown, theoretically, that the proposed formulation is convergent. The convergence rates obtained under both h - and p -refinement methods in several numerical experiments are in accordance with the theory.
- (ix) It is shown that the proposed DG formulation can be employed to solve coupled flow-transport problems in porous media with double pore-networks. In particular, the effect of heterogeneity of medium properties is studied on the appearance and growth of fingers under viscous-fingering-type instability. The proposed formulation is capable of suppressing the non-physical numerical instabilities (like Gibbs phenomenon and spurious node-to-node oscillations), yet capturing the underlying physical ones.

Appendix A. COMPUTER IMPLEMENTATION

The numerical results pertaining to the non-conforming discretization (Section 5.2) and non-constant Jacobian elements (Section 5.3), have been obtained using COMSOL Java API [COM, 2012]. The numerical simulations for the 3D numerical convergence analysis (Section 6.2) and the coupled problem (Section 8) were carried out using the Firedrake Project [Luporini et al., 2015; Rathgeber et al., 2017]. All the remaining numerical results were generated using the FEniCS Project [Alnæs et al., 2015; Logg et al., 2012a].

The FEniCS and Firedrake Projects are built upon several scientific packages and provide automated frameworks to solve partial differential equations in serial and parallel environments. Both provide an easy-to-use Python-based interface to develop computer codes, to access the scientific packages on which they are built upon, and to generate the output in various formats which are compatible with popular visualization software packages such as ParaView [Ayachit, 2015] and VisIt [Childs et al., 2012]. Under both these projects, mesh generation can be performed either within the code or using the third party mesh generators such as GMSH [Geuzaine and Remacle, 2009].

Among the various components available in FEniCS, we have used the Unified Form Language (UFL) [Alnæs et al., 2014] and the DOLFIN library [Logg and Wells, 2010; Logg et al., 2012b] in our implementations. The former enables the user to declare the finite element discretization of

variational forms and the latter is used for the automated assembly of the finite element discrete formulations. The Firedrake Project employs the UFL from the FEniCS Project. However, the main difference between the FEniCS and Firedrake Projects is that all data structures, linear solvers and non-linear solvers for the former are provided by DOLFIN library and for the latter are provided entirely by the PETSc library [Balay et al., 2016]. Another notable difference is that the FEniCS Project offers only simplicial element (e.g., triangular and tetrahedron elements), whereas the Firedrake Project offers non-simplicial elements in addition to the simplicial ones.

In our numerical simulations, MUMPS [Amestoy et al., 2001] direct solver and the sparse LU decomposition direct solver from the UMFPACK [Davis, 2004] were, respectively, employed with default settings under the COMSOL Java API and the FEniCS Project. The GMRES iterative solver with “bjacobi” preconditioner and the relative convergence tolerance of 10^{-7} was employed under the Firedrake Project.

Below, we have provided a Firedrake-based computer code, which can be used to generate the results for the coupled problem, which is discussed in Section 8.

LISTING 1. Firedrake code for solving the coupled problem in the heterogeneous porous medium

```

1 from firedrake import *
2 import numpy
3 import random
4 try:
5     import matplotlib.pyplot as plt
6 except:
7     warning("Matplotlib not imported")
8
9 #== Create mesh ==
10 nx, ny = 100, 40
11 Lx, Ly = 1.0, 0.4
12 mesh = RectangleMesh(nx,ny,Lx,Ly)
13
14 #== Function spaces ==
15 #---Double porosity/permeability flow problem---
16 velSpace = VectorFunctionSpace(mesh, "DG", 2)
17 pSpace = FunctionSpace(mesh, "DG", 2)
18 wSpace = MixedFunctionSpace([velSpace, pSpace, velSpace, pSpace])
19
20 #---Advection-diffusion problem---
21 uSpace = FunctionSpace(mesh, "CG", 1)
22
23 #---Permeability---
24 kSpace = FunctionSpace(mesh, "DG", 0)
25
26 #== Material properties and parameters ==
27 mu0, Rc, D = Constant(1e-3), Constant(3.0), Constant(2e-6)
28 k1.0 = 1.1
29 k1.1 = 0.9
30 tol = 1E-14
31
32 class myk1(Expression): #Macro-permeability
33     def eval(self, values, x):

```

```

34     if x[1] < Ly/2 + tol:
35         values[0] = k1_0
36     else:
37         values[0] = k1_1
38
39 k1 = interpolate(myk1(),kSpace)
40
41 k2_0 = 0.01 * 1.1
42 k2_1 = 0.01 * 0.9
43
44 class myk2(Expression): #Micro-permeability
45     def eval(self, values, x):
46         if x[1] < Ly/2 + tol:
47             values[0] = k2_0
48         else:
49             values[0] = k2_1
50
51 k2 = interpolate(myk2(),kSpace)
52
53 #---Drag coefficients---
54
55 def alpha1(c):
56     return mu0 * exp(Rc * (1.0 - c))/k1
57
58 def invalpha1(c):
59     return 1/alpha1(c)
60
61 def alpha2(c):
62     return mu0 * exp(Rc * (1.0 - c))/k2
63
64 def invalpha2(c):
65     return 1/alpha2(c)
66
67 #== Boundary and initial conditions ==
68 v_topbottom = Constant(0.0)
69 p_L = Constant(10.0)
70 p_R = Constant(1.0)
71 c_inj = Constant(1.0)
72
73 #== Perturbation function for initial concentration ==
74 #---Needed to trigger the instability---
75 class c_0(Expression):
76     def eval(self, values, x):
77         if x[0] < 0.010*Lx:
78             values[0] = abs(.10*exp(-x[0]*x[0]) * random.random())
79         else:
80             values[0] = 0.0
81
82 #== Define trial and test functions ==
83 #---DPP flow problem---
84 (v1,p1,v2,p2) = TrialFunctions(wSpace)
85 (w1,q1,w2,q2) = TestFunctions(wSpace)

```

```

86 DPP_solution = Function(wSpace)
87
88 #---AD problem---
89 c1 = TrialFunction(uSpace)
90 u = TestFunction(uSpace)
91 conc = Function(uSpace)
92 conc_k = interpolate(c_0(),uSpace)
93
94 #== Time parameters ==
95 T = 0.0015 # Total simulation time
96 dt = 0.00005 # Time step
97
98 #== Boundary conditions ==
99 #---DPP velocity BCs---
100 bcDPP = []
101
102 #---AD concentration BCs---
103 bcleft_c = DirichletBC(uSpace,c_inj,1,method = "geometric")
104
105 bcAD = [bcleft_c]
106
107 #== Define source terms ==
108 #---DPP model---
109 rhob1, rhob2 = Constant((0.0,0.0)), Constant((0.0,0.0))
110
111 #---AD problem---
112 f = Constant(0.0)
113
114 #== Normal vectors and mesh size ==
115 n = FacetNormal(mesh)
116 h = CellSize(mesh)
117 h_avg = (h('+') + h('-'))/2
118
119 #== Penalty parameters ==
120 eta_p, eta_u = Constant(0.0), Constant(0.0)
121
122 #== Define variational forms ==
123
124 #---DPP stabilized mixed DG formulation---
125 aDPP = dot(w1, alpha1(conc_k) * v1) * dx + \
126         dot(w2, alpha2(conc_k) * v2) * dx - \
127         div(w1) * p1 * dx - \
128         div(w2) * p2 * dx + \
129         q1 * div(v1) * dx + \
130         q2 * div(v2) * dx + \
131         q1 * (p1 - p2) * dx - \
132         q2 * (p1 - p2) * dx + \
133         jump(w1,n) * avg(p1) * dS + \
134         jump(w2,n) * avg(p2) * dS - \
135         avg(q1) * jump(v1,n) * dS - \
136         avg(q2) * jump(v2,n) * dS + \
137         dot(w1,n) * p1 * ds(3) + \

```

```

138 dot(w2,n) * p2 * ds(3) -\
139 q1 * dot(v1,n) * ds(3) -\
140 q2 * dot(v2,n) * ds(3) +\
141 dot(w1,n) * p1 * ds(4) +\
142 dot(w2,n) * p2 * ds(4) -\
143 q1 * dot(v1,n) * ds(4) -\
144 q2 * dot(v2,n) * ds(4) -\
145 0.5 * dot( alpha1(conc_k) * w1 - grad(q1), \
146         invalpha1(conc_k) * (alpha1(conc_k) * v1 + grad(p1)) ) * dx -\
147 0.5 * dot( alpha2(conc_k) * w2 - grad(q2), \
148         invalpha2(conc_k) * (alpha2(conc_k) * v2 + grad(p2)) ) * dx +\
149 (eta_u * h_avg) * avg(alpha1(conc_k)) * (jump(v1,n) * jump(w1,n)) * dS +\
150 (eta_u * h_avg) * avg(alpha2(conc_k)) * (jump(v2,n) * jump(w2,n)) * dS +\
151 (eta_p / h_avg) * avg(1 / alpha1(conc_k)) * dot(jump(q1,n), jump(p1,n)) * dS +\
152 (eta_p / h_avg) * avg(1 / alpha2(conc_k)) * dot(jump(q2,n), jump(p2,n)) * dS
153
154 LDPP = dot(w1,rhob1) * dx +\
155 dot(w2,rhob2) * dx -\
156 dot(w1,n) * p_L * ds(1) -\
157 dot(w2,n) * p_L * ds(1) -\
158 dot(w1,n) * p_R * ds(2) -\
159 dot(w2,n) * p_R * ds(2) -\
160 0.5 * dot( alpha1(conc_k) * w1 - grad(q1), \
161         invalpha1(conc_k) * rhob1 ) * dx -\
162 0.5 * dot( alpha2(conc_k) * w2 - grad(q2), \
163         invalpha2(conc_k) * rhob2 ) * dx
164
165
166 #---AD formulation with SUPG Stabilization---
167 vnorm = sqrt(dot((DPP_solution.sub(0)+DPP_solution.sub(2)),\
168         (DPP_solution.sub(0)+DPP_solution.sub(2))))
169
170 tau = h/(2*vnorm)*dot((DPP_solution.sub(0)+DPP_solution.sub(2)),\
171         grad(u))
172
173 a_r = tau*(c1 + dt*(dot((DPP_solution.sub(0)+DPP_solution.sub(2)),\
174         grad(c1)) - div(D*grad(c1))))*dx
175
176 L_r = tau*(conc_k + dt*f)*dx
177
178 #---Weak form (GL + SUPG)---
179 aAD = a_r + u*c1*dx + dt*(u*dot((DPP_solution.sub(0)+DPP_solution.sub(2)),\
180         grad(c1))*dx + dot(grad(u),D*grad(c1))*dx)
181
182 LAD = L_r + u*conc_k*dx + dt*u*f*dx
183
184 #---Create files for storing solution---
185 cfile = File("Concentration.pvd")
186 v1file = File("Macro.Velocity.pvd")
187 p1file = File("Macro.Pressure.pvd")
188 v2file = File("Micro.Velocity.pvd")
189 p2file = File("Micro.Pressure.pvd")

```

```

190
191 #== Solver for flow problem ==
192 solver_parameters = { # Default solver — medium sized problems
193     'ksp_type': 'gmres',
194     'pc_type': 'bjacobi',
195     'mat_type': 'aij',
196     'ksp_rtol': 1e-7,
197     'ksp_monitor': True
198 }
199
200 problem_flow = LinearVariationalProblem(aDPP, LDPP, DPP_solution, bcs=bcDPP,
201     constant_jacobian=False)
202 solver_flow = LinearVariationalSolver(problem_flow, options_prefix="flow.",
203     solver_parameters=solver_parameters)
204
205 #== March the solution over time ==
206 t = dt
207 while t ≤ T:
208     print '===== '
209     print '           time =', t
210     print '===== '
211     c_0.t = t
212
213     #—Compute DPP model—
214     solver_flow.solve()
215
216     #—Compute AD problem—
217     solve(aAD == LAD, conc, bcs=bcAD)
218     conc.k.assign(conc) # update for next iteration
219
220     #—Dump solutions for each time step—
221     cfile.write(conc, time = t)
222     v1file.write(DPP_solution.sub(0), time = t)
223     p1file.write(DPP_solution.sub(1), time = t)
224     v2file.write(DPP_solution.sub(2), time = t)
225     p2file.write(DPP_solution.sub(3), time = t)
226     t += dt
227
228 print "total time = ", t
229
230 v1sol, p1sol, v2sol, p2sol = DPP_solution.split()
231
232 #== Dump solution fields to file in VTK format ==
233 file = File("Concentration.pvd")
234 file.write(conc)
235
236 file = File('Macro.Velocity.pvd')
237 file.write(v1sol)
238
239 file = File('Macro.Pressure.pvd')
240 file.write(p1sol)
241

```



```

242 file = File('Micro_Velocity.pvd')
243 file.write(v2sol)
244
245 file = File('Micro_Pressure.pvd')
246 file.write(p2sol1)

```

References

- COMSOL Java API Reference Guide, Version 4.3.* COMSOL, Inc., Burlington, Massachusetts, www.comsol.com, 2012.
- R. Abedi, B. Petracovici, and R. B. Haber. A space–time discontinuous Galerkin method for linearized elastodynamics with element-wise momentum balance. *Computer Methods in Applied Mechanics and Engineering*, 195(25-28):3247–3273, 2006.
- M. Ainsworth and B. Senior. Aspects of an adaptive *hp*-finite element method: Adaptive strategy, conforming approximation and efficient solvers. *Computer Methods in Applied Mechanics and Engineering*, 150:65–87, 1997.
- M. Alnæs, J. Blechta, J. Hake, A. Johansson, B. Kehlet, A. Logg, C. Richardson, J. Ring, M. E. Rognes, and G. N. Wells. The FEniCC project version 1.5. *Archive of Numerical Software*, 3: 9–23, 2015.
- M. S. Alnæs, A. Logg, K. B. Ølgaard, M. E. Rognes, and G. N. Wells. Unified form language: A domain-specific language for weak formulations of partial differential equations. *ACM Transactions on Mathematical Software*, 40:9, 2014.
- P. R. Amestoy, I. S. Duff, J. Koster, and J. Y. L’Excellent. A fully asynchronous multifrontal solver using distributed dynamic scheduling. *SIAM Journal on Matrix Analysis and Applications*, 23: 15–41, 2001.
- D. N. Arnold. An interior penalty finite element method with discontinuous elements. *SIAM Journal on Numerical Analysis*, 19:742–760, 1982.
- D. N. Arnold, F. Brezzi, B. Cockburn, and L. D. Marini. Unified analysis of discontinuous Galerkin methods for elliptic problems. *SIAM Journal on Numerical Analysis*, 39:1749–1779, 2002.
- U. Ayachit. *The ParaView Guide: A Parallel Visualization Application*. Kitware, 2015. ISBN 978-1930934306.
- I. Babuška and M. R. Dorr. Error estimates for the combined *h* and *p* versions of the finite element method. *Numerische Mathematik*, 37:257–277, 1981.
- I. Babuška and T. Strouboulis. *The Finite Element Method and Its Reliability*. Oxford University Press, 2001.
- S. Badia and R. Codina. Stabilized continuous and discontinuous Galerkin techniques for Darcy flow. *Computer Methods in Applied Mechanics and Engineering*, 199:1654–1667, 2010.
- S. Balay, S. Abhyankar, M. F. Adams, J. Brown, P. Brune, K. Buschelman, L. Dalcin, V. Eijkhout, W. D. Gropp, D. Kaushik, M. G. Knepley, L. C. McInnes, K. Rupp, B. F. Smith, S. Zampini, H. Zhang, and H. Zhang. PETSc users manual. Technical Report ANL-95/11 - Revision 3.7, Argonne National Laboratory, 2016.
- R. E. Bank, A. H. Sherman, and A. Weiser. Some refinement algorithms and data structures for regular local mesh refinement. *Scientific Computing, Applications of Mathematics and Computing to the Physical Sciences*, 1:3–17, 1983.

- T. P. Barrios and R. Bustinza. An augmented discontinuous Galerkin method for elliptic problems. *Comptes Rendus Mathematique*, 344:53–58, 2007.
- F. Bassi and S. Rebay. A high-order accurate discontinuous finite element method for the numerical solution of the compressible Navier–Stokes equations. *Journal of Computational Physics*, 131:267–279, 1997.
- D. Braess. *Finite Elements: Theory, Fast Solvers, and Applications in Solid Mechanics*. Cambridge University Press, 2007.
- S. C. Brenner and L. R. Scott. *The Mathematical Theory of Finite Element Methods*. Springer-Verlag, New York, 1994.
- F. Brezzi and M. Fortin. *Mixed and Hybrid Finite Element Methods, volume 15 of Springer series in computational mathematics*. Springer-Verlag, New York, 1991.
- F. Brezzi, J. Douglas, and L. D. Marini. Two families of mixed elements for second order elliptic problems. *Numerische Mathematik*, 47:217–235, 1985.
- F. Brezzi, J. Douglas, M. Fortin, and L. D. Marini. Efficient rectangular mixed finite elements in two and three space variables. *Mathematical Modelling and Numerical Analysis*, 21:581–604, 1987.
- F. Brezzi, L. D. Marini, and E. Süli. Discontinuous Galerkin methods for first-order hyperbolic problems. *Mathematical Models and Methods in Applied Sciences*, 14:1893–1903, 2004.
- F. Brezzi, T. J. R. Hughes, L. D. Marini, and A. Masud. Mixed discontinuous Galerkin method for Darcy flow. *SIAM Journal of Scientific Computing*, 22:119–145, 2005.
- A. N. Brooks and T. J. R. Hughes. Streamline upwind/Petrov-Galerkin formulations for convection dominated flows with particular emphasis on the incompressible Navier-Stokes equations. *Computer methods in applied mechanics and engineering*, 32:199–259, 1982.
- C. Burstedde, O. Ghattas, M. Gurnis, G. Stadler, E. Tan, T. Tu, L. C. Wilcox, and H. Zhong. Scalable adaptive mantle convection simulation on petascale supercomputers. In *Proceedings of the 2008 ACM/IEEE conference on Supercomputing*, page 62. IEEE Press, 2008.
- N. Canouet, L. Fezoui, and S. Piperno. Discontinuous Galerkin time-domain solution of Maxwell’s equations on locally-refined nonconforming Cartesian grids. *COMPEL-The International Journal for Computation and Mathematics in Electrical and Electronic Engineering*, 24:1381–1401, 2005.
- P. Castillo, B. Cockburn, I. Perugia, and D. Schötzau. An a priori error analysis of the local discontinuous galerkin method for elliptic problems. *SIAM Journal on Numerical Analysis*, 38(5):1676–1706, 2000.
- H. Childs, E. Brugger, B. Whitlock, J. Meredith, S. Ahern, D. Pugmire, K. Biagas, M. Miller, C. Harrison, G. H. Weber, H. Krishnan, T. Fogal, A. Sanderson, C. Garth, E. W. Bethel, D. Camp, O. Rübel, M. Durant, J. M. Favre, and P. Navrátil. VisIt: An End-User Tool For Visualizing and Analyzing Very Large Data. In *High Performance Visualization—Enabling Extreme-Scale Scientific Insight*, pages 357–372. 2012.
- B. Cockburn. Discontinuous Galerkin methods. *Journal of Applied Mathematics and Mechanics/Zeitschrift für Angewandte Mathematik und Mechanik*, 83:731–754, 2003.
- B. Cockburn and C. Shu. Runge–kutta discontinuous galerkin methods for convection-dominated problems. *Journal of Scientific Computing*, 16(3):173–261, 2001.
- B. Cockburn, J. Gopalakrishnan, and R. Lazarov. Unified hybridization of discontinuous galerkin, mixed, and continuous galerkin methods for second order elliptic problems. *SIAM Journal on Numerical Analysis*, 47(2):1319–1365, 2009a.

- B. Cockburn, J. Guzmán, and H. Wang. Superconvergent discontinuous Galerkin methods for second-order elliptic problems. *Mathematics of Computation*, 78:1–24, 2009b.
- M. Crouzeix and P.-A. Raviart. Conforming and nonconforming finite element methods for solving the stationary stokes equations i. *Revue française d’automatique informatique recherche opérationnelle. Mathématique*, 7(R3):33–75, 1973.
- T. A. Davis. Algorithm 832: UMFPACK V4. 3—an unsymmetric-pattern multifrontal method. *ACM Transactions on Mathematical Software (TOMS)*, 30:196–199, 2004.
- V. Dolejší and M. Feistauer. *Discontinuous Galerkin Method: Analysis and Applications to Compressible Flow*. Springer, 2015.
- J. Douglas and T. Dupont. Interior penalty procedures for elliptic and parabolic Galerkin methods. *Computing Methods in Applied Sciences*, pages 207–216, 1976.
- P. G. Drazin. *Introduction to Hydrodynamic Stability*. Cambridge University Press, Cambridge, U.K., 2002.
- L. C. Evans. *Partial Differential Equations*. American Mathematical Society, Providence, Rhode Island, 1998.
- J. Foster and F. B. Richards. The Gibbs phenomenon for piecewise-linear approximation. *The American Mathematical Monthly*, 98(1):47–49, 1991.
- T. P. Fries, A. Byfut, A. Alizada, K. W. Cheng, and A. Schröder. Hanging nodes and XFEM. *International Journal for Numerical Methods in Engineering*, 86:404–430, 2011.
- C. Geuzaine and J. F. Remacle. Gmsh: a three-dimensional finite element mesh generator with built-in pre- and post-processing facilities. *International Journal for Numerical Methods in Engineering*, 79:1309–1331, 2009.
- J. W. Gibbs. Fourier’s series. *Nature*, 59(1522):200, 1898.
- J. W. Gibbs. Fourier’s series. *Nature*, 59(1539):606, 1899.
- A. K. Gupta. A finite element for transition from a fine to a coarse grid. *International Journal for Numerical Methods in Engineering*, 12:35–45, 1978.
- S. Güzey, B. Cockburn, and H. K. Stolarski. The embedded discontinuous galerkin method: application to linear shell problems. *International Journal for Numerical Methods in Engineering*, 70(7):757–790, 2007.
- R. Hartmann and P. Houston. Adaptive discontinuous Galerkin finite element methods for the compressible Euler equations. *Journal of Computational Physics*, 183:508–532, 2002.
- J. S. Hesthaven and T. Warburton. High-order nodal discontinuous Galerkin methods for the Maxwell eigenvalue problem. *Philosophical Transactions of the Royal Society of London A: Mathematical, Physical and Engineering Sciences*, 362:493–524, 2004.
- J. S. Hesthaven and T. Warburton. *Nodal Discontinuous Galerkin Methods: Algorithms, Analysis, and Applications*. Springer Science & Business Media, 2007.
- G. M. Homsy. Viscous fingering in porous media. *Annual Review of Fluid Mechanics*, 19:271–311, 1987.
- T. J. R. Hughes. *The Finite Element Method: Linear Static and Dynamic Finite Element Analysis*. Dover Publications, Inc., New York, 2012.
- T. J. R. Hughes, G. Engel, L. Mazzei, and M. G. Larson. The continuous Galerkin method is locally conservative. *Journal of Computational Physics*, 163:467–488, 2000.
- T. J. R. Hughes, A. Masud, and J. Wan. A stabilized mixed discontinuous Galerkin method for Darcy flow. *Computer Methods in Applied Mechanics and Engineering*, 195:3347–3381, 2006.

- S. H. S. Joodat, K. B. Nakshatrala, and R. Ballarini. Modeling flow in porous media with double porosity/permeability: A stabilized mixed formulation, error analysis, and numerical solutions. *Computer Methods in Applied Mechanics and Engineering*, 337:632–676, 2018.
- G. Karniadakis and S. Sherwin. *Spectral/hp Element Methods for Computational Fluid Dynamics*. Oxford University Press, New York, 2013.
- M. A. Kopera and G. X. Giraldo. Analysis of adaptive mesh refinement for IMEX discontinuous Galerkin solutions of the compressible Euler equations with application to atmospheric simulations. *Journal of Computational Physics*, 275:92–117, 2014.
- D. V. Kulkarni, D. V. Rovas, and D. A. Tortorelli. Discontinuous Galerkin framework for adaptive solution of parabolic problems. *International Journal for Numerical Methods in Engineering*, 70:1–24, 2007.
- J. Li and B. Rivière. Numerical solutions of the incompressible miscible displacement equations in heterogeneous media. *Computer Methods in Applied Mechanics and Engineering*, 292:107–121, 2015.
- J. Li and B. Rivière. Numerical modeling of miscible viscous fingering instabilities by high-order methods. *Transport in Porous Media*, 113:607–628, 2016.
- J. L. Lions. Problemes aux limites non homogenesa données irrégulieres: Une méthode d’approximation. *Numerical Analysis of Partial Differential Equations (CIME 2 Ciclo, Ispra, 1967)*, Edizioni Cremonese, Rome, pages 283–292, 1968.
- A. Logg and G. N. Wells. DOLFIN: Automated finite element computing. *ACM Transactions on Mathematical Software (TOMS)*, 37:20, 2010.
- A. Logg, K. A. Mardal, and G. N. Wells. *Automated solution of differential equations by the finite element method: The FEniCS book*, volume 84. Springer Science & Business Media, 2012a.
- A. Logg, G. N. Wells, and J. Hake. DOLFIN: A C++/Python finite element library. In *Automated Solution of Differential Equations by the Finite Element Method*, pages 173–225. Springer, 2012b.
- F. Luporini, A. L. Varbanescu, F. Rathgeber, G. T. Bercea, J. Ramanujam, D. A. Ham, and P. H. J. Kelly. Cross-loop optimization of arithmetic intensity for finite element local assembly. *ACM Transactions on Architecture and Code Optimization (TACO)*, 11:57, 2015.
- D. J. Morton, J. M. Tyler, and J. R. Dorroh. A new 3D finite element for adaptive h -refinement in 1-irregular meshes. *International Journal for Numerical Methods in Engineering*, 38:3989–4008, 1995.
- K. B. Nakshatrala, S. H. S. Joodat, and R. Ballarini. Modeling flow in porous media with double porosity/permeability: Mathematical model, properties, and analytical solutions. *Journal of Applied Mechanics*, 2018. Available on arXiv:1605.07658.
- P. B. Nakshatrala, K. B. Nakshatrala, and D. A. Tortorelli. A time-staggered partitioned coupling algorithm for transient heat conduction. *International Journal for Numerical Methods in Engineering*, 78(12):1387–1406, 2009.
- J.-C. Nédélec. Mixed finite elements in \mathbb{R}^3 . *Numerische Mathematik*, 35(3):315–341, 1980.
- J. Nitsche. Über ein Variationsprinzip zur Lösung von Dirichlet-Problemen bei Verwendung von Teilräumen, die keinen Randbedingungen unterworfen sind. In *Abhandlungen aus dem mathematischen Seminar der Universität Hamburg*, volume 36, pages 9–15. Springer, 1971.
- J. T. Oden, L. Demkowicz, W. Rachowicz, and T. A. Westermann. Toward a universal hp adaptive finite element strategy, Part 2. A posteriori error estimation. *Computer Methods in Applied Mechanics and Engineering*, 77(1-2):113–180, 1989.

- R. K. Pal, R. Abedi, A. Madhukar, and R. B. Haber. Adaptive spacetime discontinuous Galerkin method for hyperbolic advection–diffusion with a non-negativity constraint. *International Journal for Numerical Methods in Engineering*, 105:963–989, 2016.
- J. Palaniappan, R. B. Haber, and R. L. Jerrard. A spacetime discontinuous Galerkin method for scalar conservation laws. *Computer Methods in Applied Mechanics and Engineering*, 193(33-35): 3607–3631, 2004.
- J. Peraire and P. O. Persson. The compact discontinuous Galerkin (CDG) method for elliptic problems. *SIAM Journal on Scientific Computing*, 30(4):1806–1824, 2008.
- D. A. Di Pietro and A. Ern. *Mathematical Aspects of Discontinuous Galerkin Methods*, volume 69. Springer Science & Business Media, 2011.
- F. Rathgeber, D. A. Ham, L. Mitchell, M. Lange, F. Luporini, A. T. T. McRae, G. T. Bercea, G. R. Markall, and P. H. J. Kelly. Firedrake: automating the finite element method by composing abstractions. *ACM Transactions on Mathematical Software (TOMS)*, 43:24, 2017.
- P. A. Raviart and J. M. Thomas. A mixed finite element method for 2-nd order elliptic problems. In *Mathematical Aspects of the Finite Element Method*, pages 292–315, Springer-Verlag, New York, 1977.
- W. H. Reed and T. R. Hill. Triangular mesh methods for the neutron transport equation. *Los Alamos Report LA-UR-73-479*, 1973.
- J. F. Remacle, J. E. Flaherty, and M. S. Shephard. An adaptive discontinuous Galerkin technique with an orthogonal basis applied to compressible flow problems. *SIAM Review*, 45:53–72, 2003.
- B. Rivière. *Discontinuous Galerkin Methods for Solving Elliptic and Parabolic Equations: Theory and Implementation*. SIAM, 2008.
- B. Rivière and M. F. Wheeler. Discontinuous Galerkin methods for flow and transport problems in porous media. *International Journal for Numerical Methods in Biomedical Engineering*, 18: 63–68, 2002.
- B. Rivière, M. F. Wheeler, and V. Girault. Improved energy estimates for interior penalty, constrained and discontinuous Galerkin methods for elliptic problems. Part I. *Computational Geosciences*, 3:337–360, 1999.
- T. Rusten, P. Vassilevski, and R. Winther. Interior penalty preconditioners for mixed finite element approximations of elliptic problems. *Mathematics of Computation of the American Mathematical Society*, 65:447–466, 1996.
- P. G. Saffman and G. Taylor. The penetration of a fluid into a porous medium or Hele-Shaw cell containing a more viscous liquid. *Proceedings of the Royal Society of London A: Mathematical, Physical and Engineering Sciences*, 245:312–329, 1958.
- D. Z. Turner, K. B. Nakshatrala, M. J. Martinez, and P. K. Notz. Modeling subsurface water resource systems involving heterogeneous porous media using the variational multiscale formulation. *Journal of Hydrology*, 428:1–14, 2012.
- R. Verfürth. *A Posteriori Error Estimation Techniques for Finite Element Methods*. Oxford Science Publications, New Jersey, 2013.
- H. Wilbraham. On a certain periodic function. *Cambridge and Dublin Mathematical Journal*, 3 (198):1848, 1848.